UNIVERSIDAD DE CHILE
FACULTAD DE CIENCIAS FÍSICAS Y MATEMÁTICAS
DEPARTAMENTO DE INGENIERÍA ELÉCTRICA

DESIGN, CONSTRUCTION AND TESTING OF A 2SB RECEIVER FOR THE SOUTHERN MILLIMETER-WAVE TELESCOPE

TESIS PARA OPTAR AL GRADO DE DOCTOR EN INGENIERÍA ELÉCTRICA

RAFAEL IGNACIO RODRÍGUEZ OLIVOS

PROFESOR GUÍA:
FAUSTO PATRICIO MENA MENA

MIEMBROS DE LA COMISIÓN:
LEONARDO BRONFMAN AGUILÓ
RODRIGO REEVES DÍAZ
RICARDO BUSTOS PLACENCIA

Este trabajo ha sido parcialmente financiado por Center of Excellence in Astrophysics and Associated Technologies (CATA), Gemini-CONICYT Fund 32100003, Gemini-CONICYT Fund 32130023, Proyecto Fondecyt 1121051, and "Programa de Formación de Capital Humano Avanzado" of CONICYT.

SANTIAGO DE CHILE
2015

Abstract

This work presents a prototype sideband-separating (2SB) receiver for the 1.2m Southern Millimeter Wave Telescope (SMWT) in the framework of its upgrading. The upgrading consists of changing the configuration of the receiver from double sideband (DSB) to 2SB in order to obtain a competitive receiver for astronomical observations. It also presents the performance of this receiver in combination with a digital platform that integrates an intermediate-frequency hybrid and spectrometer in an astronomical receiver. In this way, sideband-rejection ratios beyond current state-of-the-art are obtained.

First, we have characterized the all-analogue 2SB receiver and their components by determining two important figures of merit: sideband ratio and noise temperature. The sideband-rejection ratio was higher than 7 dB in all the working bandwidth, showing that the costume-made components (RF-hybrid, LO-splitter and RF-load) performed well into specifications. The noise-temperature of the receiver was below 1500 K for commercial mixers, and more recently after an upgrade of the low noise amplifier and the mixers, below 300 K.

Secondly, we have also measured the sideband rejection ratios for different configurations of the 2SB receiver using a digital IF hybrid and a spectrometer as a back-end. In all cases, a sideband rejection ration above 35 dB was obtained.

Furthermore, we have compared the sideband rejection of an all-analogue ALMA Band-9 2SB receiver with the one using the digital back-end. We obtained sideband rejection ratios above 35 dB in all the RF band for the digital version, always above the equivalent analogue receiver. This is above any state-of-the-art all analogue-2SB receiver.

RESUMEN DE LA TESIS
PARA OPTAR AL GRADO DE
DOCTOR EN INGENIERÍA ELÉCTRICA
POR: RAFAEL IGNACIO RODRÍGUEZ OLIVOS.
FECHA: 29 DE ENERO 2015
PROF. GUÍA: SR. FAUSTO PATRICIO MENA

DISEÑO, CONSTRUCCIÓN AND PRUEBA DE UN RECEPTOR SEPARADOR DE BANDA LATERAL PARA EL TELESCOPIO AUSTRAL DE ONDAS MILIMETRICAS

Este trabajo presenta un prototipo de un receptor de separación de banda lateral (2SB) para el Telescopio Austral de Ondas Milimétricas (SMWT) de 1.2 m de diámetro en el marco de su modernización. Ésta consiste en cambiar la configuración del receptor desde una configuración de doble banda lateral (DSB) a una 2SB con el fin de obtener un receptor competitivo para las observaciones astronómicas. También se presenta el rendimiento de este receptor en combinación con una plataforma digital que integra un híbrido de frecuencia intermedia (IF) y un espectrómetro en un receptor astronómico. De esta manera, se logran razones de rechazo de banda mejores que el actual estado del arte .

En primer lugar, hemos caracterizado el receptor 2SB totalmente analógico y sus componentes usando dos importantes figuras de mérito: rechazo de banda y temperatura de ruido. La razón de rechazo de banda fue mayor que 7 dB en toda el ancho de banda de trabajo, mostrando que los components frabricados (Híbrido RF, Bifurcación de LO y Carga RF) cumplieron de buena forma las especificaciones. La temperatura de ruido del receptor estuvo bajo los 1500 K, atribuible principalmente al bajo rendimiento de los mezcladores comerciales, y más recientemente 300 K, después de cambiar el amplificador de bajo ruido y los mezcladores.

Segundo, hemos medido también la razón de rechazo de banda para diferentes configuraciones del receptor 2SB usando un espectrómetro e híbrido RF digital como *back-end*. En todos los casos, una razón de rechazo de banda superior a 35 dB fue obtenida.

Además, hemos comparado el rechazo de banda de un receptor completamente análogo 2SB de Banda-9 de ALMA con uno usando el esquema de *back-end* digital. Obtuvimos razones de rechazo de banda sobre 35 dB in toda la banda RF para el versión digital. Ésto esta sobre el rendimiento de cualquier receptor 2SB completamente análogo en la actualidad.

A mi familia...

Acknowledgements

Quisiera agradecer a quienes de una u otra forma han participado en este trabajo, partiendo por el Profesor Pablo Estévez quien me dio la idea y oportunidad de realizar el postgrado y a mi Profesor Guía Patricio Mena, quien me presentó este proyecto en un área que siempre quise explorar. También quiero agradecer a mis compañeros de doctorado Pablo Zorzi, Laurent Pallanca, Jaime Álvarez, Claudio Barrientos, Victor Hugo Calle y Jorge Castillo por hacer más ameno y grato el transcurso del postgrado en Beaucheff.

También me gustaría agradecer a los integrantes del laboratorio de ondas milimétricas Nicolás Reyes, Francisco Navarrete, Claudio Jarufe, Pablo Vázquez, Valeria Tapia y Ricardo Finger, quienes aportaron tanto con sus conocimientos en muchos aspectos de este trabajo, como con su buen humor y amistad fuera del laboratorio. Tampoco puedo dejar de lado a José Pizarro, sin quien hubiese sido imposible finalizar el proyecto, dado que cada pieza mecánica a construir pasó por sus manos.

Agradezco a los Profesores Leonardo Bronfman, Rodrigo Reeves y Ricardo Bustos por la buena disposición y tiempo dedicado en la corrección para hacer de esta tesis un mejor trabajo.

Agradezco a mis padres Rosa y Manuel, a mi hermana Anita y principalmente a mis tías Alicia y Carmen por el apoyo y afecto incondicional que me entregaron durante este largo proceso.

Para finalizar agradezco a mis amigos de la vida Rodrigo Inostroza, Gabriela Alcázar e Isao Parra por haber estado en las buenas y en las malas durante todo este tiempo.

Contents

List of Tables

List of Figures

Chapter 1

Introduction

During recent years Astronomy has become an important topic in Chile, a fact that has been stirred by the construction of some of the most important and powerful astronomical centers in the world. The reason for this interest in the Chilean territory is the quality of its northern skies which have exceptional atmospheric conditions appropriate for optical and radio astronomy. In fact, several state-of-the-art optical and radio observatories have been built in Chile. Among the optical observatories we have the Very Large Telescope (VLT) located at Cerro Paranal [1], the Gemini Sur [2] at Cerro Pachón, the Cerro Tololo Inter-American Observatory (CTIO) [3] at Cerro Tololo and others under construction as the European Extremely Large Telescope (E-ELT) at Cerro Armazones [1] and the Giant Magellan Telescope (GMT) at Cerro las Campanas [4]. Among the radio astronomical facilities we can mention, for example, the Cosmic Background Imager (CBI) [5], the Atacama Pathfinder EXperiment (APEX) [6], and the Atacama Large Millimeter Array (ALMA) [7] [8]. Universidad de Chile has been directly related with radio astronomy since the sixties with the Maipú Radio Observatory, which was used for the radio observation of the Sun and Jupiter [9], and of other phenomena in Jupiter, like the effect of the impact of Shoemaker Levy-9 [10]. Later, during the eighties, Universidad de Chile participated in the observation of molecular CO [11] using the 1.2-m Southern Millimeter-Wave Telescope (SMWT) which was located at Cerro Tololo International Observatory. During the mid-nineties, its use was discontinued because its performance became poor when compared to similar instruments. In 2009, it was moved from the CTIO to the Astronomy Department of University of Chile for a complete upgrading has been carried out. The present proposal is in the framework of the project of improving the SMWT, changing the configuration of the receiver from Double Sideband (DSB) to Sideband Separating (2SB) improving the signal-to-noise ratio and consequently reducing the observation time.

1.1 Objectives

The current work has two main objectives:

1. Design, construction, assembling and testing of a prototype 2SB receiver for the Southern Millimeter Wave Telescope located at the Department of Astronomy in the University of Chile. This receiver should have an operational radio frequency bandwidth of 84−116 GHz, an intermediate frequency bandwidth of 3 GHz, a sideband rejection ration better than 20 dB and noise temperature less than 300 K.
   (a) Design and construction of the Radio Frequency (RF) components for the 2SB configuration: RF Hybrid, Local Oscillator (LO) Bifurcation and RF Load.
   (b) Characterize the 2SB receiver using the Hot-Cold test and measuring its Sideband Rejection Ratio.
   (c) Design the test setups for the characterization of the 2SB receiver.
2. Demonstrate the functionality of a digital back-end at millimeter and sub-millimeter wavelengths.
   (a) Integrate the digital back-end and the analogue part of the SMWT receiver.
   (b) Characterize the SMWT receiver with the digital back-end.
   (c) Verify the use of the digital back-end at sub-millimeter wavelengths in an ALMA Band-9 prototype 2SB receiver at Space Research Organisation Netherlands (SRON).

1.2 Scientific importance of the 84−116 GHz Band

In the study of the galactic dynamics it is important to explore the central kilo-parsec[1] of our galaxy. This region is obscured by the dust in the optical wavelength but not in the millimeter to far infrared wavelength range. Of particular importance are the Carbon Monoxide (CO) surveys because this molecule is a good tracer of Molecular Hydrogen (H_2), which cannot be observed by ground based telescopes [12]. A number of important astronomical sources, can be observed from the southern hemisphere. For instance, the center of the Milky Way can be best observed from Cerro Calán The Astronomy Department of the University of Chile has been part of the observations of the Galactic Center [13] using the 1.2-m SMWT of the molecular CO [11] at the CTIO. In 2005, the receiver of the SMWT was brought from the CTIO to the Millimeter Wave Laboratory of Universidad de Chile for upgrading.

At the Millimeter Wave Laboratory (MWL) in the Astronomy Department of the Universidad de Chile, the local oscillator source was changed from a klystron to a Gunn oscillator [14] and a Low Noise Amplifier (LNA) was added as a first amplification stage to reduce the noise [15]. Then, after determining the atmospheric transmission at Cerro Calan using the SMWT receiver [16], the SMWT was moved from CTIO to Cerro Calan in 2009 and installed in its final position in 2009 [17] (see figure 1.1). Now, the SMWT is being used for academic purposes, and is planned to be used for research with the present upgrades.

[1] 1 parsec = 3.26 light years

(a)

(b)

(c)

Figure 1.1: Installation of the SMWT in Cerrro Calán in September 2010. (a) Moment when the telescope is being installed. (b) Moment when the dome is being installed. (c) Telescope finally installed at Cerro Calan.

Initially, the SMWT was designed to observe mostly the $^{12}C^{16}O$ line at 115.3 GHz and $^{13}C^{16}O$ at 110.3 GHz although it works down to 109.8 GHz, the $^{12}C^{18}O$ line. With the latest upgrades [14, 15] the SMWT reached the capability of observing other spectral lines in the range of 84–116 GHz. Some lines that can be find in this range are presented in the table 1.1.

This work aims to improve the current SMWT receiver capability, changing the receiver configuration from DSB to 2SB configuration, increasing the useful Intermediate Frequency (IF) bandwidth and reducing the noise contribution due to atmospheric conditions.

Table 1.1: Some Important Radio Lines in 84−116 GHz [18].

Chemical Name	Chemical Formula	Transition*	Frequency (GHz)
Silicon Monoxide	SiO	ν=1, J=2 → 1	86.243
Hydrogen Cyanide	HCN	J=1 → 0 , three F transitions	88.632
Formylium	HCO^+	J=1 → 0	89.189
Diazenylium	N_2H^+	J=1 → 0, seven F transitions	93.174
Carbon Monosulfide	CS	J=2 → 1	97.981
Carbon Monoxide	$^{12}C^{18}O$	J=1 → 0	109.782
Carbon Monoxide	$^{13}C^{16}O$	J=1 → 0	110.201
Carbon Monoxide	$^{12}C^{17}O$	J=1 → 0, three F transitions	112.359
Carbon Monoxide	$^{12}C^{16}O$	J=1 → 0	115.271

*This correspond to the molecular emission lines where J is the quantum number of angular momentum.

1.3 Atmospheric conditions in the 84−116 GHz Band at Cerro Calan

From September 2008 to July 2009 a study of the atmospheric transmission at the new site of the SMWT, Cerro Calan, was performed [16]. In that study the receiver of the radio telescope was used as a radiometer, doing measurements at 115 GHz. Figure 1.2 presents the results of the measurements performed in [16]. In that study, the optical depth was measured during nine months and it was demonstrated that the atmosphere in Cerro Calán presents a mean atmospheric transmission above 73%, for more than half of the year. The best period of observation is from June to November, part of autumn, winter and spring in the southern hemisphere, where the saturation vapor pressure is lower. Considering the result of the atmospheric transmission, it was concluded that Cerro Calán is an appropriate site for hosting the SMWT. The installation of the SMWT occurred in 2009. The installation of the telescope in its new building was carried out in 2010 and first light was obtained on November 17, 2010 [17].

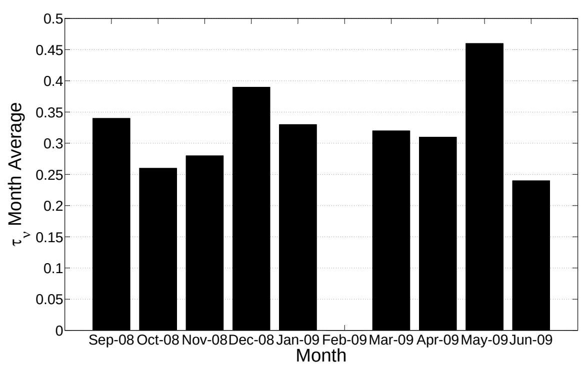

Figure 1.2: Monthly average of the optical depth τ_ν. Note that during February no measurements were performed since the facilities were closed.

Chapter 2

Literature Review

2.1 Radio Telescopes and the SMWT

2.1.1 General configuration

A general configuration of a receiver is presented in figure 2.1. First, an antenna collects the signal and guides the RF signal, in the order of few μW or -60 dBm, to the front end. Inside the front end, the signal feeds first a LNA that amplifies it usually in the order of 20 to 30 dB. Before reaching the mixer the RF signal has to be combined with the LO signal. This step can be performed with a resonant ring or a directional coupler. If we have a receiver which uses a balanced mixer a separate combiner is not needed because the signals are combined inside the block where the mixing takes place. For details of mixing process see section 2.3.1. At the mixer the RF signal is converted to an IF which is easier to handle for digitalization, that means a frequency in the order of few GHz. The new IF signal is a representation of the RF signal but in lower frequency which is equal to the difference between the RF and LO frequencies. After the mixer a band pass filter is needed to eliminate the spurious frequencies produced by the mixing process. The final stage in the front end is a new amplification of the IF signals, usually in the order of 30 dB.

The LNA is usually a High Electron Mobility Transistor (HEMT) placed inside a cryostat for operation at cryogenic temperatures in order to diminish its noise contribution.

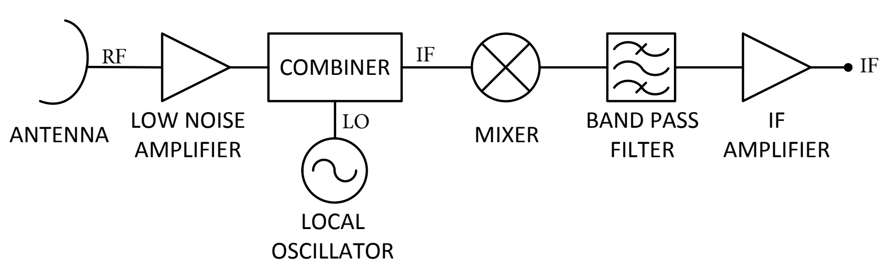

Figure 2.1: Schematic of a DSB heterodyne receiver. At high frequencies, when SIS mixers are used, the RF signal enters the mixer without amplification.

The most common technologies for implementing the mixer are Superconductor-Isolator-Superconductor (SIS) junctions and Schotttky diodes. SIS junctions, for example, are used in most of the bands of ALMA [19]. Their use depends on the noise level to be achieved, the LO power available and operational costs. Here it is necessary to emphasize that if a SIS junction is used, the LNA is not necessary and the RF signal is fed in directly into the next stage, in these cases the mixers are cooled down to 4 Kelvin.

2.1.2 Double Sideband Configuration (DSB)

The double sideband configuration, in some way, is the simplest receiver. The receiver uses the minimum quantity of components. Figure 2.1 represents a typical configuration of this kind of receiver. The frequency response of this configuration produces the superposition of the Lower Sideband (LSB) and the Upper Sideband (USB) which are components of the RF signal. This superposition increases the noise in the down-converted signal IF and, therefore, in the observation time. Additionally, this overlap in the IF could lead to observe the phenomenon of line confusion, due to the difficulty in identifying if the signal comes from the LSB or USB components. Figure 2.2 illustrates those problems.

2.1.3 Single Sideband Configuration (SSB)

The Single Sideband (SSB) configuration is presented in figure 2.3. The SSB differs from the DSB by a filter added before the mixer. With this filter it is possible to suppress one of the bands, USB o LSB, depending of the kind of filter used. Filtering one sideband the receiver avoids the problem of spectrum overlap, see figure 2.4, in the IF. Consequently, it reduces the noise from the image band and the confusion of the signal in the IF. However, half of the RF spectrum is lost and, additionally, making tunable filters at mm-wavelengths is still very difficult.

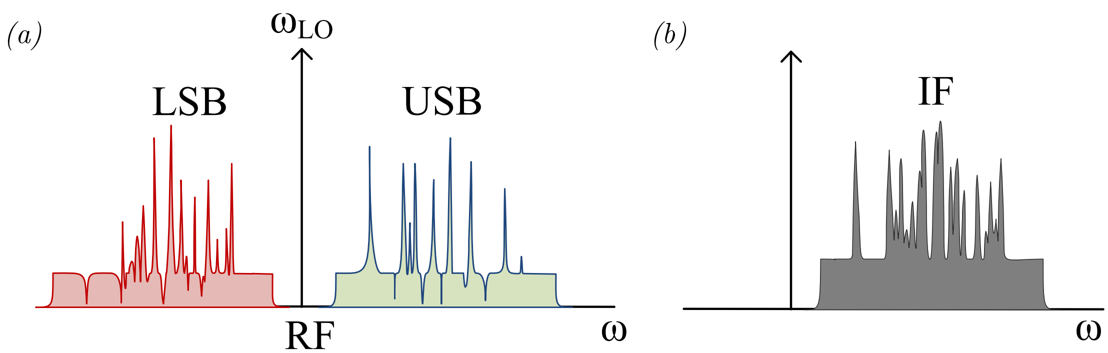

Figure 2.2: Representation of RF signals. *(a)* RF signal observed by the receiver at certain LO frequency. *(b)* After the down conversion the noise floor is higher and it is difficult to identify the band of origin of the signal.

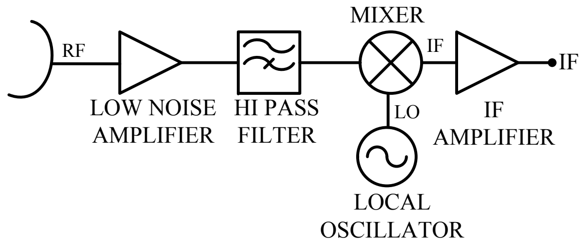

Figure 2.3: Schematic of a SSB receiver. The main difference with respect of the DSB is the filter which is used in order to eliminate one of the bands presented in the RF signal (USB or LSB). In this case the high pass filter suppress the LSB.

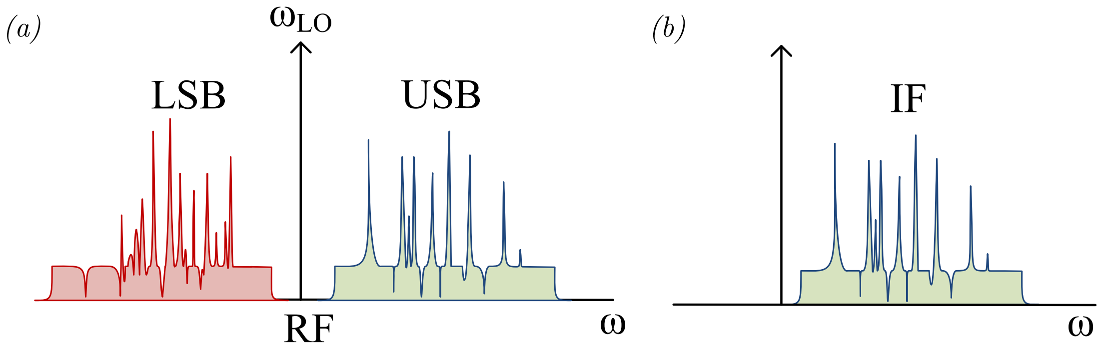

Figure 2.4: *(a)* Representation of RF signals. *(b)* The final spectrum obtained with the configuration of figure 2.3 is only the USB.

2.1.4 Sideband Separating Configuration (2SB)

The use of the 2SB configuration implies an increase in the number of components and complexity, but makes it possible to observe the two sidebands simultaneously, reducing the noise in each sideband by a factor of two, and increasing the bandwidth of the observations. The 2SB configuration, presented in figure 2.5, has the inconvenience that the sideband rejection depends highly on the amplitude and phase imbalance of the entire system. In order to minimize the imbalance, the total electrical length and gain must be the same in the two branches of the system. Mixers must have similar behavior, and hybrids and power splitters must perform very close to their nominal design. Achieving all of this over wide RF and IF ranges is, in practice, very difficult.

To illustrate the operation of a 2SB receiver consider figure 2.4. The LSB and USB components are represented in the RF domain. The latter are downconverted and using the 2SB receiver configuration the RF signal can be separated in two outputs avoiding the superposition of the sidebands.

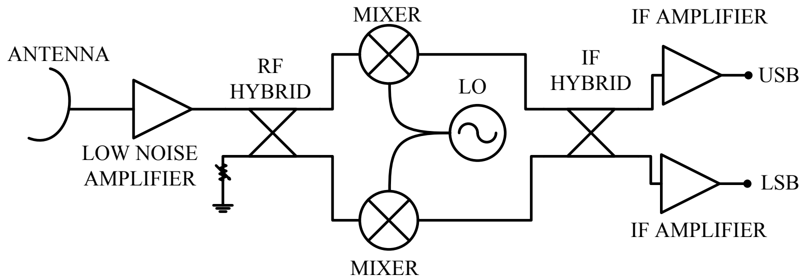

Figure 2.5: Schematic of a 2SB receiver, the main difference when comparing with a DSB receiver are the use of two mixers, the RF and IF hybrid and the LO splitter. The RF and IF hybrid split the signal reducing its power in −3 dB and adding a phase shift of 90° between the outputs.

2.2 The Southern Millimeter-Wave Telescope

2.2.1 Antenna Focusing System

The antenna focusing system is composed by an antenna and a horn. The antenna is a Cassegrain Antenna which consists of a primary and a secondary reflector with their support and alignment structure. In figure 2.6 a scheme of the antenna is shown. On January 2013, the radiation pattern of the antenna was measured [20]. This measurement was performed in the antenna far-field at 4 km from Cerro Calán. The radiation pattern obtained at 115.3 GHz is presented in figure 2.7. The main characteristics of the radiation pattern are shown in figure 2.8.

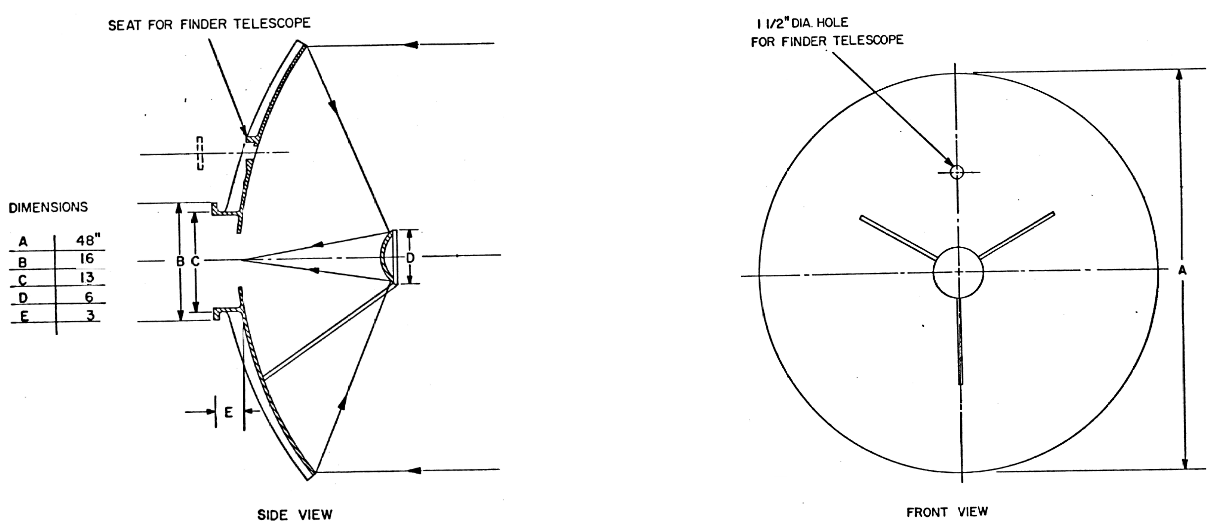

(a) (b)

Figure 2.6: Scheme of the antenna Cassagrain. (a) Side view showing the ray trace. (b) A front view is presented showing the diameter of the antenna and the position of the finder [21].

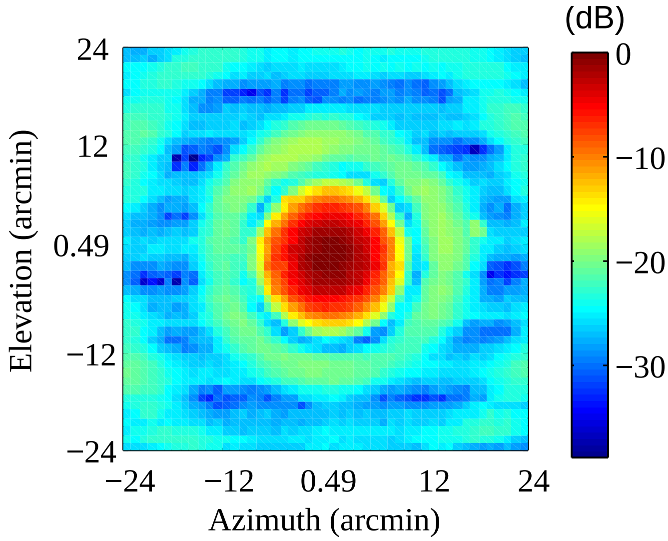

Figure 2.7: Radiation pattern of the SMWT located at Cerron Calán [20].

(a)

Parameter	Value
x_0	0.0616'
y_0	-0.6657'
a	9.1829'
b	8.5543'
ϕ	12.21°
e	0.36363
g	6.84 %

(b)

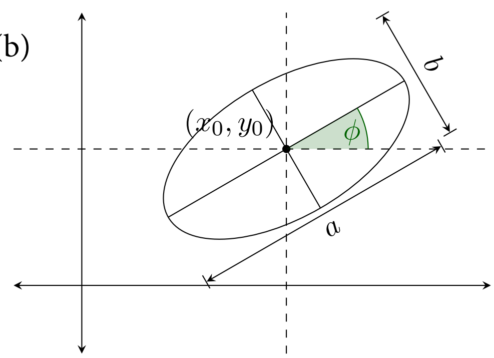

Figure 2.8: Parameters obtained from the radiation pattern on January 2013. (a) Parameters of the beam pattern. (b) Representation of the parameters over an ellipse [20].

2.2.1.1 Primary Reflector

The primary reflector was fabricated from a single aluminum casting which was machined to a parabolic surface with a focal length of 0.45 meters. A center hole of 0.15 meters in diameter, corresponding to the region shadowed by the secondary, is located in the primary to allow the access to the feed horn and associated electronics. In addition, a 38 mm off-axis hole is provided for a finding telescope, which is located about 0.3 meters from the optical axis.

2.2.1.2 Secondary Reflector

The clear aperture of the hyperbolic secondary reflector is 0.150 meters. Also this reflector was fabricated from a single aluminum block. The distance between the focal point of the hyperboloid is 45 cm, so that the focal point of the Cassegrain system lies at the vertex of the primary paraboloid.

2.2.1.3 Horn

The horn is a conical corrugated which has some advantages such as low side lobes, wide bandwidth and low cross polarization. For the transition between the circular waveguide to the WR-10 standard, a six-step transformer was used. As the other parts in the antenna the horn was made from copper using electro-forming techniques.

2.2.2 Original receiver

The original receiver configuration of the radio telescope is presented in figure 2.9. This configuration receives directly the RF signal into a resonant ring and a diplexer where the RF and LO signals were coupled. This new signal enters the Schottky-barrier diode where the signal is down converted to 1390 MHz. All these components are inside a dewar which is cooled down with liquid nitrogen to 77 K. A wet dewar was used, meaning that it was necessary to refill it every 12 hours approximately. The time for total liquid N_2 loss was three days.

A Klystron[1] was used as LO. The Klystron generated a signal of 57 GHz with a power of 25 mW and a doubler was needed to reach 113.9 GHz. To stabilize the Klystron oscillator a Phase Lock Loop (PLL) was used. The reference signal was obtained by a coupler in the Klystron output and mixing it in a harmonic mixer. In one of the upgrades, the klystron local oscillator was changed to a Gunn oscillator.

2.2.3 Back-end

The back-end of the SMWT consists of two filter banks spectrometer. The first one has 256 channels of 0.1 MHz and the second has 128 channels of 1 MHz of resolution, giving 25.6 and 128 MHz of bandwidth, respectively [17].

[1] The principle of operation of the Klystron is the following. A beam of electrons (stream of cathode rays) is accelerated before passing by a resonant cavity. This cavity generates a wave which modifies the velocity of the beam electrons. This wave has the same frequency that the field inside the cavity and a velocity lower than the beam.

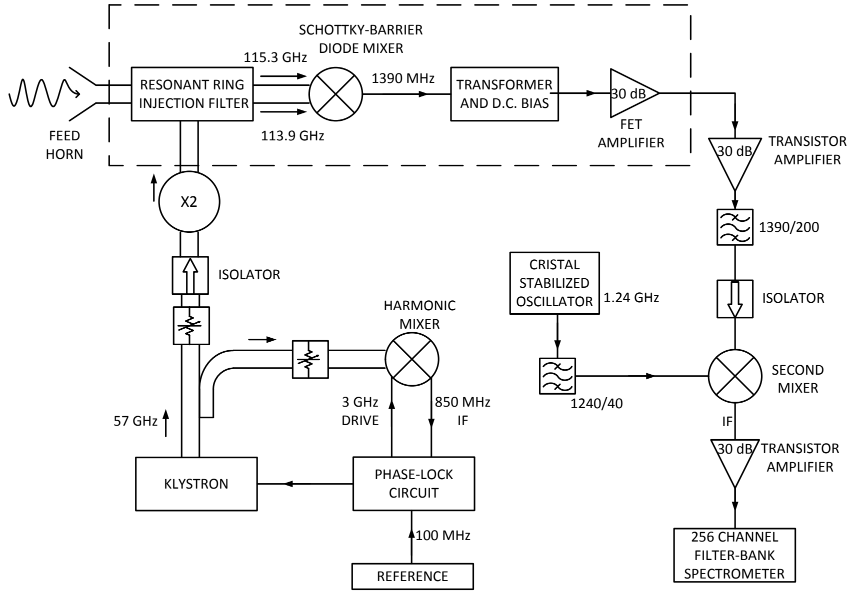

Figure 2.9: Original Configuration of the the Southern Millimeter-Wave Telescope receiver.

2.3 Technologies for mixing.

2.3.1 Mixing Theory

The mixing of signals is produced by elements which have a non-linear I-V relation. Under this condition new signals can be created from an input signal. A non-linear I-V relationship can be expanded in a series of power,

$$F\left(V\right) = \alpha_0 + \alpha_1 V + \alpha_2 V^2 + \alpha_3 V^3 + ... \tag{2.1}$$

If we replace the value of V by:

$$V = A_1 \sin(\omega_1 t) + A_2 \sin(\omega_2 t) \tag{2.2}$$

where $\omega_1 = 2\pi f_1$ and $\omega_2 = 2\pi f_2$,

we obtain:

$$\begin{aligned} F(V) &= \alpha_0 + \alpha_1 [A_1 \sin(\omega_1 t) + A_2 \sin(\omega_2 t)] \\ &\quad + \alpha_2 [A_1 \sin(\omega_1 t) + A_2 \sin(\omega_2 t)]^2 + ... \end{aligned} \tag{2.3}$$

Considering the quadratic term and expanding it, we obtain

$$\begin{aligned} [A_1 \sin(\omega_1 t) + A_2 \sin(\omega_2 t)]^2 &= A_1^2 \sin^2(\omega_1 t) + 2A_1 A_2 \sin(\omega_1 t) \sin(\omega_2 t) \\ &\quad + A_2^2 \sin^2(\omega_2 t). \end{aligned} \tag{2.4}$$

Using the following trigonometric relationships

$$\sin^2(\theta) = \frac{1-2\cos(2\theta)}{2} \tag{2.5}$$

$$\sin(\theta)\sin(\phi) = \frac{\cos(\theta-\phi)-\cos(\theta+\phi)}{2} \tag{2.6}$$

Equation 2.3 can be re-written as follows

$$\begin{aligned} F(V) &= \alpha_0 + \alpha_1[A_1\sin(\omega_1 t) + A_2\sin(\omega_2 t)] \\ &+\alpha_2\Bigg\{A_1^2\frac{1-2\cos(2\omega_1 t)}{2} \\ &+2A_1A_2\left[\frac{\cos((\omega_1-\omega_2)t)-\cos((\omega_1+\omega_2)t)}{2}\right] + A_2^2\frac{1-2\cos(2\omega_2 t)}{2}\Bigg\}. \end{aligned} \tag{2.7}$$

Observe that if we consider the terms of higher orders in equation 2.1, it is possible to observe all the combinations of $n\omega_1$, $m\omega_2$ and $n\omega_1 \pm m\omega 2$. Then, simplifying Equation 2.7 taking into account only the components of second order and in special the component derived from the sine products (from equation 2.4), we obtain

$$F(V) = K[\cos((\omega_1-\omega_2)t) - \cos((\omega_1+\omega_2)t)] \tag{2.8}$$

where K represents all the constants related with the second order term. Then, considering the term which contains the frequency difference (the other terms are not considered since they are in frequencies higher or lower than the operational and therefore filtered), we have

$$\begin{aligned} F(V) &= K\cos((\omega_1-\omega_2)t) \\ &= K\cos(2\pi(f_1-f_2)t). \end{aligned} \tag{2.9}$$

Finally, changing $f_1 - f_2$ by f_{IF} we obtain a new signal with a frequency equal to the difference between f_1 and f_2

$$F(V) = K\cos(2\pi f_{IF} t). \tag{2.10}$$

In electronics, the frequencies f_1 and f_2 are from LO and RF signals and the difference between those produces the IF, which contain the same information of RF but in a lower frequency determined by the LO frequency.

2.3.2 Single Diode Mixer

The procedure performed in the section 2.3.1 can be implemented in a single mixer diode, presented in figure 2.10. In this type of mixer the LO and RF signals feed the same diode,

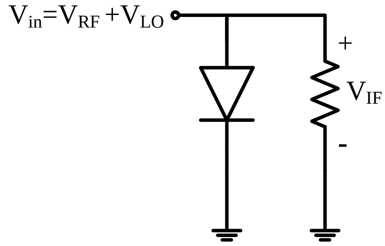

Figure 2.10: Electrical circuit of the single diode mixer. Both frequency signals arrive at the same diode.

producing a IF signal over the resistor. Then, for the single diode mixer the output is described by

$$V_{IF} = K\cos(2\pi(f_{LO} - f_{RF})t) = K\cos(2\pi f_{IF}t). \tag{2.11}$$

2.3.3 Balanced Mixers

The balanced mixer can be formed by connecting two reversed biased mixer to an input hybrid. Figure 2.11, shows a basic configuration of the 180° balanced mixer. Following Kooi [22], we will use a polynomial expansion to represent the currents $i_1(t)$ and $i_2(t)$ through the diodes. For $i_1(t)$ we have

$$\mathrm{i}_1(t) = a_0 + a_1v_1(t) + \frac{a_2v_1(t)^2}{2!} + \frac{a_3v_1(t)^3}{3!} + \cdots = \sum_{n=0}^{\infty}\frac{a_nv_1(t)^n}{n!} \tag{2.12}$$

but, since the voltage across diode 2 is reverse from diode 1 ($v_2(t) = -v_1(t)$), for $i_2(t)$ we have

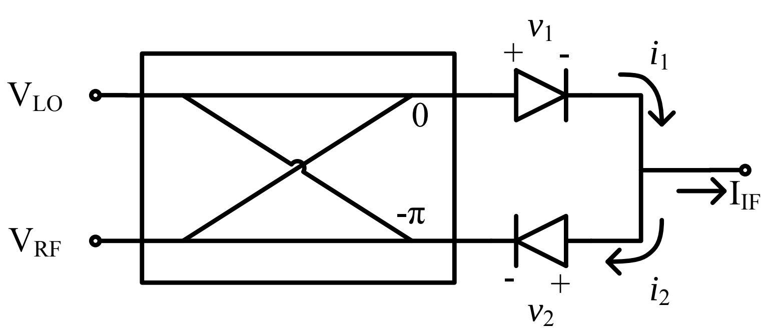

Figure 2.11: 180° balanced mixer scheme. V_{LO} and V_{RF} are combined by the hybrid into 2 signals, introducing a phase shift of 180° between the output signals.

$$\mathrm{i}_2(t) = b_0 - b_1 v_2(t) + \frac{b_2 v_2(t)^2}{2!} - \frac{b_3 v_2(t)^3}{3!} + \cdots = \sum_{n=0}^{\infty} (-1)^n \frac{b_n v_2(t)^n}{n!}. \quad (2.13)$$

The terms a_n and b_n represent the mixer conversion gain (magnitude, not power). The equations 2.12 and 2.13 contain terms related with the dc component ($n = 0$), the fundamentals ($n = 1$), the second order difference and product terms ($n = 2$), and the harmonic and inter modulation products ($n \geq 3$). It is also possible to observe from equations 2.12 and 2.13 that the product terms decrease by $n!$, then terms higher than forth order can be neglected.

Considering the voltages of $V_{LO}(t) = V_{LO}\cos(\omega_{LO}t)$ and $V_{RF}(t) = V_{RF}\cos(\omega_{RF}t)$ as the inputs to the ideal hybrid (no losses and imbalances), the voltages over the diodes are

$$v_1(t) = V_{RF}\cos(\omega_{RF}t) + V_{LO}\cos(\omega_{LO}t) \quad (2.14)$$

$$v_2(t) = V_{RF}\cos(\omega_{RF}t) + V_{LO}\cos(\omega_{LO}t - \pi). \quad (2.15)$$

From the figure 2.11, and applying the Kirchhoff law, the current $\mathrm{I}_{IF}(t)$ is:

$$\mathrm{I}_{IF}(t) = \mathrm{i}_1(t) - \mathrm{i}_2(t). \quad (2.16)$$

Using the equations 2.12 and 2.13 in equation 2.16 and with the assumption that the mixer gain are equal ($a_n = b_n = K_n$), we obtain

$$\mathrm{I}_{IF}(t) = [K_0 - K_0] + K_1[v_1(t) + v_2(t)] + K_2\left[v_1(t)^2 - v_2(t)^2\right]. \quad (2.17)$$

Replacing the values of v_1 and v_2 by the equations 2.14 and 2.15, and simplifying we obtain

$$\begin{aligned} \mathrm{I}_{IF}(t) &= K_1\big[2 \times V_{RF}\cos(\omega_{RF}t)\big] + K_2\big[4 \times V_{RF}V_{LO}\cos(\omega_{RF}t)\cos(\omega_{LO}t)\big] + \cdots \\ &= K_1^*\big[\cos(\omega_{RF}t)\big] + K_2^*\big[\cos(\omega_{RF}t)\cos(\omega_{LO}t)\big] + \cdots \end{aligned} \quad (2.18)$$

Using the trigonometric identity

$$\cos\alpha\cos\beta = \frac{\cos(\alpha+\beta) + \cos(\alpha-\beta)}{2}, \quad (2.19)$$

equation 2.18 can be rewritten as follow

$$\mathrm{I}_{IF}(t) = K_1^*[\cos(\omega_{RF}t)] + K_2^{**}[\cos((\omega_{RF}+\omega_{LO})t) + \cos((\omega_{RF}-\omega_{LO})t)] + \cdots \quad (2.20)$$

The first term corresponds to the fundamental RF signal and the second term is related to the IF signal. Then, selecting the term related directly to the IF we finally obtain

$$\mathrm{I}_{IF}(t) = V_{IF}[\cos((\omega_{RF}-\omega_{LO})t)] = V_{IF}[\cos(\omega_{IF}t)]. \quad (2.21)$$

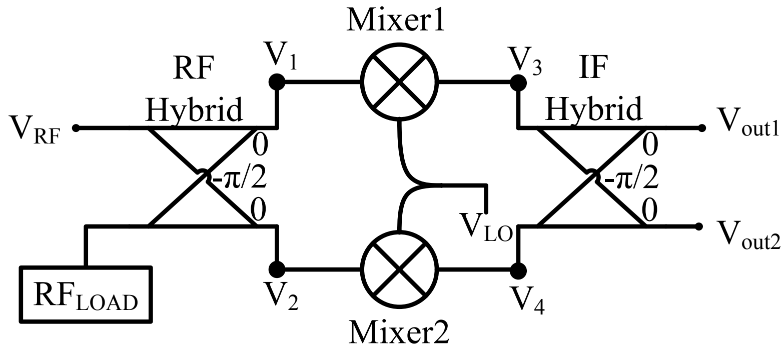

Figure 2.12: 2SB mixer configuration. It is shown the two mixers and the two hybrids, one in the RF and other in the IF, necessaries for this configuration. Both hybrids produced a phase shift of 90° between the outputs ports. The LO signal pass through a splitter and feed both mixers in phase.

2.3.4 2SB configuration

The 2SB mixer configuration is presented in figure 2.12. Consider an input signal V_{RF} expressed by

$$V_{RF}(t) = V_{RF}\cos(\omega_{RF_{LSB}}t) + V_{RF}\cos(\omega_{RF_{USB}}t). \tag{2.22}$$

where the components of the USB and LSB of the signal are represented by $\omega_{RF_{USB}}$ and $\omega_{RF_{LSB}}$ respectively. It is possible to express the terms related with the USB and LSB in function of the LO frequency as

$$\omega_{RF_{USB}} = \omega_{LO} + \omega_{IF_{USB}} \tag{2.23}$$
$$\omega_{RF_{LSB}} = \omega_{LO} - \omega_{IF_{LSB}} \tag{2.24}$$

Using the new variables, V_{RF} can be expressed as,

$$V_{RF}(t) = V_{RF}\cos((\omega_{LO} + \omega_{IF_{USB}})t) + V_{RF}\cos((\omega_{LO} - \omega_{IF_{LSB}})t). \tag{2.25}$$

The voltages V_1 and V_2 in the RF hybrid outputs, presented in figure 2.12, can be expressed in function of V_{RF}, where $V_1(t)$ and $V_2(t)$ corresponds to V_{RF} with a phase shift of 0° and 90°, respectively, i.e.,

$$V_1(t) = \underbrace{V_{RF}\cos((\omega_{LO} + \omega_{IF_{USB}})t)}_{USB \quad \rightarrow} + \underbrace{V_{RF}\cos((\omega_{LO} - \omega_{IF_{LSB}})t)}_{LSB \quad \rightarrow} \tag{2.26}$$

$$V_2(t) = \underbrace{V_{RF}\cos((\omega_{LO} + \omega_{IF_{USB}})t - \frac{\pi}{2})}_{USB \quad \downarrow} + \underbrace{V_{RF}\cos((\omega_{LO} - \omega_{IF_{LSB}})t - \frac{\pi}{2})}_{LSB \quad \downarrow}. \tag{2.27}$$

The arrows below the equation, represent the phase of each frequency band. These voltages are downconverted to the voltages V_3 and V_4 after the mixers 1 and 2. Then, those voltages can be expressed as

$$V_3(t) = \left[\underbrace{V_{RF}\cos((\omega_{LO}+\omega_{IF_{USB}})t)}_{USB} + \underbrace{V_{RF}\cos((\omega_{LO}-\omega_{IF_{LSB}})t)}_{LSB}\right] \times V_{LO}\cos(\omega_{LO}t) \quad (2.28)$$

$$V_4(t) = \left[\underbrace{V_{RF}\cos((\omega_{LO}+\omega_{IF_{USB}})t-\frac{\pi}{2})}_{USB} + \underbrace{V_{RF}\cos((\omega_{LO}-\omega_{IF_{LSB}})t-\frac{\pi}{2})}_{LSB}\right] \times V_{LO}\cos(\omega_{LO}t) \quad (2.29)$$

Then, using the trigonometric relationship given by equation 2.19 we obtain

$$\begin{aligned} V_3(t) &= \underbrace{V_{IF}\frac{\cos((2\omega_{LO}+\omega_{IF_{USB}})t)+\cos(\omega_{IF_{USB}}t)}{2}}_{USB} \\ &+ \underbrace{V_{IF}\frac{\cos((2\omega_{LO}-\omega_{IF_{LSB}})t)+\cos(-\omega_{IF_{LSB}}t)}{2}}_{LSB} \quad (2.30) \\ V_4(t) &= \underbrace{V_{IF}\frac{\cos((2\omega_{LO}+\omega_{IF_{USB}})t-\frac{\pi}{2})+\cos(\omega_{IF_{USB}}t-\frac{\pi}{2})}{2}}_{USB} \\ &+ \underbrace{V_{IF}\frac{\cos((2\omega_{LO}-\omega_{IF_{LSB}})t-\frac{\pi}{2})+\cos(-\omega_{IF_{LSB}}t-\frac{\pi}{2})}{2}}_{LSB} \quad (2.31) \end{aligned}$$

Now we can select the frequencies directly related with ω_{IF} since this frequencies correspond to the down-converted signal, which leads to

$$\begin{aligned} V_3(t) &= V_{IF}\left[\underbrace{\frac{\cos(\omega_{IF_{USB}}t)}{2}}_{USB\ \rightarrow} + \underbrace{\frac{\cos(-\omega_{IF_{LSB}}t)}{2}}_{LSB\ \rightarrow}\right] \quad (2.32) \\ V_4(t) &= V_{IF}\left[\underbrace{\frac{\cos(\omega_{IF_{USB}}t-\frac{\pi}{2})}{2}}_{USB\ \downarrow} + \underbrace{\frac{\cos(-\omega_{IF_{LSB}}t-\frac{\pi}{2})}{2}}_{LSB\ \downarrow}\right]. \quad (2.33) \end{aligned}$$

Note that the term related with LSB in V_4 has a negative sign. Using the parity of the function cosine it is possible to re-write $V_3(t)$ and $V_4(t)$ as follow

$$V_3(t) = V_{IF}\left[\underbrace{\frac{\cos(\omega_{IF_{USB}}t)}{2}}_{USB \quad \rightarrow} + \underbrace{\frac{\cos(\omega_{IF_{LSB}}t)}{2}}_{LSB \quad \rightarrow}\right] \tag{2.34}$$

$$V_4(t) = V_{IF}\left[\underbrace{\frac{\cos(\omega_{IF_{USB}}t - \frac{\pi}{2})}{2}}_{USB \quad \downarrow} + \underbrace{\frac{\cos(\omega_{IF_{LSB}}t + \frac{\pi}{2})}{2}}_{LSB \quad \uparrow}\right] \tag{2.35}$$

Continuing with the circuit presented in figure 2.12, the voltages V_{out1} and V_{out2} are the output of the IF hybrid 90° producing another phase shift of $-\frac{\pi}{2}$ between the outputs, i.e.

$$V_{out1}(t) = V_3(t)\angle 0 + V_4(t)\angle -\frac{\pi}{2} \tag{2.36}$$

$$V_{out2}(t) = V_3(t)\angle -\frac{\pi}{2} + V_4(t)\angle 0. \tag{2.37}$$

Replacing equations 2.34 and 2.35 into equations 2.36 and 2.37 leads to

$$\begin{aligned} V_{out1}(t) = & V_{IF}\left[\underbrace{\frac{\cos(\omega_{IF_{USB}}t)}{2}}_{USB \quad \rightarrow} + \underbrace{\frac{\cos(\omega_{IF_{LSB}}t)}{2}}_{LSB \quad \rightarrow}\right] \\ & + V_{IF}\left[\underbrace{\frac{\cos(\omega_{IF_{USB}}t - \pi)}{2}}_{USB \quad \leftarrow} + \underbrace{\frac{\cos(\omega_{IF_{LSB}}t)}{2}}_{LSB \quad \rightarrow}\right] \end{aligned} \tag{2.38}$$

$$\begin{aligned} V_{out2}(t) = & V_{IF}\left[\underbrace{\frac{\cos(\omega_{IF_{USB}}t - \frac{\pi}{2})}{2}}_{USB \quad \downarrow} + \underbrace{\frac{\cos(\omega_{IF_{LSB}}t - \frac{\pi}{2})}{2}}_{LSB \quad \downarrow}\right] \\ & + V_{IF}\left[\underbrace{\frac{\cos(\omega_{IF_{USB}}t - \frac{\pi}{2})}{2}}_{USB \quad \downarrow} + \underbrace{\frac{\cos(\omega_{IF_{LSB}}t + \frac{\pi}{2})}{2}}_{LSB \quad \uparrow}\right] \end{aligned} \tag{2.39}$$

Finally, V_{out1} and V_{out2} are expressed as

$$V_{out1}(t) = V_{IF}\left[\cos(\omega_{IF_{LSB}}t)\right] \quad \Rightarrow \quad V_{LSB} \tag{2.40}$$

$$V_{out2}(t) = V_{IF}\left[\cos(\omega_{IF_{USB}}t - \tfrac{\pi}{2})\right] \quad \Rightarrow \quad V_{USB} \tag{2.41}$$

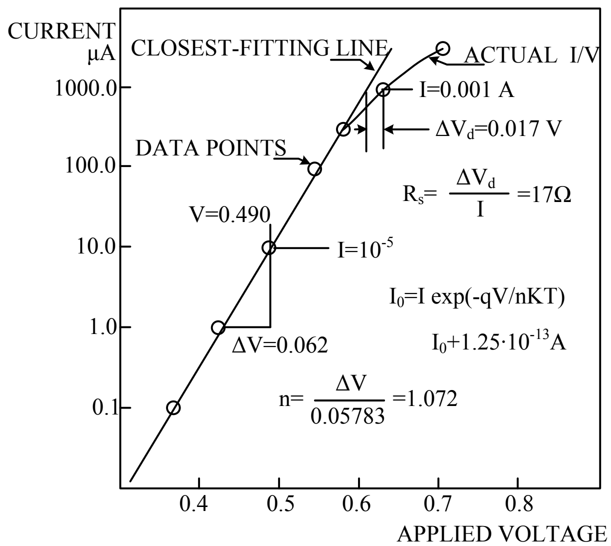

Figure 2.13: A typical non linear I-V curve of a Schottky Diode. Notice the logarithmic scale. The circles over the line are the measured I-V data of a Schottky diode [23].

2.3.5 Schottky Diodes and SIS Junction

In section 2.3.1 it was shown how to produce the mixing process with a non-linear electrical component. Typical components used in radio astronomy that have a non-linear behaviour are Schottky diodes and Superconductor-Isolator-Superconductor (SIS) junctions.

2.3.5.1 Schottky Diodes

The Schottky diode is formed by a metal contact to a semiconductor. The diode is usually made of silicon or GaAs thanks to their high electron mobility. Many materials can create a Schottky barrier on either silicon or GaAs semiconductor. In the case of GaAs, the most common are platinum, titanium and gold [23]. N-type semiconductors are the most used for mixer diodes since they have lower series resistances and higher cut-off frequencies.

In general, Schottky diodes are majority-carrier devices that do not suffer from the charge-storage effects that limit the use of semiconductor p-n junction. At the metal to semiconductor interface a voltage dependent potential barrier is created producing a strongly non-linear current-voltage characteristic that can be used for the mixing of two signals [23]. In figure 2.13 the characteristic I-V curve of a Schottky diode is presented.

In figure 2.14 the energy band structures of a metal and a semiconductor before and after the formation of the junction are shown. When the metal and semiconductor are in equilibrium and are not in contact (figure 2.14a) the energy levels are constant in the materials. When the materials are joined (figure 2.14b) some of the electrons in the semiconductor move to the metal and collect on its surface. This movement produces an ionized donors location in the semiconductor, which are positively charged, and these create a negative surface on the metal. As a consequence, an electric field is set up between these positive and negative

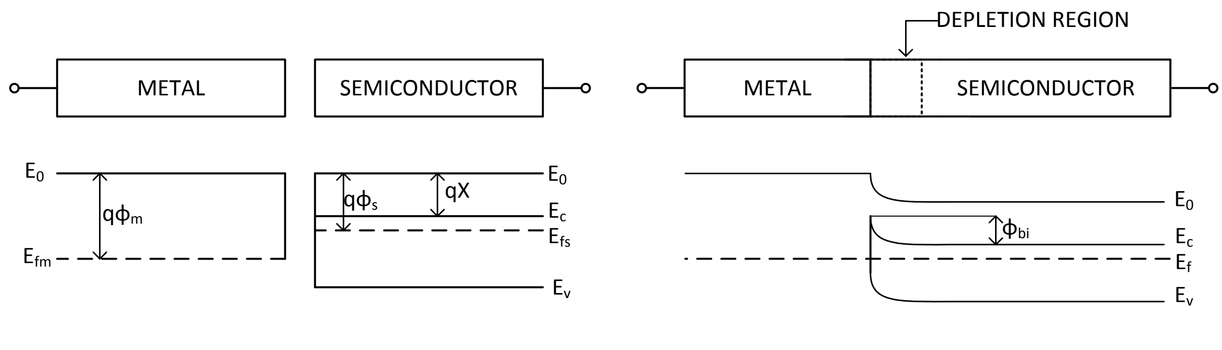

Figure 2.14: Energy band of a Schottky junction before and after the junction. (a) Band structure of the metal and semiconductor before the contact. E_0 is the free-space energy level, E_c is the bottom of the conduction band and E_v is the top of the valence band. E_{fm} and E_{fs} are the Fermi levels in the metal and semiconductor, respectively. (b) Band structure of the Schottky junction.

charges decreasing the flow of the electrons into the metal. This charged region is called depletion region, since it is almost completely depleted of mobile electrons. This barrier originates the non-linear I-V curve when electrons are forced through it.

Schottky diode mixers are widely used in receivers for frequencies lower than 100 GHz, although it is possible to use them at higher frequencies. The advantages of these diodes are the relatively low cost and the high operation temperatures at which they can be used when compared with other technologies like SIS junctions. One of the main limitations of the Schottky diode is the higher LO power needed for its operation, being in the order of 1 mW [24].

Important for radio astronomical use is that the dominant noise source in Schottky-barrier diodes is thermal noise generated in the series resistance and shot noise arising from carrier emission across the junction [23]. To diminish their noise contribution they are usually cooled below 77 K.

2.3.5.2 Superconductor-isolator-Superconductor (SIS) junctions

The SIS diode consists of two superconductors separated by a very thin insulating layer. The electrons can flow across this diode only by tunnelling through the insulator that separates the two superconductors. For this current to be significant, the insulator has to be thin enough so that the quantum mechanical wave function for the electrons in the superconductors has a significant overlap in the insulator. Usually the insulator can have a width of 0.6 to 1 nm [25].

An important difference of the SIS junction when compared to the Schottky diodes is that the gap in voltage between filled and empty states in the superconductor is of about 1 to 2.5 mV which is comparable to the energy of the photon at about 300 − 1000 GHz. In addition, the LO power requirement is 1000 times lower than what is needed for conventional mixers [26] like the Schottky diodes. Figure 2.15 shows the characteristic I-V curve and the

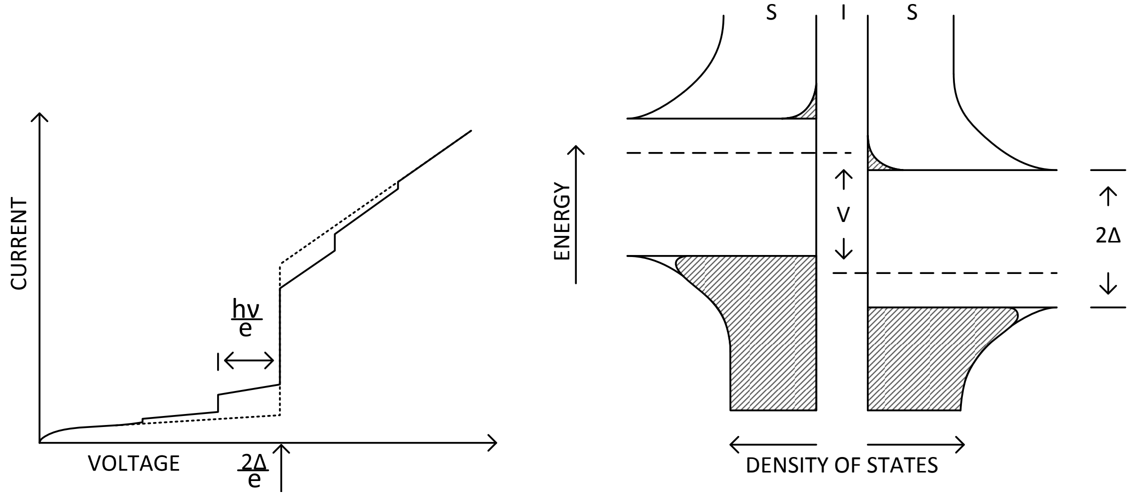

(a) (b)

Figure 2.15: Characteristics of a SIS junction. (a) Ideal I-V curve with (solid line) and without (dashed line) the presence of a LO signal. (b) Density of states showing the occupied states a temperature $T > 0$ [26]. 2Δ corresponds to the superconducting energy gap which is the energy required to produce two single particle excitation from a Copper pair [22].

density of state in a SIS diode.

For low noise operation a SIS junction needs to be DC biased at an appropriate voltage and current. If, in addition to the mixer bias, there is a source of photons of energy $h\nu$, then tunnelling can occur at a lower bias voltage, $h\nu$/e. If the SIS device is biased and the LO signal is applied at frequency ν, extra conduction steps appear (the so-called Shapiro steps) [26]. Under these conditions, for a weak signal present at a frequency around ν the conversion of these photons to lower frequencies is more efficient than with a classical mixer [26]. An increase of the gap energy allows the efficient detection of higher-frequency photons. This is usually achieved using niobium [19, 27].

SIS mixers are used in the front ends for operations between 150 GHz and 1000 GHz because [26]:

- Their intrinsic low noise contribution.
- The IF bandwidths can be higher than 1 GHz. For example the IF of ALMA receivers have a bandwidth of 8 GHz starting at 4 GHz.
- They can be tuned over around 30% of the central frequency.
- The local-oscillator power that is needed is less than 1 μW.

As disadvantages of the SIS junction we can mention the low temperature needed for its operation (4 K) that increases the costs of operation. Moreover, a magnetic field is required to minimize the noise induced by Josephson currents.

Although SIS junctions have a better performance in the mixing process compared with

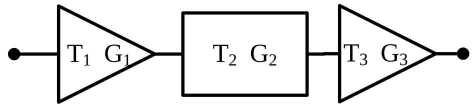

Figure 2.16: Simplified scheme of a receiver. T_i and G_i represent the noise temperature and gain of each component.

Schottky diodes, for this project we have selected the latter as mixing component. The main reason is that the use of liquid Helium is extremely expensive. Moreover, a Schottky diode in combination with a 2SB configuration and amplification with enough gain can still make the SMWT competitive.

2.4 Amplifiers

2.4.1 Friis Formula

One important component in radio receivers is the amplification, in particular the amplification in the first stage. This can be illustrated using the figure 2.16 and the Friis equation [28]. This equation gives the noise temperature of a system due to the individual contribution of noise temperature from the components in cascade. The noise temperature of the system is related with how much noise introduces the system in the received signal. At normal temperatures and no electrical force, the electrons are in random motion. Therefore, in average, there is no net motion. This random motion, however, produces a current that can be measured. At any temperature above 0 K the thermal noise power generated in a conductor is proportional to its absolute physical temperature. Then, in the case of figure 2.16 the noise temperature of the system, T_{SYS}, is

$$T_{SYS} = T_1 + \frac{T_2}{G_1} + \frac{T_3}{G_1 \times G_2} \tag{2.42}$$

where T_i and G_i are the noise temperature and the gain of the components, respectively. Equation 2.42 shows the importance of a good first component in a radio receiver. The gain of the first device decrease the contribution of the noise due to the following stages. Also the equation shows that the noise of the receiver is dominated mainly by the first component. Then, a good amplifier with high gain and low noise is required in order to obtain a good receiver and low T_{SYS}.

2.4.2 Low Noise Amplifiers based in HEMTs

The LNAs based on High Electron Mobility Transistor (HEMT)s can be implemented using different types of HEMT technologies: Pseudomorphic High Electron Mobility Transistor (p-HEMT); Indium Phosphide High Electron Mobility Transistor (InP-HEMT); and inside

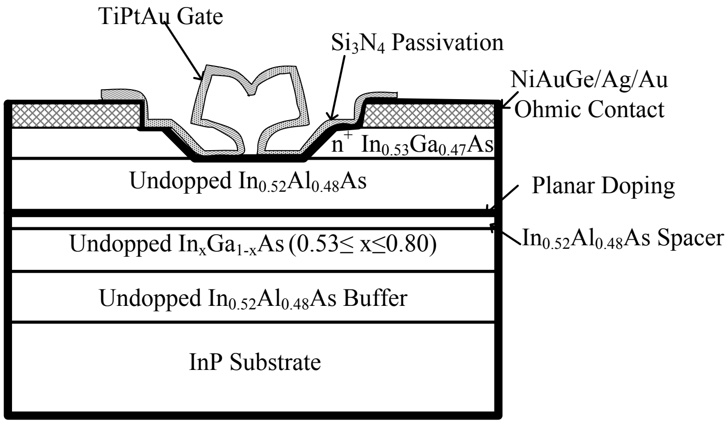

Figure 2.17: Cross section of typical InP based low noise HEMT [30].

a group of HEMTs forming a Microwave/Millimeter-wave Integrated Circuit (MMIC) [29, 30, 31, 32]. The earliest HEMT's were based on the GaAS/AlGaAs material system. GaAs-based HEMT's with pseudomorphic InGaAs channels provided improved millimeter wave performance, including reduced noise figure and increased power-added efficiency [30].

The GaAs-based pseudomorphic p-HEMT differs from the conventional AlGaAs/GaAs HEMTs. In latter, a thin (typically $50 - 200$ A°) layer of $In_xGa_{1-x}As$ (x=0.15 − 0.35) is inserted between the AlGaAs layer and GaAs buffer. The device is therefore based on the AlGaAs/InGaAs hetero-junction. GaAs-based p-HEMT have shown excellent noise and gain performance [32].

The InP-based HEMT performance arises directly from the intrinsic properties of the InAlAs/InGaAs material system. The high indium content (typically 53-80 %) InGaAs channel possesses high electron mobility and velocity, and the large conduction band discontinuity at the InGaAs/InAlAs hetero-junction permits high current and transconductance. The high transconductance of the InP-HEMT is most directly responsible for its increased operating frequency and excellent gain-bandwidth properties [30]. Figure 2.17 presents a typical cross section of a InP-HEMT [30]. In particular the MWL has two InP-HEMT amplifiers developed by Caltech in the early 2000s, labeled $W10$ and $W7$. The first is located inside the current receiver of the SMWT and the second is a spare amplifier.

2.5 Digital Back-end

The digital back-end used in this work was developed by R. Finger during his PhD. Thesis [33]. The hardware used to perform the signal processing is known as the Reconfigurable Open Architecture Computing Hardware (ROACH) [34]. The ROACH is an open Field Programmable Gate Array (FPGA)-based (Xilinx Virtex 5) platform, the product of an international collaboration lead by the Center for Astronomy Signal Processing and Electronic Research (CASPER) in University of California at Berkeley. CASPER aims to produce open hardware designs and software/gateware resources for signal processing in astronomy.

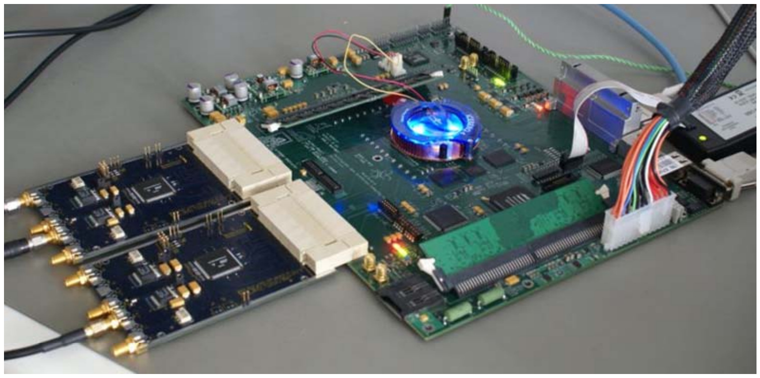

Figure 2.18: Typical configuration of a ROACH with 2 ADC.

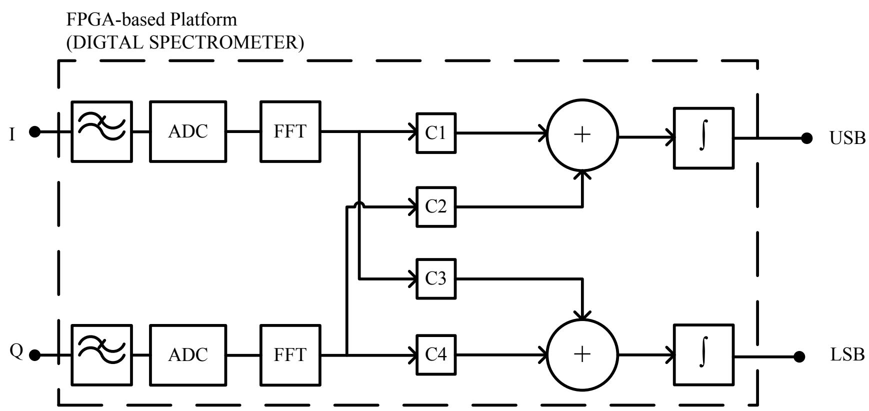

Figure 2.19: Model of the digital hybrid inside the ROACH.

The centrepiece of the ROACH is a Xilinx Virtex 5 FPGA. A separate Performance Optimization With Enhanced RISC Performance Computing (PowerPC) chip runs Linux and is used to control the board, programming the FPGA and allow interfacing between the FPGA software registers/BRAMs/FIFOs and external devices using Ethernet. The high performance Virtex-5 FPGA in which the ROACH is based can be programmed to perform very demanding parallel data processing algorithms usually found in radio astronomy. Figure 2.18 shows a typical ROACH connected with two Analog-to-Digital Converter (ADC)s [34].

The work of Finger [33] consisted in the implementation of a digital IF hybrid and digital spectrometer using a ROACH. The goal of that implementation is the possibility to compensate all the imbalances produced by the RF-hybrid, mixers, difference in cable lengths in the IF-plate and any other component before the back-end. That work was tested as a proof of concept at 2 GHz and it was not tested in a millimeter radio astronomical receiver.

In order to achieve this goal, the digital back-end must be calibrated. With the calibration the constants C1 to C4 of figure 2.19 are determined. These constants represent an IF-hybrid which has an amplitude and phase difference between its ports equal to the total phase and phase imbalances. With these constants the digital IF-hybrid reduce the total imbalances producing high rejection ratios. Figure 2.19, shows a block diagram of the digital back-end implemented in the ROACH.

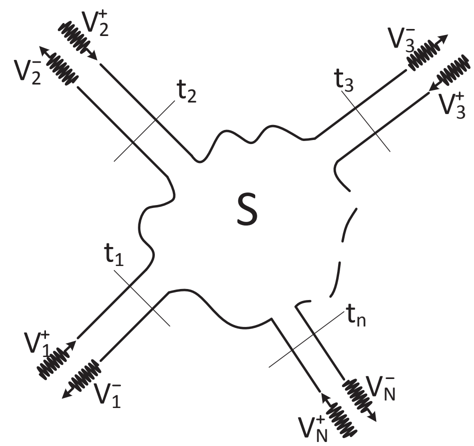

Figure 2.20: An arbitrary N-port microwave network.

2.6 Characterization of a 2 network system - S Parameters or Scattering Parameters

A practical problem exists when trying to measure voltages and currents at microwave frequencies, because direct measurements usually involve the magnitude and phase of the wave travelling in a given direction, or of a standing wave. For that reason, a representation more in accord with the direct measurement, and with the ideas of incident, reflected, and transmitted wave is given by the S-parameters.

The S-parameters provide a complete description of a network, relating the voltage waves incident on the ports to those reflected from the ports. They can be calculated using network analysis techniques, or measured directly using a Vector Network Analyser (VNA). Once the scattering parameters or S-parameters are known, the conversion to other matrix parameter can be performed.

Let us consider a N-port network, see figure 2.20, where V_n^+ is the voltage wave incident to the port n, and V_n^- is the voltage wave reflected from the port n. The scattering matrix, or $[S]$ matrix, is defined in relation to these incident and reflected voltage waves as

$$\begin{bmatrix} V_1^- \\ V_2^- \\ \vdots \\ V_N^- \end{bmatrix} = \begin{bmatrix} S_{11} & S_{12} & \dots & S_{1N} \\ S_{21} & S_{22} & \dots & S_{2N} \\ \vdots & \vdots & \ddots & \vdots \\ S_{N1} & S_{N2} & \dots & S_{NN} \end{bmatrix} \begin{bmatrix} V_1^+ \\ V_2^+ \\ \vdots \\ V_N^+ \end{bmatrix} \tag{2.43}$$

or

$$\left[V^-\right] = \left[S\right] \left[V^+\right]. \tag{2.44}$$

A specific element of the $[S]$ matrix can be determined as

$$S_{ij} = \left.\frac{V_i^-}{V_j^-}\right|_{V_k^+=0 \quad for \quad k\neq j} \tag{2.45}$$

Equation 2.45 says that S_{ij} can be found by driving port j with an incident wave of voltage V_j^+, and measuring the reflected wave amplitude, V_i^- coming out of port i. The incident waves on all ports are zero except for the jth port, which means that all ports should be terminated in matched loads to avoid reflections. Then, S_{ii} correspond to the reflection coefficient seen into port i when all ports are terminated in matched loads, and S_{ij} is the transmission coefficient form port j to i when all other ports are terminated in a matched load [35].

2.7 Characterization of a receiver

In the characterization of the receiver presented in this work it is necessary to consider two important figures of merit, the noise temperature and the sideband rejection ratio.

2.7.1 Noise Temperature measurement

The noise temperature of the system is related with how much noise introduces the system in the received signal. In order to estimate the noise due to the temperature produced by the thermal noise of a system, the technique called Hot/Cold test is used.

At normal temperatures and no electrical force, the electrons are in random motion. Then, in average, there is no net motion. This random motion, however, produces a current that can be measured. At any temperature above 0 K the thermal noise power generated in a conductor is proportional to its absolute physical temperature. Then, the thermal noise power is related with the noise temperature by

$$P = kB(T_N + T) \tag{2.46}$$

where, P is the power (watts), k is the Boltzmann's constant, $1,38 \times 10^{-23} J/K$, B is the Bandwidth (hertz), T_N is the noise temperature (K) and T is the physical temperature of the device which produces the noise.

The noise temperature of a receiver, T_R, can be determined using the hot/cold test. This technique consists of measuring the output power of the device under test, when the input power comes from two elements (loads), at two different known temperatures. Usually, the temperatures of the loads are ambient temperature (298 K) and liquid nitrogen (77 K). With these power measurements we first calculate the ratio between them, known as Y-factor,

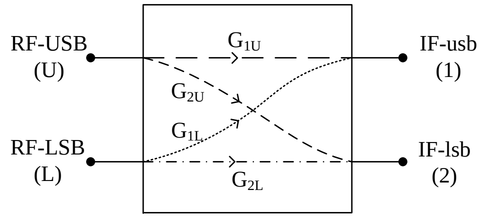

Figure 2.21: Schematic of the flow of the RF sidebands into the IF outputs

$$Y = \frac{P_{Hot}}{P_{Cold}}. \tag{2.47}$$

On the other hand, using 2.47, we can relate the Y-factor with the noise temperature of the receiver and the physical temperature of the hot and cold loads,

$$Y = \frac{T_{Hot} + T_R}{T_{Cold} + T_R} \tag{2.48}$$

Equating equations 2.47 and 2.48, and solving for T_R (receiver temperature) we obtain the noise temperature of the receiver as function of the physical temperature of the two loads,

$$T_R = \frac{T_{Hot} - T_{Cold}Y}{Y - 1} \tag{2.49}$$

2.7.2 Image Rejection of a Sideband-Separating Receiver

The sideband rejection ratio is a figure of merit used to estimate the amount of power from the image band which is presented in the signal band. This figure of merit is used in 2SB receivers where exists a separation between the image and signal bands.

To determine the image rejection we need to determine how much power of one sideband is contained in the other sideband. In other words, considering figure 2.21, we want to determine the ratios,

$$R_1 = \left.\frac{G_{1U}}{G_{1L}}\right|_{IF\ Port_{USB}} \qquad R_2 = \left.\frac{G_{2L}}{G_{2U}}\right|_{IF\ Port_{LSB}} \tag{2.50}$$

where $G_{i,j}$ corresponds to the conversion gain between the ports i and j. Basically, there are two ways to measure this parameter. The first way is measuring directly the output. The second is by using the procedure presented by Kerr [36] in an indirect way with the use of hot and cold loads.

2.7.2.1 Direct measurement of Sideband Rejection Ratio (SRR)

This method measures directly the ratio of the signal from the RF signal to the IF port. The measure procedure is summarized,

1. With a continuous-wave (CW) test signal in the USB band of the RF, the corresponding IF signal at the IF port 1, obtaining G_{1U}
2. With a CW test signal in the LSB band of the RF, the corresponding IF signal at the IF port 1, obtaining G_{1L}
3. With a CW test signal in the USB band of the RF, the corresponding IF signal at the IF port 2, obtaining G_{2U}
4. With a CW test signal in the LSB band of the RF, the corresponding IF signal at the IF port 2, obtaining G_{2L}

where the variables G_{1U}, G_{1L}, G_{2L} and G_{2U} are presented in figure 2.21. Finally the SRR is obtained calculating the following ratios,

$$R_1 = \frac{G_{1U}}{G_{1L}} \; ; \; R_2 = \frac{G_{2U}}{G_{2L}} \tag{2.51}$$

This measurement, as mentioned before, has the inconvenience that it can be incorrect if the dependence of the RF power in frequency is not considered. This is particular true for receiver with large IF bands. For that reason a calibration of the RF power must be done in order to correct this dependence.

2.7.2.2 SRR with hot/cold loads

This procedure for measuring the Sideband Rejection Ratio (SRR) follows [36] and is summarized here. See figure 2.21 for details.

1. With a CW test signal in the upper sideband, the corresponding IF signals at the IF ports 1 and 2 are measured. The ratio is

$$M_U = \frac{G_{1U}}{G_{2U}}. \tag{2.52}$$

2. With a CW test signal in the lower sideband, the corresponding IF signals at the IF ports 1 and 2 are measured. The ratio is

$$M_L = \frac{G_{2L}}{G_{1L}}. \tag{2.53}$$

3. Measure the changes, $\Delta P1$ and $\Delta P2$, of output power at IF ports 1 and 2, when a cold load at the receiver input is replaced by a hot load. Then, if the difference between the noise temperature of the hot and cold loads is ΔT, we have

$$\Delta P_1 = kB\Delta T(G_{1U} + G_{1L}) \tag{2.54}$$

$$\Delta P_2 = kB\Delta T(G_{2U} + G_{2L}) \tag{2.55}$$

With the equations 2.54 and 2.55 we define the ratio

$$M_{DSB} \triangleq \frac{\Delta P_1}{\Delta P_2} = \frac{G_{1U} + G_{1L}}{G_{2U} + G_{2L}} \tag{2.56}$$

where the terms M_U, M_L and M_{DSB} can be used to deduce the sideband separation ratios R_1 R_2, using the relations

$$R_1 = M_U \frac{M_L M_{DSB} - 1}{M_U - M_{DSB}} \tag{2.57}$$

and

$$R_2 = M_L \frac{M_U - M_{DSB}}{M_L M_{DSB} - 1}. \tag{2.58}$$

2.8 Conclusions

In this chapter we have reviewed the most important concepts for this thesis. The review considered the scientific motivation and a description of receiver configurations, technologies associated to the receivers, the description of the SMWT and parameters used in a characterization of a 2SB receiver.

Chapter 3

Design and Construction of the Receiver and its Components

In this chapter, the design and construction of the components and their assembling in the receiver is presented. Furthermore, the design of the test setups for the measurements and characterization of the receiver will be also presented.

3.1 2SB Receiver Concept

The receiver implemented in this work corresponds to a 2SB receiver in the band of $84-116$ GHz. Our philosophy was to design a modular receiver that combines home-made and off the shelf parts, following the configuration presented in 2.1.4. We have implemented two configurations. The first one is a full-analogue receiver. In the second one the IF-hybrid was replaced by a digital IF-hybrid with a digital spectrometer.

Figure 3.1 shows the 2SB receiver design, where the two main blocks, the analogue RF and the digital back-end are presented. The components designed in this work are RF-hybrid, LO-splitter and RF load. Other components such as the mixers, IF filters and amplifiers were purchased to Millitech, Minicircuits and Miteq, respectively. Since the mixers were purchased as independent blocks, the design of the RF-hybrid and LO-splitter was adapted to their physical dimensions.

The electromagnetic design and optimization of the components was performed using the software [37] and the mechanical design of the receiver was performed using [38].

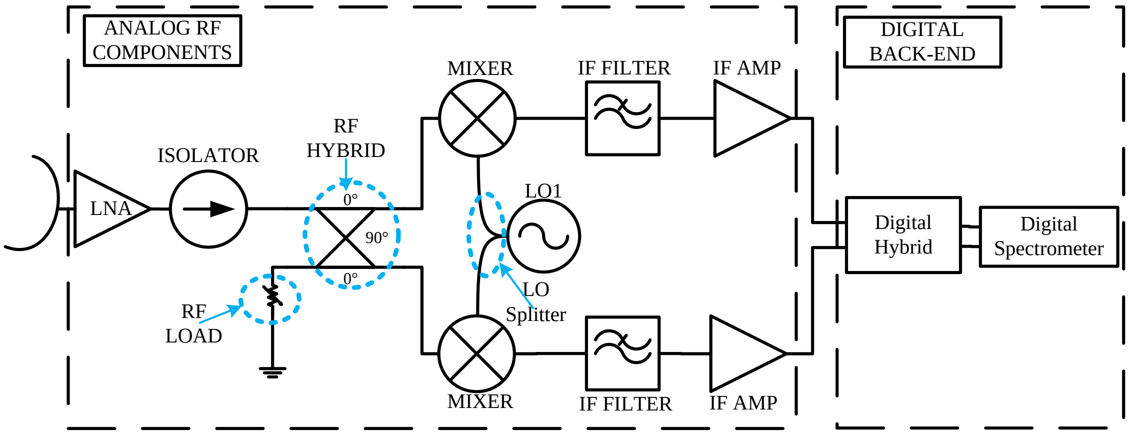

Figure 3.1: Block diagram of a 2SB receiver. The components designed in this work are indicated with the dotted circles.

3.2 Analogue Components

3.2.1 RF load

The design of the load needed to terminate the unused port of the RF hybrid was done following [39, 40]. ECCOSORB® MF-124 [41] has been selected as absorber due to its good electrical and magnetic properties. One diagonal structure, transversal to the E-plane of the waveguide, was selected for construction simplicity. The length of the load was optimized using High Frequency Structure Simulation (HFSS) [37], with the goal of obtaining a reflection less than -20 dB. To ease the implementation of the load, we constructed a large cavity (with the appropriate inclination) at the end of one of the outputs of the hybrid. As shown in figure 3.2, this cavity was then filled with a block of ECCOSORB®. In figure 3.3, the S_{11} parameter of the load is plotted and compared with -20 dB. This result shows that the reflection of the load is less than -25 dB for all the frequency band, satisfying the requirement.

3.2.2 RF-hybrid

The design of the RF hybrid has been done using the methodology presented by Matthaei and L. Young [42, 43]. Two different models of hybrids were taken into account, the synchronous and the periodical [42, 44, 45, 46] hybrid. The first design consisted in a 5-branch synchronous hybrid [44] since this model usually gives a good result using a lower number of branches. Note that the same number of branches was used in [47] but with the periodical approach. The problem with the synchronous approach is the small dimensions between the branches, making difficult its construction with a conventional milling machine. The main restriction coming from the use of the milling machine,instead of its precision [2], is the dimensions of the

[2]Note that the milling machine is an Computer Numerical Control (CNC) machine with five working axes with a precision of 1 μm

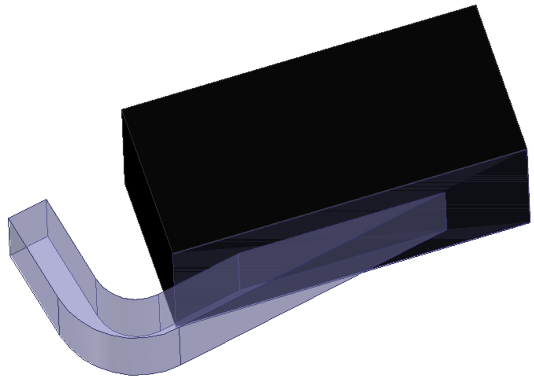

(a) Sketch of the RF load.

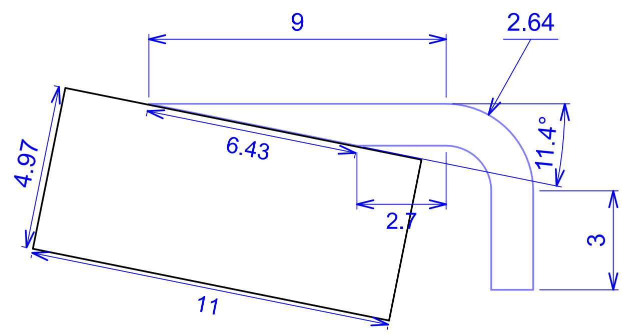

(b) Dimensions of the RF load in millimeters.

Figure 3.2: Sketch and dimension of the RF load.

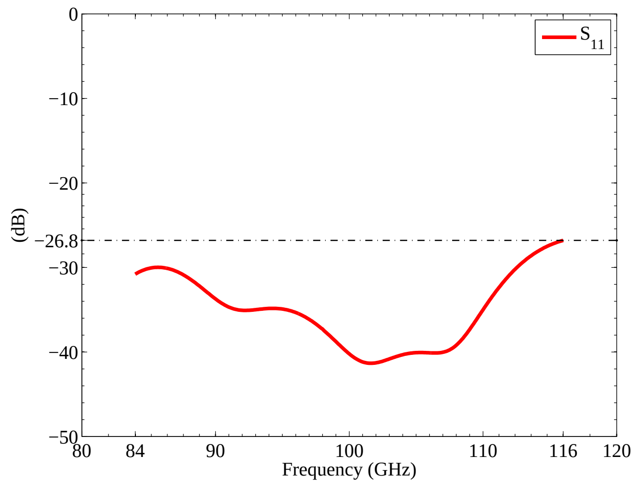

Figure 3.3: Simulation result of parameter S_{11} of RF load. The absorber ECCOSORB® MF-124 was selected.

tool used for fabrication. In general, the design of the components needs to comply with the following practical restriction,

$$w \leqslant 3d, \tag{3.1}$$

where w is the length and d is the diameter of the milling tool. This restriction ensures that it is possible to find a commercial milling tool that can be used for machining the component. With this restriction was not able to obtain a good performance and it was necessary a special milling tool. The new milling tool has $w = 6d$, with that it is possible to mill the hybrid branches of 0.2×1.27mm.

The design consists in a 9-branch periodical hybrid with impedance adaptation at each port. The impedance adaptation was designed using the model in [42, 48], with the goal to achieve the lowest reflection in the adaptation. The final design is presented in figure 3.4a.

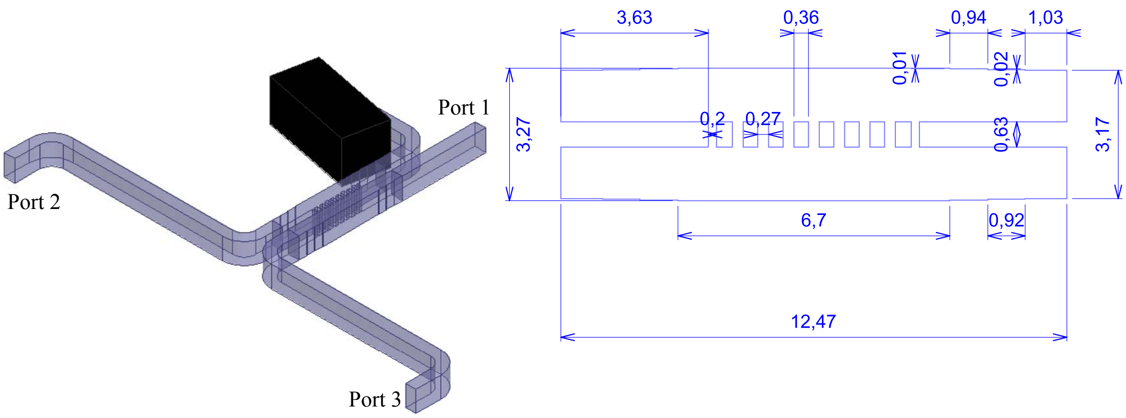

(a) (b)

Figure 3.4: Sketch and dimensions of the hybrid. (a) Sketch of the 90°hybrid coupler with one of the output ports terminated with a load. (b) Dimensions of the hybrid in millimeters.

The dimensions of the input and output waveguides correspond to the standard WR-10. In figure 3.4b the specific dimensions are presented.

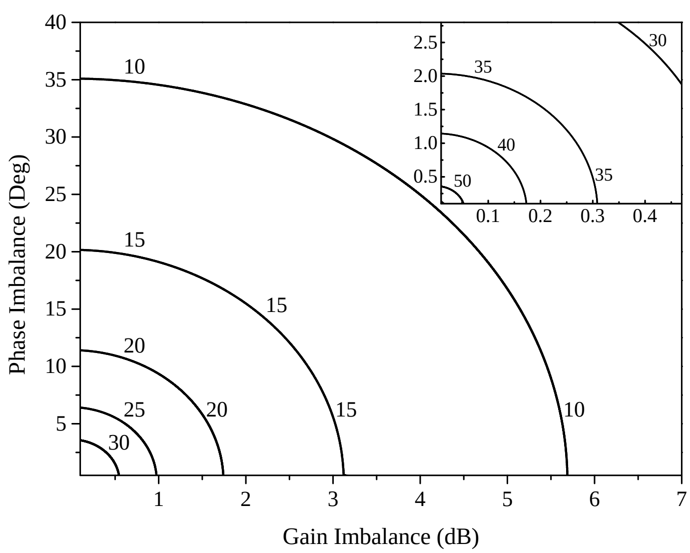

Figure 3.5: Image Rejection of a Single Sideband Separating Receiver.

To compare the performance of the hybrid we have used the relation for the sideband-separation rejection [22],

$$R(G, \phi) = -10 \log \left(\frac{1 - 2\sqrt{\Gamma}\cos(\Delta\phi) + \Gamma}{1 + 2\sqrt{\Gamma}\cos(\Delta\phi) + \Gamma} \right), \tag{3.2}$$

where Γ is the total gain and $\Delta\phi$ is the phase difference between the two IF outputs. Equa-

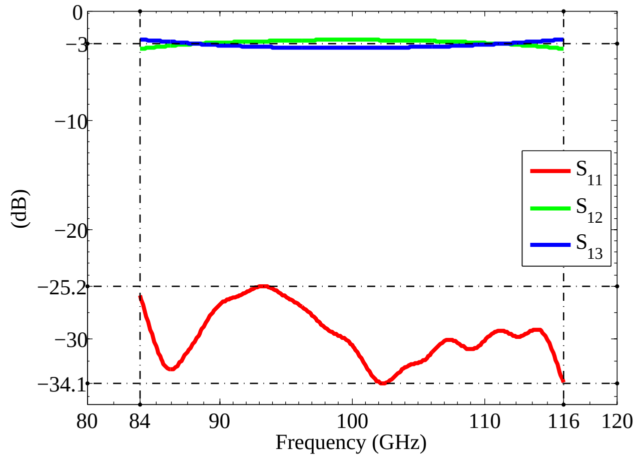

(a) RF Hybrid S paramenter simulated.

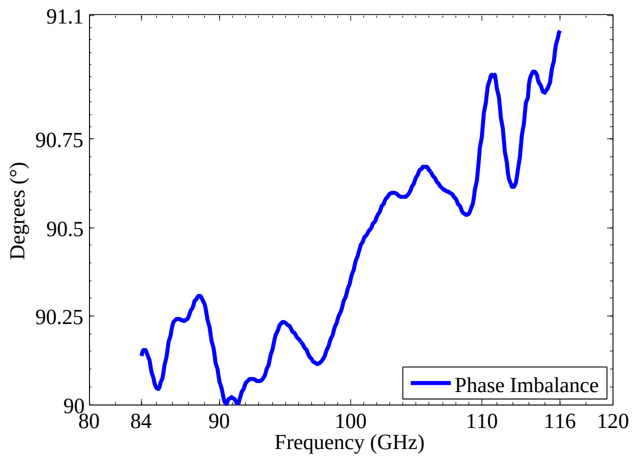

(b) Hybrid Phase Imbalance.

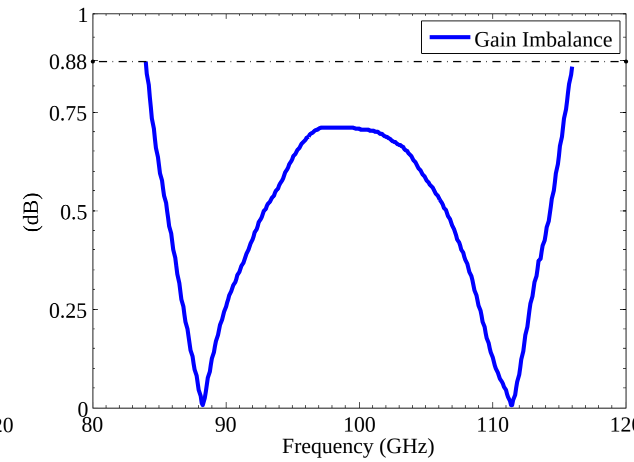

(c) Hybrid Gain Imbalance.

Figure 3.6: 90° RF Hybrid S-Parameters simulation from the figure 3.4a.

tion (3.2) is plotted in Figure 3.5 where we can observe the importance of having a good performance in gain and phase imbalances. For example, if we have a gain lower than 1 dB and a phase imbalance lower than 7.5 degrees, then a 25 dB of image rejection is expected. We also observe that by changing in 1 dB the gain imbalance the system can have a behavior worse than 5 degrees of imbalance. Taking this into account, it is very important to have the gain imbalance as low as possible in the whole frequency range for maximizing the image rejection. ALMA specifications establish that the image rejection of the system should be above 10 dB [49].

The results of the electromagnetic simulations of the hybrid are presented in figure 3.6. This figure shows the S parameters and the output phase shift. In particular, figure 3.6a shows the parameters S_{11}, S_{12} and S_{13}. The transmissions are centered at -3 dB which is consistent with theory [42], and with the results obtained for different ALMA receivers [47, 50, 51]. The reflections of the S_{11} parameter are below -25 dB. This is an excellent result as the design goal was to obtain a reflection below -20 dB, ensuring that less of 1 percent of the power is reflected. The phase of the hybrid outputs are bound between 90° and 91°, producing 1° of difference between the outputs ports 2 and 3. In figure 3.6b, the phase imbalance produced by the RF-hybrid is presented. The phase difference is less than

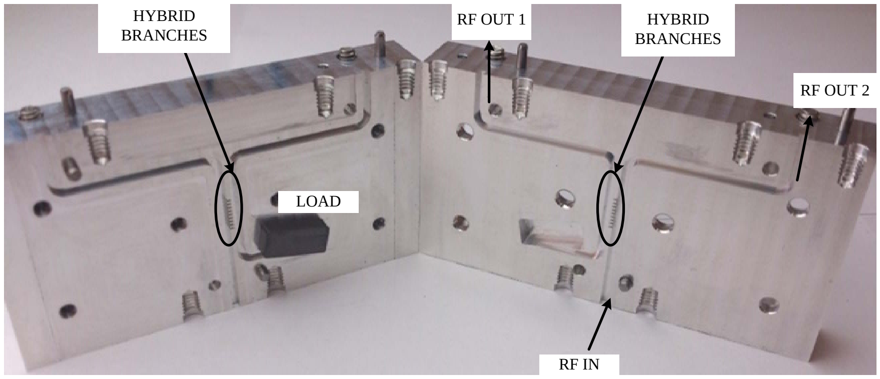

Figure 3.7: Half of the RF hybrid constructed using the split block technique. Also in this picture the designed and constructed RF load it is also been showed.

1 degree in the whole frequency range. The gain imbalance is presented in figure 3.6c where it is possible to observe that it is limited to less than 0.9 dB. Considering those values, the maximum image rejection (using figure 3.2) is around 25 dB.

Figure 3.7 shows the RF hybrid constructed in aluminium where it is possible to see the branches of the hybrid and the load for the fourth port. The figure presents one part of the structure which was fabricated using the split block technique. Individual test of this component was not possible given the experimental limitations of the laboratory.

From the data obtained in the simulation simulation of the RF hybrid and considering an IF hybrid with a gain imbalance and a phase imbalance of 0.75 dB and 8°, respectively, it is possible to estimate the sideband rejection using equation 3.2. Figure 3.8 shows the effect in the rejection ratio when the system has two mixers with different imbalances. The best case is when there are not imbalances between the mixers (green line) and the worst case evaluated is when the mixers add 2 dB and 10° of gain and phase imbalances, respectively.

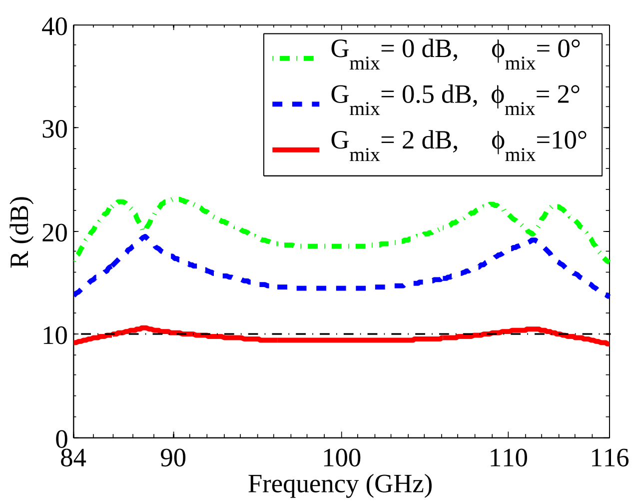

Figure 3.8: Estimation of the sideband rejection considering the values from the simulation of the RF-hybrid and the measurement of the IF-hybrid. The different lines represent the influence of the imbalances of the mixers in the sideband rejection of the system.

3.2.3 E-Plane Bifurcation

Figure 3.9a presents the design of the LO splitter. This component divides the LO signal into two signals with the same power and phase. The design of this component was performed following [52] and the equations presented in [48] were used as first approximation. Afterwards, the design was optimized using the electromagnetic simulation program HFSS [37]. The electromagnetic behavior is consistent with the practical design presented in [53]. The approach taken for our design is different from the design presented in [52] and [53], which uses a Y instead of a T for the E plane bifurcation. The dimensions of the waveguide in the E-plane bifurcation have the standard WR-10. The detailed dimensions are presented in the figure 3.9b.

For the E-plane bifurcation the expected result is to have the transmissions (parameters S_{12} and S_{13}) very close to -3 dB. The simulation results, presented in figure 3.10a, show indeed that the transmissions are very close to -3 dB in the band of 84–116 GHz. In the case of the reflections a value of less than -20 dB is expected. The simulations of our design show that we obtain -28 dB in the entire frequency range. The isolation between ports 2 and 3 is presented in the figure 3.10c: they are around the -6.15 dB and within the value range presented in [52]. Finally, the phase is stable in the band and centered around 0.65°. The E-plane bifurcation was finally built in duralumin, see figure 3.11.

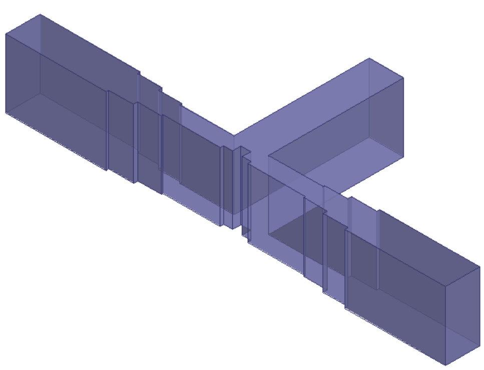

(a) 3D Sketch.

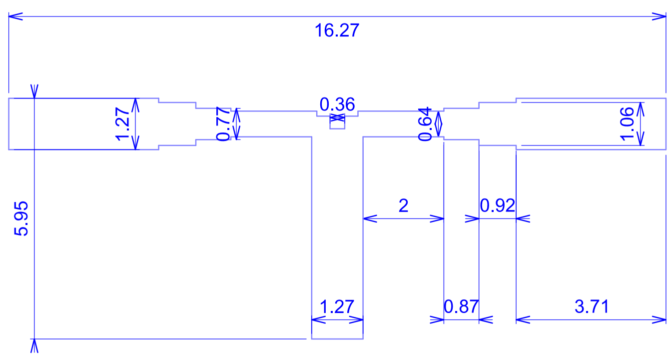

(b) Dimensions in millimeters.

Figure 3.9: 3D sketch and dimensions of the E-plane Bifurcation.

3.3 Integration of the analogue 2SB receiver

The integrated receiver is shown in figure 3.12. For amplification we have used a spare LNA amplifier from the SMWT. From a previous work [15] we have determined that the gain of the LNA is 5.9 dB at 115.2 GHz with $V_{\mathrm{d}} = 1.5$ V, $V_g = 0.25$ V and $I_{\mathrm{d}} = 27.44$ mA. As described above, the RF-hybrid and the LO-splitter were designed and constructed at Cerro Calan within the context of this thesis. The mixers were purchased to Millitech Inc. Nominally, these mixers are designed to work in the W-band, from 75 – 110 GHz, with an

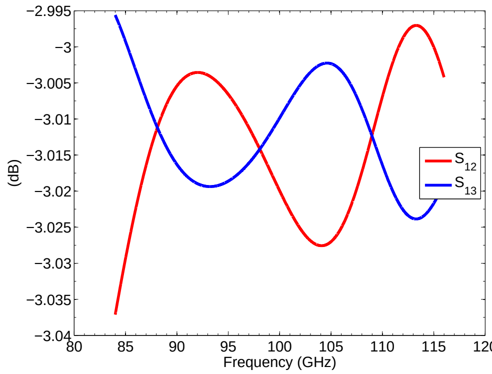

(a) E-Plane Transmission.

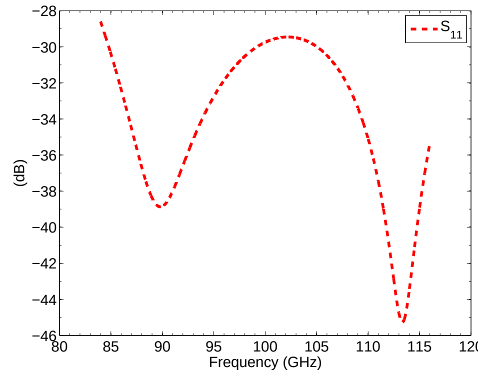

(b) E-plane Reflections.

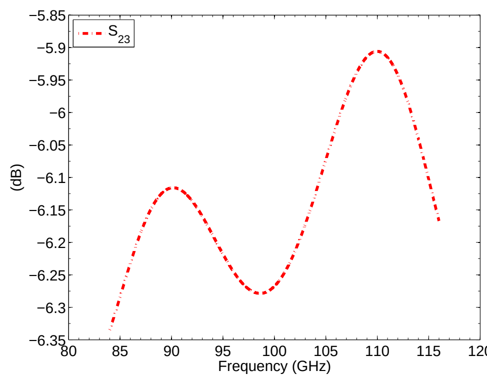

(c) E-plane Isolation.

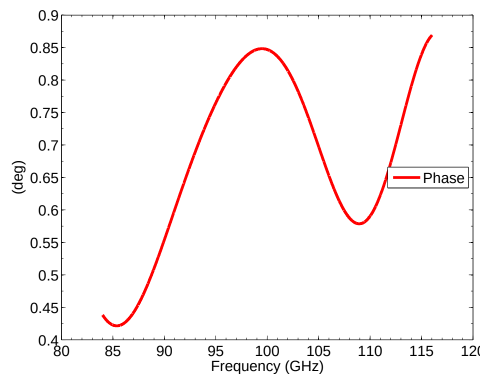

(d) E-plane Phase.

Figure 3.10: E plane Bifurcation S Parameter.

IF between 0.1 – 3 GHz and with a bias voltage of 15 volts, [24]. The RF an LO input are in the W-band in order to use the LO at 100 GHz. The IF-hybrid is from Miteq [54] and works from 0.8 – 4.2 GHz. The IF was selected to match the current IF of 1320 MHz in the telescope.

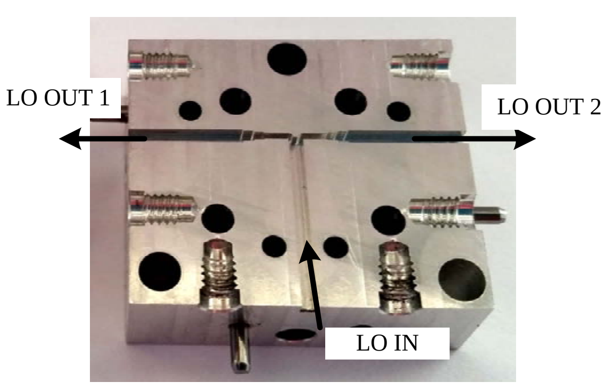

Figure 3.11: Implementation of the E-plane bifurcation made of aluminium using the split block technique.

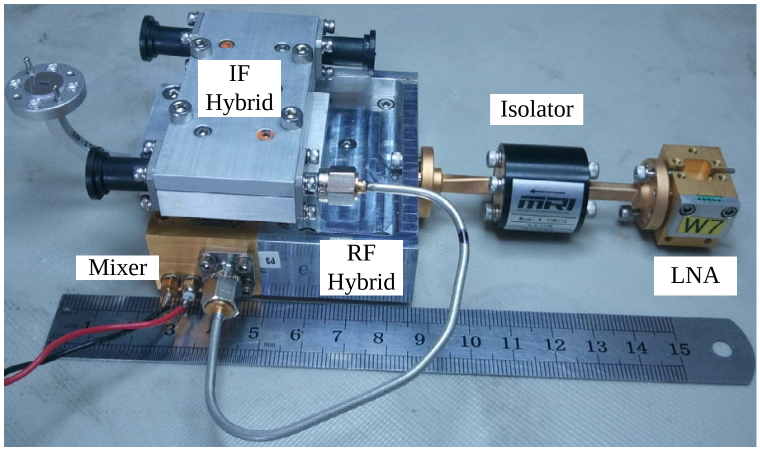

Figure 3.12: 2SB analogue receiver. Note that when the digital back-end is used, the IF-hybrid is not longer needed.

The useful space inside the dewar of the SMWT is a cylinder of 190 mm of diameter with 50 mm of height. In order to optimize the space, the IF hybrid was placed above the LO splitter and mixers, as shown in figure 3.12, connected by two rigid SMA cables with the same length in order to minimize the gain and the phase imbalances between the two outputs.

The input waveguide of the receiver has its E-plane perpendicular to the horizontal. Since the RF-hybrid and the E-plane bifurcation are designed with the E-plane of the waveguide parallel to the horizontal line, it is necessary to use a twist of 90° in order to match both waveguides. This twist increases the length of the receiver but it does not affect the design.

3.4 Test Setups

To characterize the receiver and its components, we have implemented the hot/cold method described in section 2.7.1 and the version of sideband rejection ratio measurement described in section 2.7.2. The two configurations presented in this work have been tested. The first one was the complete analogue 2SB receiver, while the second was implemented using the digital back-end designed by R. Finger [33].

In order to automate the different measurements some scripts and programs were programmed and-or modified in LABVIEW, MATLAB and PYTHON using Standard Commands for Programmable Instruments (SCPI) commands. For communication with the equipment we have used mainly ETHERNET creating a sub-net with the equipments and instruments. The instruments used in the different test setup are shown in the table 3.1,

3.4.1 Hot/Cold test

The hot/cold method requires two loads at different physical temperatures. The hot load is a piece of absorber at room temperature while the cold load is liquid nitrogen inside a box of

Table 3.1: Instruments used in this work.

Equipment	Brand	Model	Characteristics
Vector Netwrok Analyzer	Agilent	E8364C	10MHz - 50GHz
Spectrum Analyzer	Agilent	N9030A	3Hz - 50 GHz with an Harmonic Mixer extension capable to cover W-band
Signal Generator	R&S	SMB100A	9KHz to 3.2 GHz
Signal Generator	Agilent	E8257D	250kHz -20 GHz
Signal Generator	Anritsu	MG3604C	2-40 GHz
Source Power Supply	Keithley	2006A	Source Meter

expanded polystyrene. In order to automate the measurement a program in LABVIEW was implemented to control the signal generator, spectrum analyser, and a chopper motor which changes between the hot and cold (H/C) loads. The H/C measurement was performed with the receiver at room temperature only.

3.4.1.1 LNA Gain

The measurement of the LNA W7 has a starting point with the work of Nicolas Reyes. In that work [15] Reyes found the operational point of the LNA at room temperature. That work gave a gain around 5.9 dB in a operational point of $V_G = 0.25$ V and $V_D = 1.5$ V with a $I_D = 30$ mA at 115 GHz. The maximum drain current before burn out the amplifier is 30 mA. Nevertheless, the gain of the amplifier was measured again for this work. Figure 3.13 presents the setup. With the PSG and a harmonic mixer a tone is generated. First this tone is swept between 75 to 110 GHz without the LNA and the output power is measured with the spectrum analyser. This first measurement was used as calibration. Later, the same measurement was performed with the LNA, using the same parameters. Finally, subtracting both measurement we obtain the gain of the amplifier.

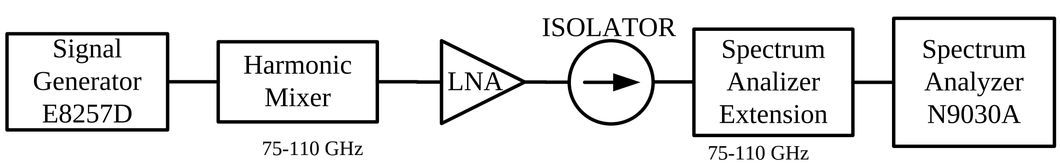

Figure 3.13: Sketch of test setup for the gain measurement. The tone is generated using an harmonic mixer as frequency multiplier ×6. The input frequency to the harmonic mixer is 12.5 to 18.3 GHz with a power of 6 dBm. The power supply is not shown.

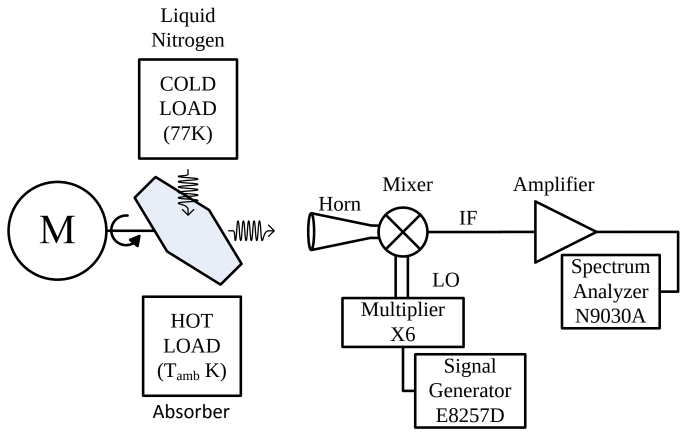

Figure 3.14: Sketch of hot/cold test setup for the mixers.

3.4.1.2 Mixer

The noise temperature of the mixer was determined using the scheme presented in figure 3.14. The LO is supplied by the PSG agilent E8257D and with the use of a $6\times$ multiplier it is possible to obtain the frequency range of $85-115$ GHz. The power of the LO is controlled by a variable attenuator and sensed by a power meter. The IF output is connected to the spectrum analyser N9030A which can measure the whole IF bandwidth (0.1 to 3 GHz). The mixer was biased by a constant DC power supply of 15 volts. A chopper changes between the hot and cold loads every $\sim$2 seconds. The motor is controlled by serial communication.

3.4.1.3 Mixer+LNA

The test setup for the mixer+LNA system is similar to the test setup for the measurement of the noise temperature of the mixers. In this setup, however, it is necessary to bias the LNA. For this purpose a Keithley power supply is used. An scheme of the setup is presented in figure 3.15.

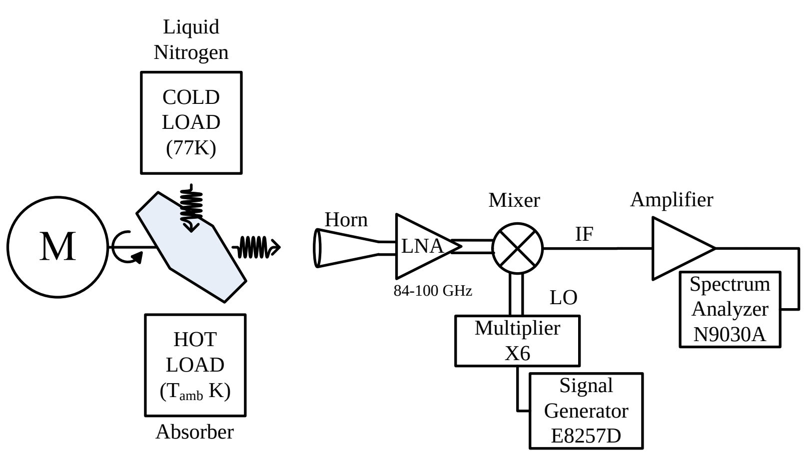

Figure 3.15: Sketch of hot/cold test setup for the mixers with LNA.

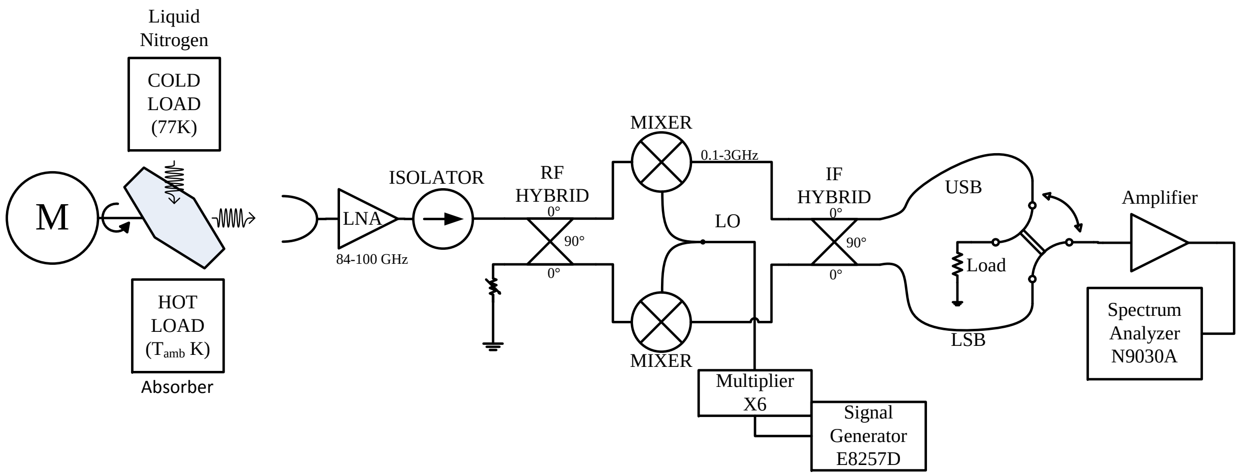

Figure 3.16: Scheme of hot/cold test of all analogue receiver. After the IF hybrid a switch is used in order to select the output port that will be measured in the spectrum analyser.

3.4.1.4 All-analogue 2SB receiver at room temperature

A scheme of the setup for measuring the noise temperature of the entire 2SB receiver is presented in figure 3.16. A horn was constructed in our facilities, within the context of this thesis, in order to couple in a better way the different loads. The chopper changed every couple of seconds the load and the power of the system was measured using a spectrum analyser.

3.4.2 Sideband Rejection Ratio in a mm-wave 2SB receiver

The receiver used in these measurements corresponds to the receiver presented in section 3.3. The SRR is measured directly at the IF output ports but it is compensated by the difference in the input power of the source as it was mentioned in section 2.7.2.

The general configuration of this setup consists of mounting the receiver with a horn over an optical table in order to get a better alignment, with the a second horn which is emitting the RF signal. Figure 3.17 shows a photograph of the analogue part in the general set up. In order to get the RF frequency, we have used an Anritsu PSG and an harmonic mixer as a frequency multiplier. The input power of the harmonic mixer was never more than 6 dBm. The LO is given by the combination of a Agilent PSG and a Millitech active 6× multiplier.

This measurement has been performed using the 2SB receiver with two configurations. The first is implemented using the IF hybrid obtaining an all-analogue 2SB receiver, and a second replacing the IF hybrid by a digital back-end [33] which includes a digital IF hybrid.

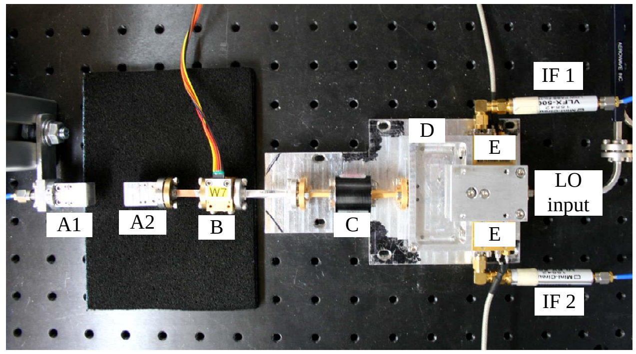

Figure 3.17: Picture of the 100-GHz receiver implemented at MWL showing the analogue RF components. (A1) Harmonic mixer and feed horn as RF source, (A2) horn, (B) LNA amplifier, (C) isolator, (D) RF hybrid and (E) mixers. The LO input and IF outputs are also shown.

3.4.2.1 Sideband Rejection Ratio of all-analogue receiver

The all-analogue RF receiver is formed by the 2SB receiver and an analogue IF-Hybrid. In this measurement the RF signal is swept between the frequency range of [LO-BW LO+BW], where bandwidth (BW) is the bandwidth so this interval corresponds to the LSB and USB part of the RF band. In figure 3.18 an scheme of the measurement is presented.

3.4.2.2 Sideband Rejection Ratio of 2SB receiver with digital Back-end

The test setups for 2SB receiver with digital back-end are practically the same as the setup used with the all-analogue receiver. The main difference is that we have replaced the analogue IF hybrid by the ROACH. Consequently, in the following setups, the spectrum analyser is not needed because the spectrometer is also implemented inside the ROACH.

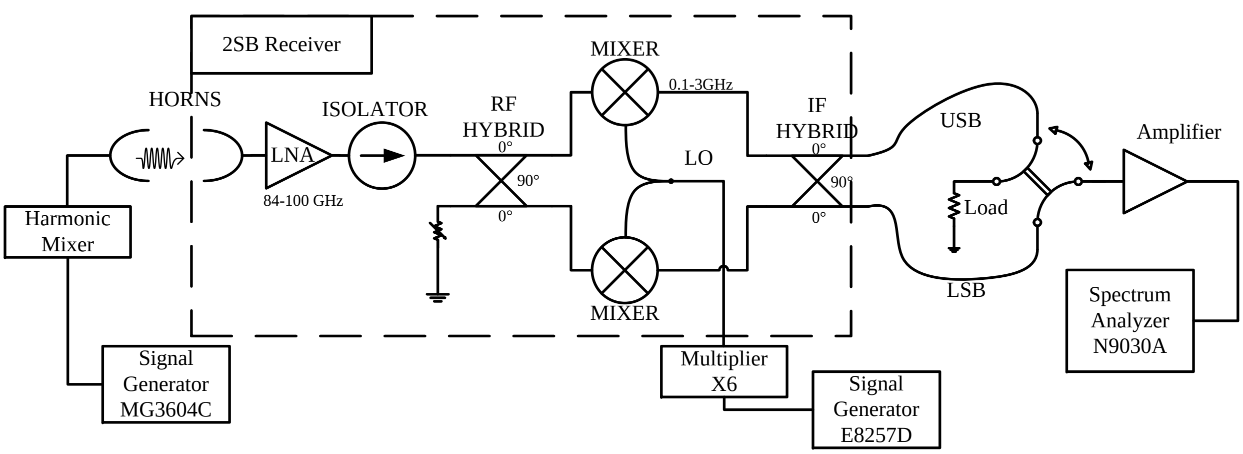

Figure 3.18: Scheme of the SRR measurement with an all analogue receiver.

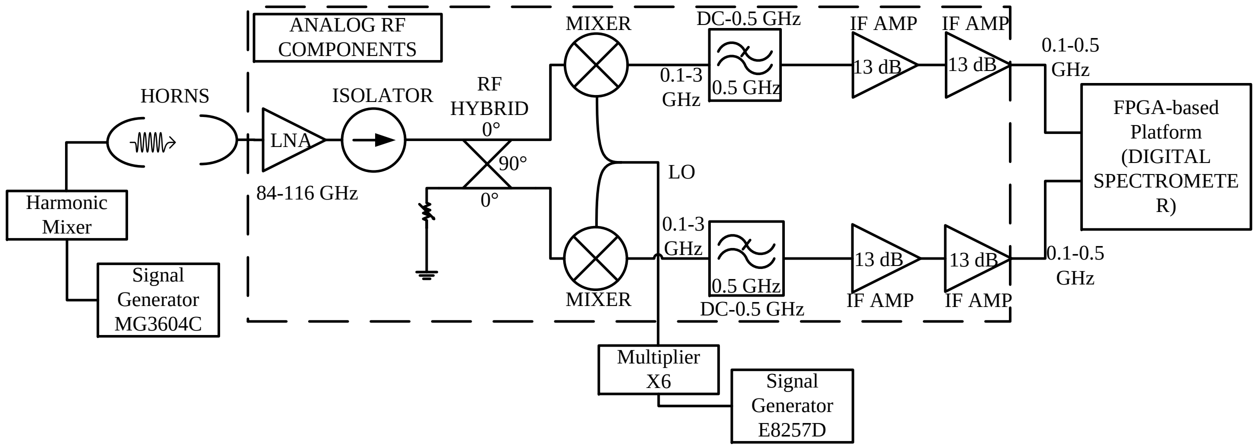

Figure 3.19: Scheme of the calibration setup for the digital hybrid constants. The IF amplifier are used in order to get the 0 dBm at the input of the ADC, this is the point where the ADC has the best performance.

3.4.2.2.1 Calibration of the Digital Hybrid

In order to get high levels of sideband rejection ratio, it is necessary to calibrate the model of the digital hybrid programmed inside the ROACH (see section 2.5). This calibration is performed by sweeping the RF source in frequency with a step related to the number of channels implemented in the digital spectrometer and the bandwidth in the intermediate frequency in this case there are 1024 channels with a bandwidth of 500 MHz, therefore the step in the RF source was 488.281 KHz. During the frequency sweep of the RF source, the ROACH measures the tone output power in the IF output produced by the RF tone . Then, the software inside the ROACH compares the output signals from the channels IF1 and IF2, characterizing the behavior of the analogue components. This characterization allows to determine the constants C_1 to C_4 in the model presented in section 2.5. These constants compensate the different imbalances presented in the analogue part of the receiver [55].

The setup of the calibration is presented in figure 3.19. It is important to notice that for every change in the LO frequency it is necessary to recalibrate the equipment since this defines another operational point.

3.4.2.2.2 Sideband Rejection Ratio with digital IF hybrid and spectrometer

The setup for measuring the sideband rejection ratio using the digital spectrometer is basically the same setup presented in the calibration setup. The only difference is that the constants that were determined during the calibration are loaded into the model inside the ROACH and the PYTHON script which executes the measurement.

3.4.2.3 Sideband Rejection Ratio with a second down-conversion and digital IF hybrid and spectrometer

Figure 3.20 presents the setup for the measurement of the sideband rejection ratio using the digital spectrometer with a second down-conversion over the IF. The procedure adopted for the measurement is similar to the previous cases. The main change is the presence of a second LO (LO_2), which down-converts the signal from the IF mixer.

This concept was proved in the 100-GHz receiver described above where the second LO is provided by the signal generator R&S-SMB100A with an RF power output of 18 dBm. The measurements were done at two LO_2 frequencies 2.0 GHz and 2.5 GHz covering the RF range of $[LO_1 - LO_2 - BW \ LO_1 - LO_2]$ and $[LO_1 + LO_2 \ LO_1 + LO_2 + BW]$. These intervals correspond to the LSB and USB part of the signal, respectively.

3.4.3 SRR in a sub-millimeter wavelength 2SB receiver at SRON, The Netherlands

Using the test setup presented in the section 3.4.2.3 as a proof of concept of the implementation of a second-down conversion, we proceeded to test the same concept in a complete functional 2SB receiver in the frequency band of 600−720 GHz. Figure 3.21 shows the setup implemented at SRON using a 2SB Band-9 ALMA receiver. In this setup the SRR measurement is performed using the method presented by Kerr [36] and described in section 2.7.2.2. The SRR is only implemented using a second down-conversion with digital back-end, due to the wide IF bandwidth of this receiver.

The setup used to characterize this receiver follows the same concept presented in section 3.4.2.3. It differs in the IF bandwidth, IF amplification, the RF, and LO sources. In this case, a new model in the ROACH with the capability of 1 GHz IF bandwidth was used. The Band 9 2SB receiver has a IF bandwidth of 8 GHz, between 4 to 12 GHz, and a RF bandwidth between 600 to 720 GHz. In order to cover all the RF bandwidth the LO_1 was

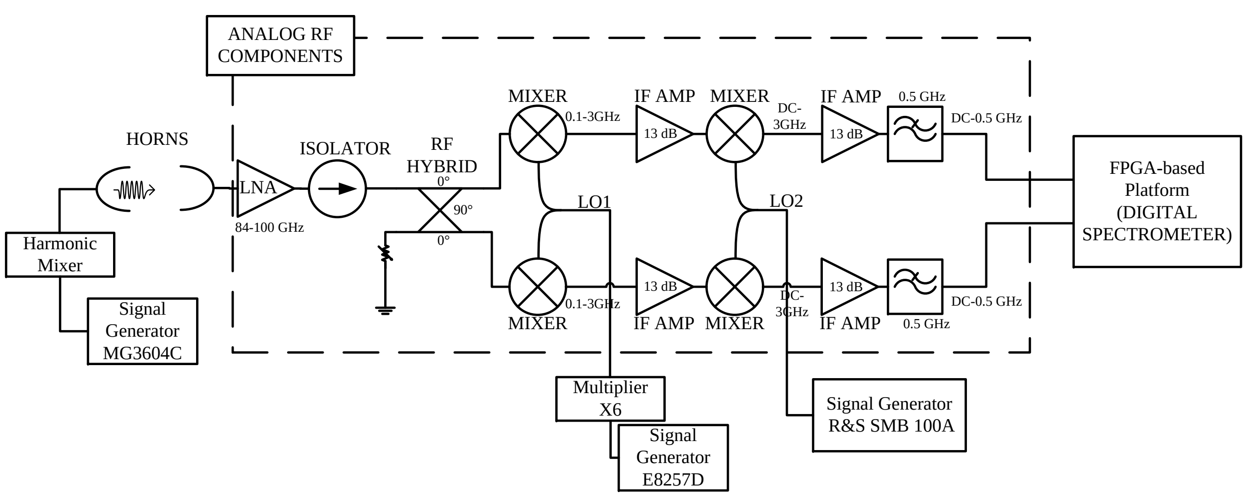

Figure 3.20: Scheme of the SRR measurement with a second down-conversion setup.

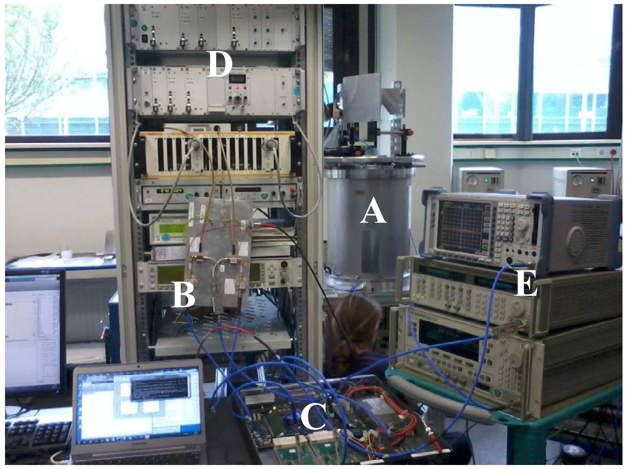

Figure 3.21: Picture of the experimental setup implemented at SRON. (A) Band-9 receiver inside the cryostat, (B) second down-conversion plate, (C) ROACH, (D) Band-9 electronics and (E) RF-sources.

moved between 614 to 710 in steps of 8 GHz, while the LO_2 was moved from 4 to 11 GHz in a step of 1 GHz.

3.5 Conclusions

In this chapter we have presented the design of the RF components of the 2SB receiver developed in this work. These components include the RF hybrid, the LO splitter and the RF load all where simulated and optimize using [37]. The designs achieved the performance goals when simulated. Due to technical considerations at the time of writing, an individual characterization of the components was not possible. However, their performance can be evaluated by the performance of the entire receiver as it will be shown in the next chapter. Furthermore, here we have also presented the measurement setups which were implemented at the MWL.

Chapter 4

Results and Measurements

The results of the measurement will be presented in three sections. The first corresponds to the measurement of the all-analogue receiver. The second section presents the results of measurements performed with the digital back-end and in the final section, preliminary measurements with two different receivers, using a second down conversion are presented. One of the receivers is the one presented in previous sections, in the context of this thesis, while the other one is a 2SB receiver for Band-9 of ALMA [56, 57, 58, 59, 60]. Notice that in this section we follow the definition presented in 2.7.2.

4.1 Analogue Components and All-Analogue Receiver

4.2 Gain of the Amplifier

The gain is around 17 dB from 75 up to 100 GHz. After this frequency the gain decreases rapidly. The measured gain of the W7 amplifier was performed using the setup described in section 3.4.1.1. The bias was set to $V_\mathrm{d} = 1.5$ V, $V_g = 0.25$ V and $I_\mathrm{d} = 27.44$ mA. The result is presented in figure 4.1.

4.2.1 Hot/Cold Test

4.2.1.1 Hot Cold Test of the mixers

This measurement was performed in order to determine the noise temperature of the mixers. The procedure we have used is presented in section 3.4.1. The most representative results of these measurement are presented in figures 4.2a and 4.2b. The noise temperature of the mixers was relatively difficult to obtain. The measurements turned to be very noisy, meaning that the variation of the power between the hot and cold was very low indicating that the

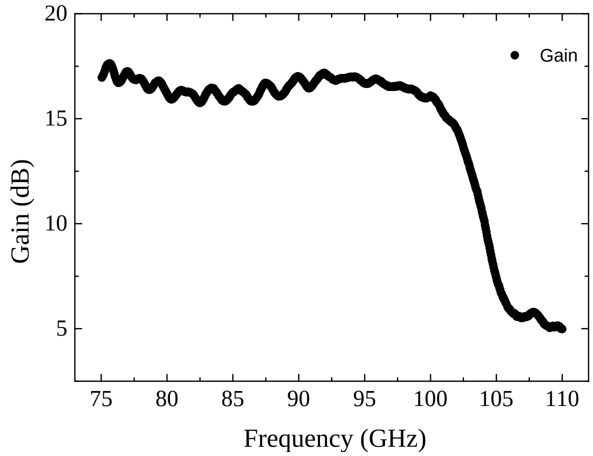

Figure 4.1: Gain of the W7 HEMT amplifier in W-band.

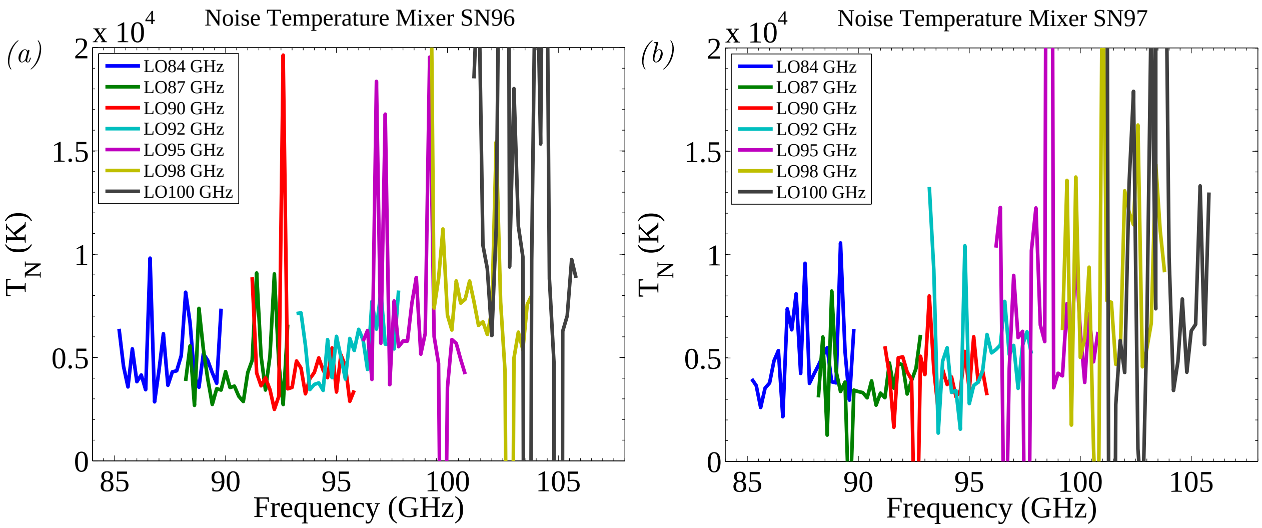

Figure 4.2: Noise temperature of mixers *(a)* SN96 and *(b)* SN97. Both measurements were performed at room temperature for different LO frequencies.

mixers have low sensitivity. The measured noise temperatures were of around 4000 K for the LO frequencies below 100 GHz and LO power between 3−5 dBm. For LO frequencies over the 100 GHz the noise temperature increases a lot, being impossible to obtain an accurate value. The behavior is similar in both mixers and no attempt of changing the mixer polarization was done. During the processing of the data the points corresponding to Radio Frequency Interference (RFI) were deleted. For more details see appendix A.

4.2.1.2 Hot Cold Test of the LNA + Mixer

In order to measure the noise temperature of the LNA and mixer, a procedure similar to the one described in the section 4.2.1.1 was used. The results are presented in figures 4.3a and 4.3b for different LO frequencies. The measurements show that the noise temperature of the system decrease considerably due to the gain of the amplifier. The noise temperature of LNA and Mixer for LO frequencies below 90 GHz are around 900 K. For LO frequencies

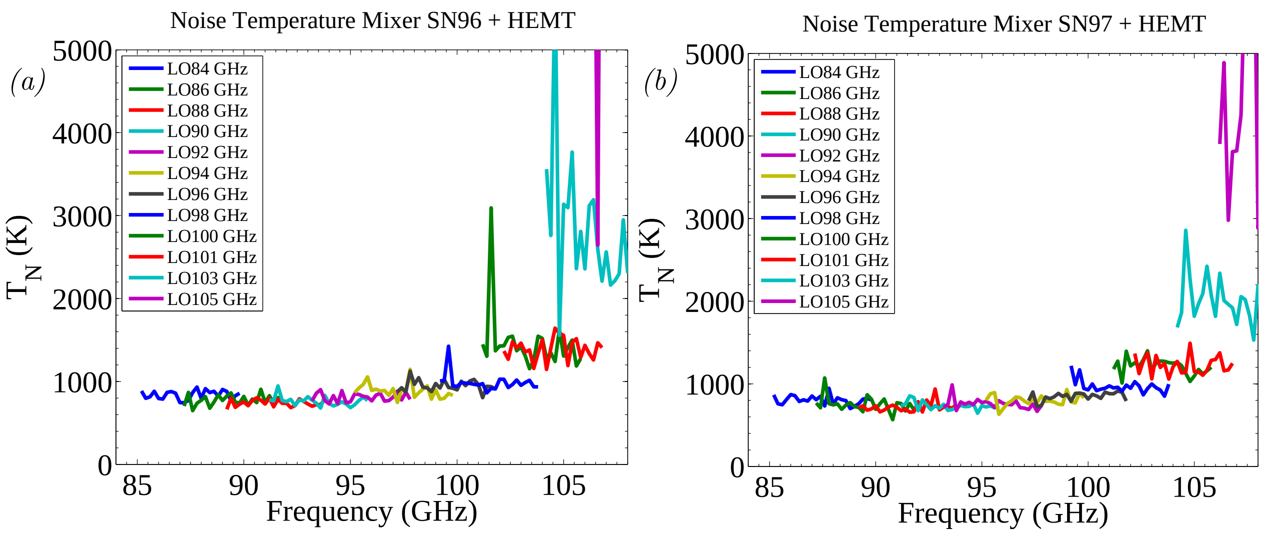

Figure 4.3: *(a)* Noise temperature of the System HEMT + mixer SN96. *(b)* Noise temperature of the System HEMT + mixer SN97. Both measurement were performed with the receiver at room temperature for different LO frequencies.

higher than 105 GHz the noise temperature increases considerably being impossible to obtain a good noise temperature of the system. This increment is consistent with the increment of the noise from the mixer and the decrease in the gain of the amplifier. Both systems, with mixers SN96 and SN97, present similar behavior in the noise temperature. No attempt of change in the biasing of the mixer was attempted. All the measurements presented here were performed at room temperature.

4.2.1.3 Hot Cold Test of the all-analogue 2SB receiver

The characterization of the all-analogue 2SB receiver considers the use of the IF hybrid. The measurement of the noise temperature of the all-analogue receiver followed the procedure presented in section 3.4.1.4. The noise temperatures of the whole system are consistent with the previous results and are presented, for different LO frequencies, in figures 4.4a and 4.4b. The LO frequency step was selected considering the IF bandwidth of 3 GHz. For frequencies above 100 GHz a similar result is obtained and it is extremely difficult to estimate a noise temperature.

The data presented in figures 4.4a and 4.4b correspond to the lowest noise temperature of the system obtained after sweeping in the LO power. Both outputs (LSB and USB) have similar behavior but it is possible to observe some differences.

Although the characteristics of this receiver have not been the best, it has served as a technology development and a testing tool to other innovative technologies as presented below. It also serves as a starting point for new developments using better mixers.

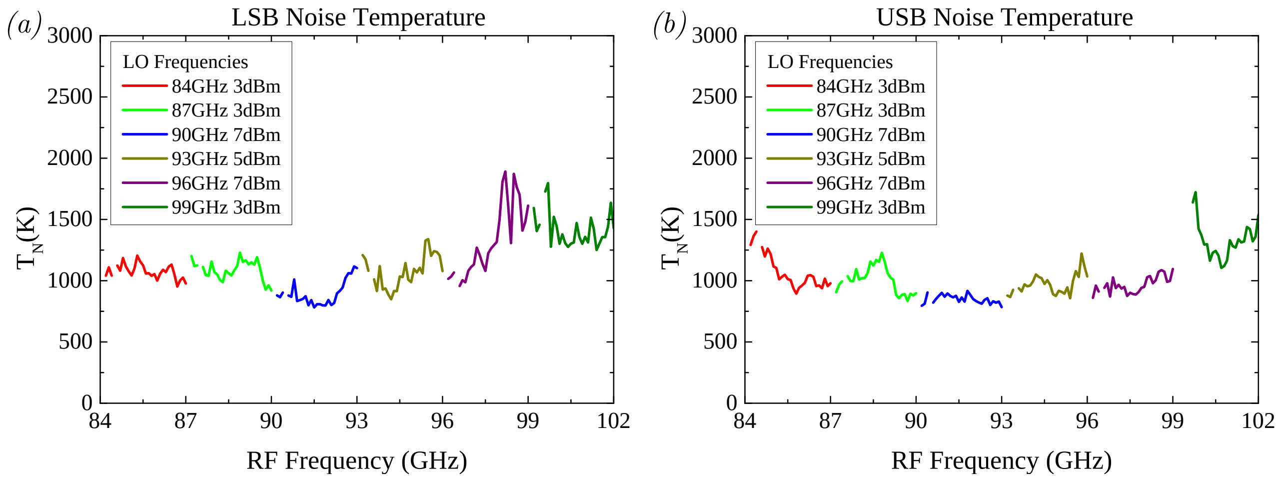

Figure 4.4: *(a)* Noise temperature for the LSB port. *(b)* Noise temperature for the USB port. The graphs shown considered the best noise temperature achieved in the system at different LO power.

4.2.2 Sideband Rejection Ratio of the all-analogue receiver

The measurement of the sideband rejection ratio of the all-analogue receiver followed the procedure presented in section 3.4.2.1. Figure 4.5 presents the sideband rejection of the receiver with the analogue IF hybrid. The sideband rejection is above 7 dB in the band of $84 - 100$ GHz, where the system presents the best performance. Notice that at different LO frequencies covering the same RF range the sideband rejection ratios are different. This is caused by mixers having different performance at different LO frequencies and power. No attempt was made to modify the biasing of the mixers in order to improve the sideband rejection. These results demonstrate that the components designed and manufactured by us operate within expectations.

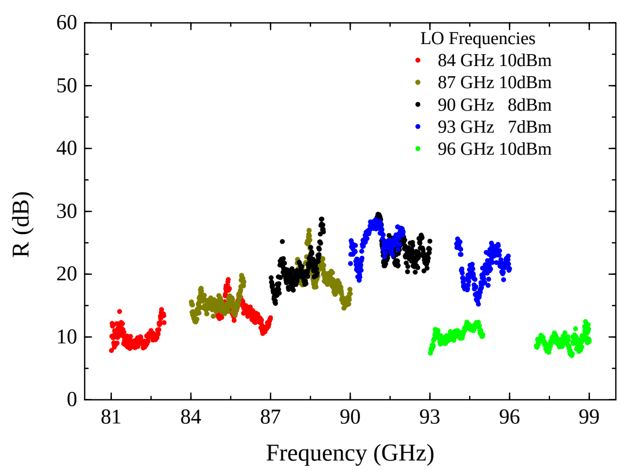

Figure 4.5: Sideband rejection ratio using an analogue IF hybrid for different LO frequencies. The LO power was optimized for best mixer performance.

4.3 Receiver with digital back-end

4.3.1 Calibration of the digital back-end

In order to use the digital back-end it is necessary to calibrate it. For this calibration we used the scheme presented in section 3.4.2.2.1. Figure 4.6a shows an example of the amplitude and phase imbalances measured with the digital spectrometer during the calibration. From these values the calibration constants are calculated. The measured values are rather noisy but a clear trend, which is drawn in solid lines, is visible. We attribute the origin of this noise to the fact that in the first implementation of the digital spectrometer there is no timing control in the data acquisition from the ROACH board to the computer. This noise appears in the presence of large phase noise in the LO and test RF signals that propagates into the IF signal. In our case, in order to get the frequencies around 100 GHz, it was necessary to use multipliers for LO signal and RF signal increasing the phase noise. Therefore, the measurements of the signal at the two output ports could be completely unrelated since they could correspond to measurements made at different times. This is, evidently, increased with a higher phase noise. Indeed, such noise was not visible in similar experiments performed at lower frequencies [55]. In order to verify this hypothesis the same measurement was repeated using a VNA. An example of such measurements is shown in Figure 4.6b. When the measurements are done without any synchronization between ports IF1 and IF2 (gray dots), noise appears in the phase and amplitude imbalances. This noise is very similar to the one appearing in the measurements performed with the ROACH-based spectrometer. When the measurements are synchronized (black dots), the noise disappears altogether. Having thus confirmed our hypothesis, a synchronization block was programmed inside the digital spectrometer. This block averts that the incoming stream of data enters to the memories while the data are being read by the computer. The calibration data with this improvement is presented in Figure 4.6c. The new calibration data are identical to the trend line presented in Figure 4.6a. but without any noise in the measurement.

4.3.2 Sideband Rejection Ratio

We measured the sideband rejection of the receiver using the digital spectrometer with the synchronization block used in 4.3.1, following the procedure described in section 3.4.2. The results are presented in Figure 4.7a. Rejections around 50 dB are obtained at the center of the band degrading to 35 dB at the edges. This degradation is not originated in the procedure presented here but in the degradation of the conversion gain of the mixers. To illustrate this situation we present in Figure 4.7b typical spectra obtained during the frequency sweep in the determination of the sideband rejection after calibration. We have defined the sideband ratio as the ratio between the tone in the correct sideband (peak A) to either the tone in the incorrect sideband (peak B) or the highest spurious (peak C), whichever is larger. Evidently, the conversion gain of the mixers deteriorates at the band edges resulting in a lower peak A and, consequently, lower sideband rejection ratio.

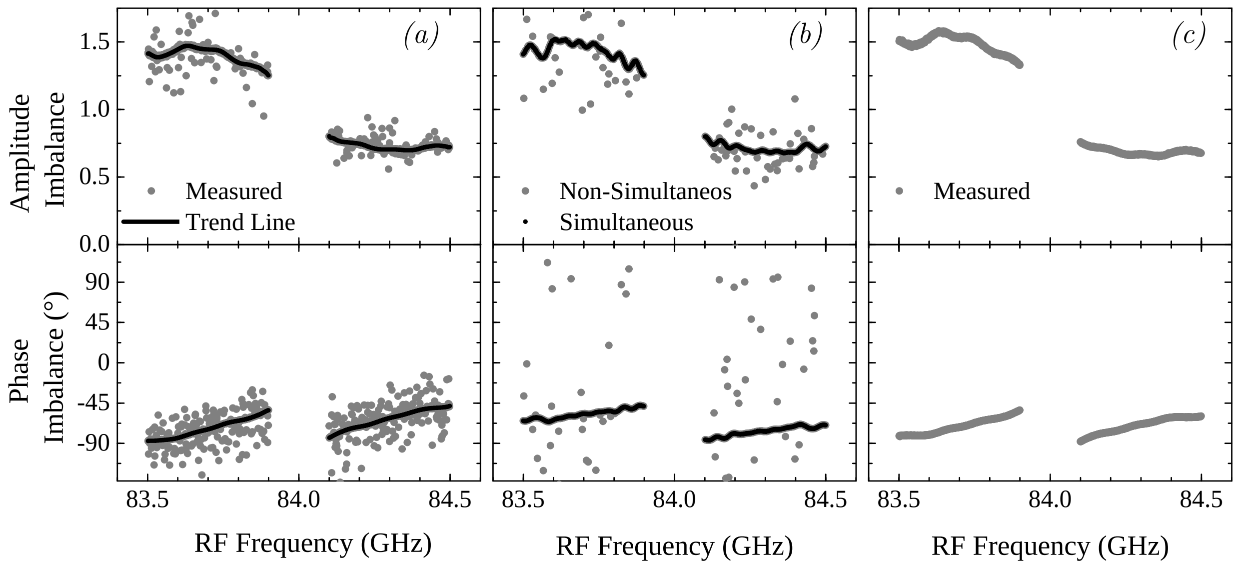

Figure 4.6: Amplitude and phase imbalances for an LO of 84 GHz. *(a)* Results of unsynchronized measurements with the digital spectrometer (gray circles) and their trend lines (black lines). *(b)* Results obtained with a VNA. The measurements were performed by reading simultaneously (black dots) and non-simultaneously (gray dots) the two IF ports of the mixers. Notice that the measurements performed with our ROACH-based spectrometer and the VNA are not exactly the same. There is an additional path difference when using the latter, as an extra adapting cable had to be introduced in both paths. *(c)* Results of synchronized measurements with the digital spectrometer.

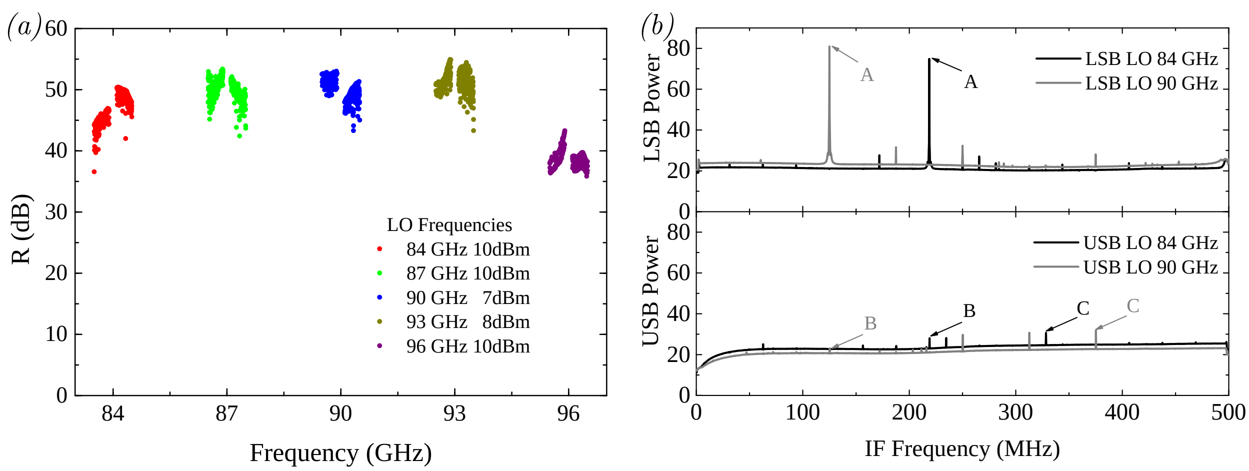

Figure 4.7: *(a)* Sideband rejection ratio for different LO frequencies using the digital spectrometer with synchronized data acquisition. *(b)* Typical spectra in the spectrometer while the sideband rejection is calculated. Peaks A, B and C correspond to the tone in the correct sideband, the tone in the incorrect sideband, and the highest spurious in the incorrect sideband, respectively. The sideband ratio is defined as the ratio between peak A and the highest between peaks B and C. The degradation in the sideband ratio is a consequence of the degradation of the amplitude of peak A.

4.4 Receivers with a second down-conversion and digital back-end

We have extended our measurements to receivers having a second down conversion. The first one is the 100-GHz receiver presented above. The second test was performed at SRON in Netherlands where a 2SB receiver for Band-9 of ALMA was used.

4.4.1 100-GHz 2SB receiver

4.4.1.1 Calibration

The calibration follows the procedure presented in previous sections 3.4.2.2.1. Examples of the calibration data for amplitude and phase are presented in Figure 4.8. The measurement was performed at an LO of 90 GHz considering two different second LOs, the first one at 2 GHz and another at 2.5 GHz. The data presented in figure 4.8 shows that there exist a standing wave in the calibration. This is due to the introduction of more components in the system, specially a second mixing stage and amplifier. Moreover, this produces an increment in the mismatch which is seen in the calibration.

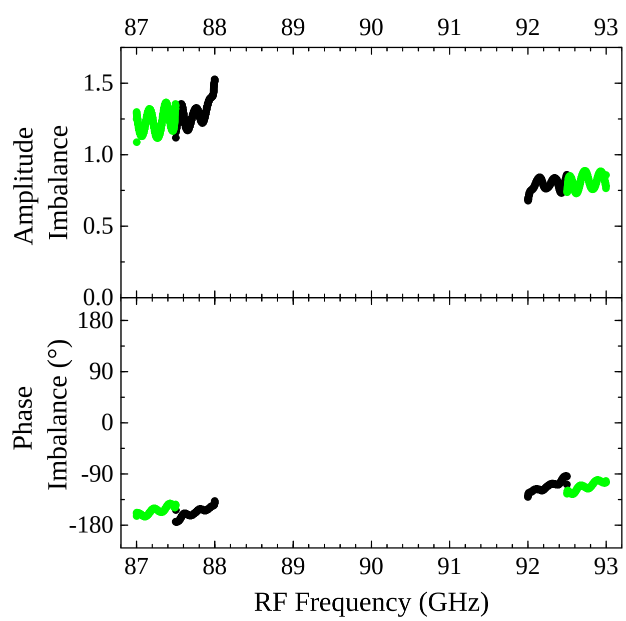

Figure 4.8: Typical calibration data for the system with second down-conversion. Black and green lines represent the calibration for an LO_2 of 2 GHz and 2.5 GHz respectively

4.4.1.2 Sideband Rejection Ratio

This measurement followed the procedure presented in section 3.4.2.3. Figure 4.9 shows an example of the sideband rejection ratios obtained when the second down-conversion stage is used. In this example LO_1 was maintained at 90 GHz while two different LO_2 frequencies were used. In other words, for each one of these cases, LSB and USB are further away, increasing the bandwidth of the system. Some degradation of the rejection ratios can be seen due to digital spurious not appearing before. However, values above 35 dB are obtained.

The degradation observed in the ratio is due to the presence of spurious signals. The rejection was calculated comparing the tone in the correct band to the highest tone in the other band, then, this represents the worst-case scenario in the ratio (see figure 4.10). Moreover, this spectrometer considers the channel 1024 where by digital effects there is always a fake tone during the measurements, and in the case of the second down-conversion, was variable in amplitude. Another source of noise in this measurement is the isolation in the splitter of the LO_2 source. Part of the LO_2 signal reflects from one mixer and goes to the other increasing the spurious signals.

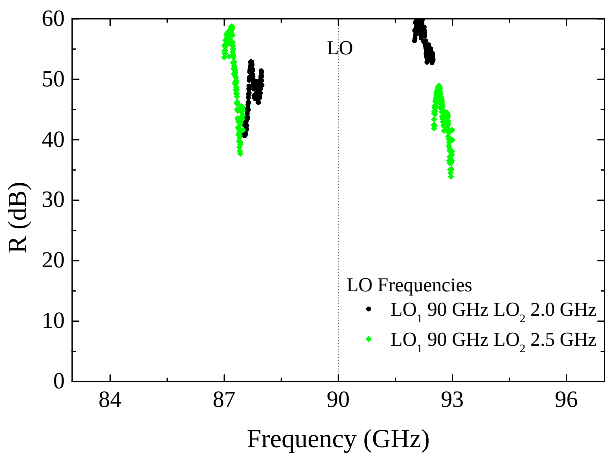

Figure 4.9: Image rejection ratio for two different second LO frequencies (2 and 2.5 GHz) with the corresponding first LO fixed at 90 GHz, using the digital spectrometer with synchronized data acquisition.

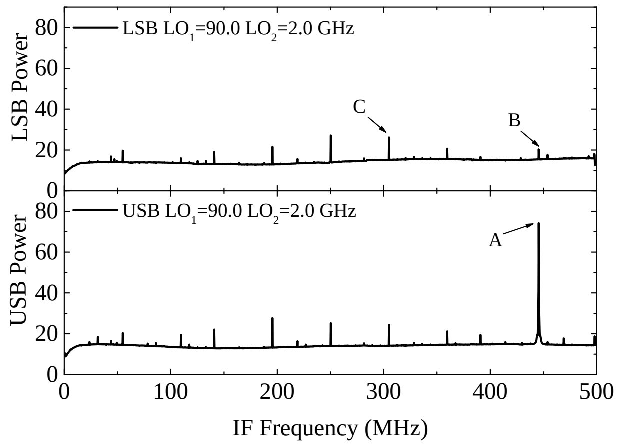

Figure 4.10: Typical spectra in the spectrometer while the sideband rejection is calculated. Peaks A, B and C correspond to the tone in the correct sideband, in the incorrect sideband, and the highest spurious in the incorrect sideband, respectively. The sideband ratio is defined as the ratio between peak A and the highest between peaks B and C. The degradation in the sideband ratio is mostly a consequence of an increment in the spurious.

4.4.2 ALMA Band-9 2SB receiver

The measurement with the ALMA Band-9 2SB receiver was performed at SRON, The Netherlands, during July 2014. In this way we were able to prove the concept of a digital back-end in a functional astronomical receiver.

4.4.2.1 Calibration

The operational frequency range of this receiver is from 600−720 GHz [56, 57, 58, 59, 60]. The calibration follows the same procedure presented in 3.4.2.2.1, with the difference that the IF bandwidth of the receiver is higher, 8 GHz (from 4 to 12 GHz). In this test the available IF frequency band of the spectrometer is 1 GHz (the double of the frequency presented in previous sections).

In order to sweep all the IF bandwidth, a different LO_2, spaced by 1 GHz (the width of the spectrometer), was used. Figure 4.11 presents the calibration data for LO_1 =654 GHz and eight different LO_2 (from 4 to 11 GHz). The values of the calibration vary with the different LO since a different LO_2 power represents a different point of operation in the mixers of the second stage. In the imbalances it is possible to observe a standing wave which corresponds to the second IF plate. The phase imbalance represents the total imbalance in the output ports of the second stage mixers, produced by both the RF and IF stages.

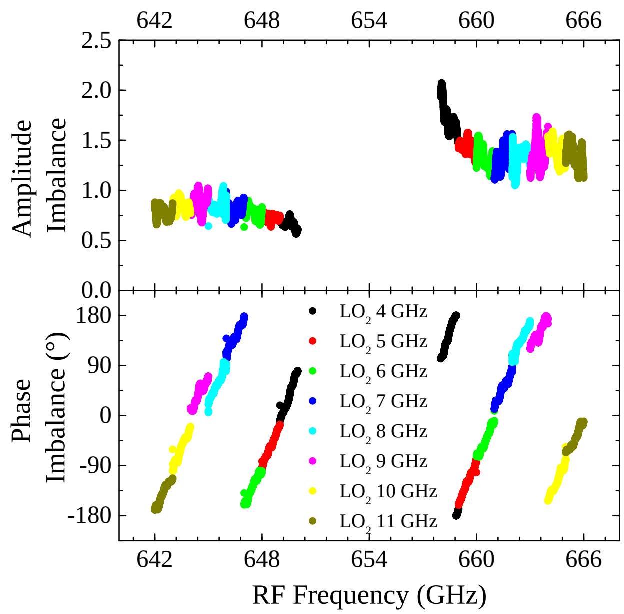

Figure 4.11: Typical calibration data for the system with second down-conversion. Dots represent the calibration data for LO_2 between 4 GHz and 11 GHz with a 1 GHz of bandwidth in the spectrometer, LO_1 is fixed at 654 GHz.

4.4.2.2 Sideband Rejection Ratio

Figures 4.12a and 4.12b present the rejection M at LO_1 with 8 LO_2 covering the total IF of the receiver. Notice that M is defined in equations 2.52 and 2.53 and does not require any kind of calibration for the frequency dependence of the RF source. The difference between the figures comes from how the ratio is calculated. Figure 4.12a considers the ratio between peak A and peak B (see Figure 4.13) while figure 4.12b considers the same ratio used in previous sections. The ratio is above 40 dB practically in the entire frequency band in both cases, which is at least 15 dB higher than the current analogue rejection in this receiver [56, 57, 58, 59]. The ratio obtained after the calibration corresponds to achieve an equivalent total imbalance less than 0.3 dB and 2° in gain and phase, respectively, in all the band.

Figure 4.13 shows a spectrum obtained during the measurement of the rejection. In this case the measurement considered the removal of the channel 1024, where the ghost tone was located. Also an improvement in the IF plate was considered. We have added attenuators in the splitter of the second down-conversion in order to reduce the spurious produced by the reflection of the LO_2 on the mixers. With these improvements the spurious were reduced considerably.

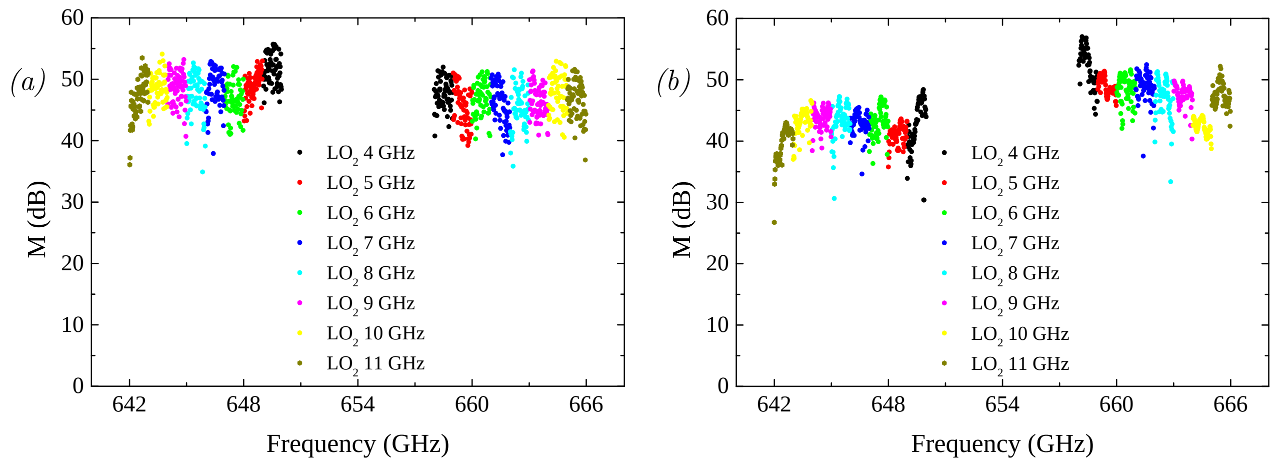

Figure 4.12: Rejection ratio for LO_1 at 654 GHz , sweeping the second LO between 4 to 11 GHz. *(a)* Rejection considering the ratio between the peaks A and B. *(b)* Rejection considering the ratio between the peaks A and the maximun between peaks B and C (figure 4.13).

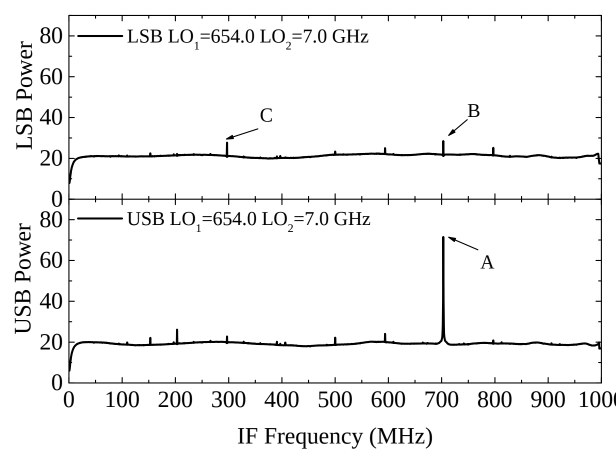

Figure 4.13: Typical spectra in the spectrometer while the sideband rejection is calculated. Peaks A, B and C correspond to the tone in the correct sideband, in the incorrect sideband, and the highest spurious in the incorrect sideband, respectively. The sideband ratio is defined as the ratio between peak A and the highest between peaks B and C. In this measurement also is considered the sideband rejection as the ratio between the peaks A and B, without considering any spurious peak like C.

Figures 4.14a and 4.14b present the sideband rejection ratio M for the entire RF frequency band. The ratio is higher than 30 dB and 25 dB for the entire band for each case. As before, the main difference is how the ratio was determined. Figures 4.14a and 4.14b consider in some way the best and worst case scenarios, respectively. From the 4.14b it is possible to conclude that the presence of intermodulation products in the spectrum add noise and decrease the sideband rejection ratio. This noise due to intermodulation products come from the multiple frequencies multiplier used in order to achieve the high frequencies of this receiver. Considering the best case, most of the points are above 40 dB and degradation is shown in frequencies lower than 620 GHz and above 700 GHz. Figure 4.14b presents a similar result to that obtained with the measurement performed at 100 GHz where similar intermodulation products were observed.

Finally, the sideband rejection ratio R, taking the best case (figure 4.14a), was measured using the procedure presented by Kerr [36]. The results are summarized in figure 4.15. It is important to note that using this procedure the degradation of the rejection in the limit of the band is not observed.

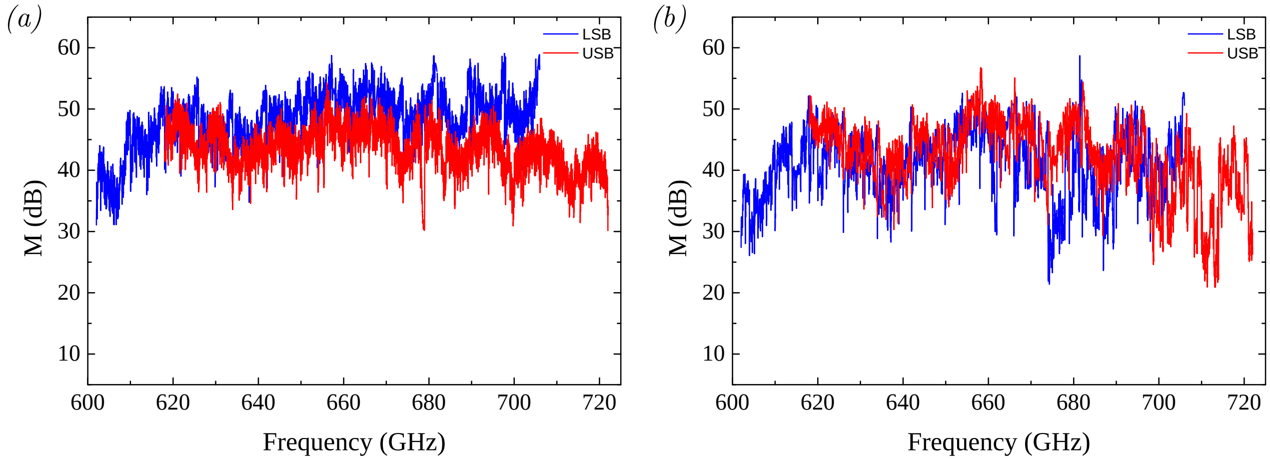

Figure 4.14: Image rejection ratio for all frequency band, sweeping LO_1 and LO_2 frequencies. Figures *(a)* and *(b)* consider the best and the worse case in the ratio.

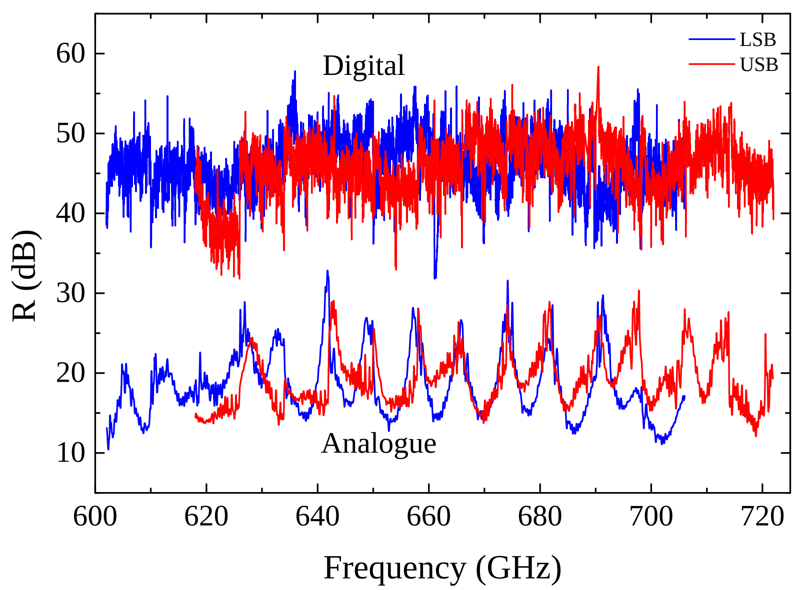

Figure 4.15: Comparison of the sideband rejection ratio for the entire frequency band, sweeping LO_1 and LO_2 frequencies. Both cases correspond to the sideband rejection obtained from the procedure presented by Kerr.

4.5 Conclusions

In the first part of this chapter the characterization of a 2SB all-analogue receiver and some of its components is presented. The noise temperature of the all-analogue 2SB receiver was below 1500 K at LO frequencies lower than 102 GHz. This performance is mainly limited by the low quality of commercial mixers used originally. This is solved in the preliminary work presented in Chapter 5. Finally, the sideband rejection of the all-analogue receiver was higher than 7 dB in the whole operation range for the 100 GHz receiver.

The second part of this chapter presented the sideband rejection of different configurations of 2SB receivers using a digital IF hybrid-and-spectrometer as a back-end. In all cases a sideband rejection ration above 35 dB was obtained. This is above any state-of-the-art all-analogue 2SB receiver [19, 61, 62].

Chapter 5

Improving the analogue 2SB receiver for the SMWT

In this chapter an improvement of the 2SB receiver will be presented. In particular, we will present the integration and preliminary results of the characterization of this receiver performed during November 2014.

5.1 Design, Construction and Integration

The improvement of the receiver considers two new mixers. These mixers are sub harmonically pumped mixers from Virginia Diodes, Inc. (VDI) and were tested at 77 K. The specifications of the mixers provided by VDI are presented in figure 5.1.

The use of these new mixers imply changes in the design such as changing the LO source and designing a new LO-splitter. The design was based on the LO-splitter presented in section 3.2.3. The new design started by scaling the previous design. It was afterwards optimized using the electromagnetic simulation program HFSS [37]. Figure 5.1 presents the new LO splitter. The dimensions of this component is bigger than the one presented in section 3.2.3 mainly because the new LO frequencies are lower and the relative location of

Table 5.1: General Specifications of the VDI Sub Harmonic Mixers.

Parameter	Specifications	Interface
RF input	75−110 GHz	WR-10
LO input	37.5−55 GHz	WR-20
IF input	16 KHz−11 GHz	2.9 mm
LO Power (Optimal/Damage)	2−4 mW/8 mW	
RF Power (Optimal/Damage)	$<100\mu$W/1mW	
Typical Noise Temperature	400−800 K	
Typical Conversion Loss	<7 dB	

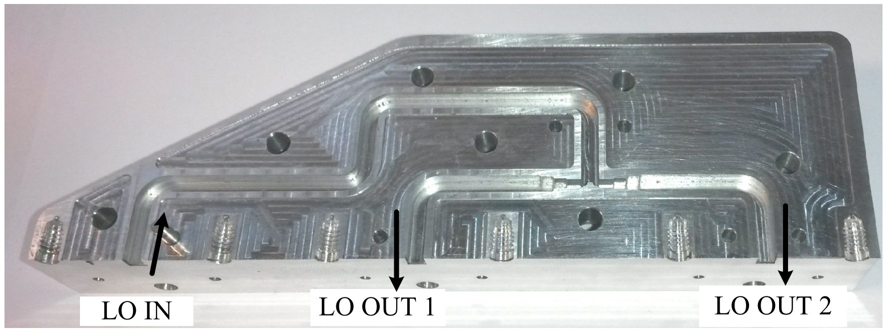

Figure 5.1: New implementation of the E-plane bifurcation made of aluminium using the split block technique. The dimensions of the waveguide are 4.775 $\times$ 2.388 mm.

the RF and LO port of the mixers.

A new LNA, with better performance, was used in this improvement. This LNA comes from a collaboration with CALTECH and is physically equal to the LNA used in the previous receiver design presented in Chapter 4. Therefore, no mechanical changes in the RF hybrid were needed. The integrated receiver inside the test-cryostat is shown in figure 5.2.

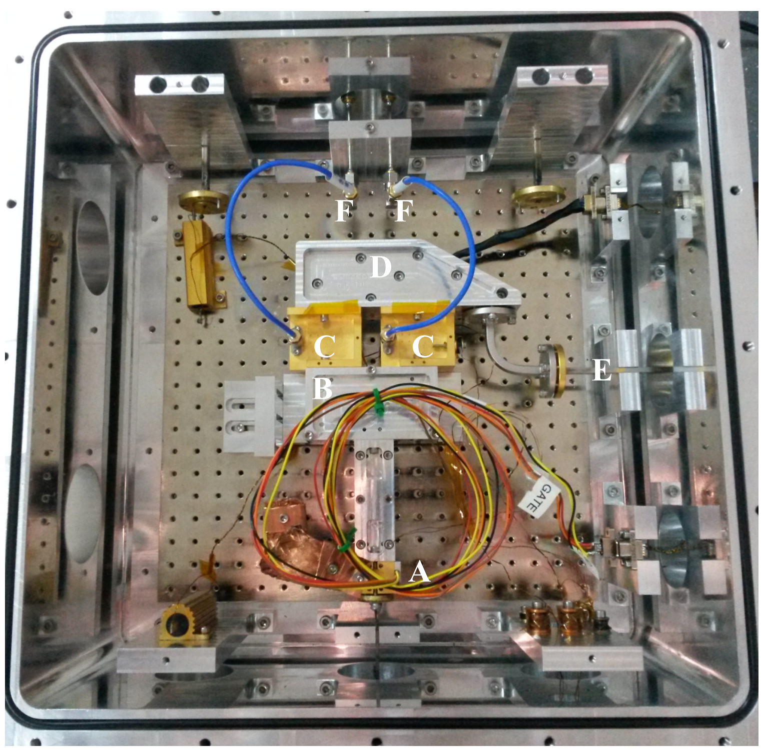

Figure 5.2: Picture of the improved 2SB receiver, mounted inside a test cryostat, showing the analogue RF components. (A) LNA amplifier, (B) RF hybrid, (C) mixers, (D) LO splitter, (E) LO input and (F) IF output.

5.2 Preliminary Results

The mixers were also characterized at room temperature. To characterize this receiver we measured its noise temperature and sideband rejection in conjunction with the digital back-end. The noise temperature of the improved receiver was measured in the test-cryostat at 77 and 20 Kelvin. The material used as isolator interface between inside and outside the cryostat is a thin layer of 75 μm of Mylar. The horn was located outside of the test-cryostat at room temperature. For the sideband rejection test, the measurement was performed at room temperature.

5.2.1 Hot/Cold test

5.2.1.1 Hot/Cold test of the mixers

This measurement was performed in order to determine the noise temperature of the mixers and corroborate a better functionality than the previous mixers. The procedure we have used was presented in section 3.4.1. The preliminary results of this measurement are presented in figures 5.3a and 5.3b. Since these measurements were performed at room temperature, the noise temperature of the mixer is higher than presented in table 5.1 in the specifications. However, the noise temperatures obtained are much lower than the noise from the previous mixers. Another important point is that in these measurements lower levels of RFI were observed, mainly due to the change of the IF-amplifier power supply.

5.2.1.2 Hot/Cold test of the System

The characterization of this receiver did not consider the use of IF hybrid, then the results correspond to a DSB noise temperature. The measurement of the noise temperature followed

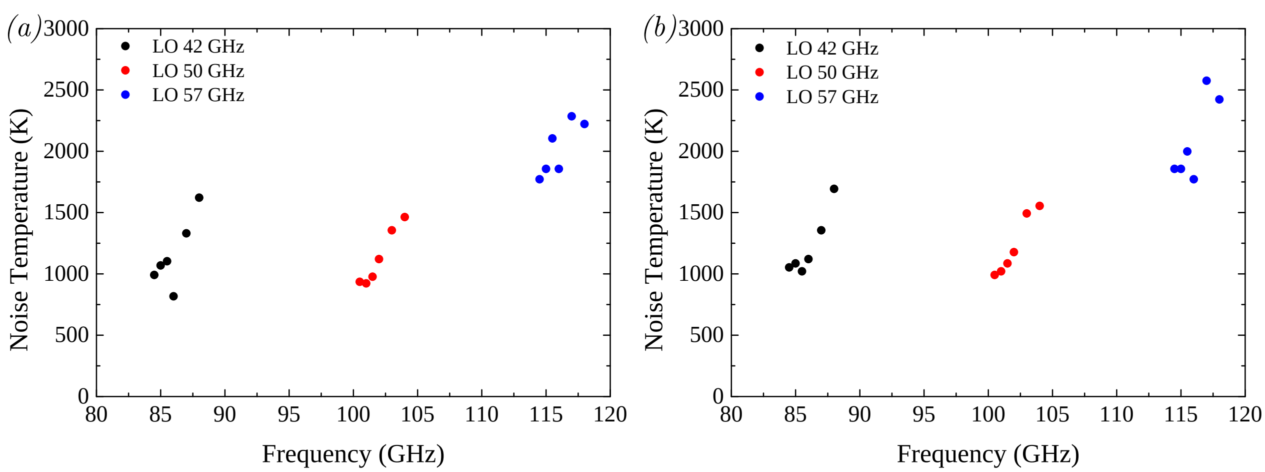

Figure 5.3: Noise temperature of mixers *(a)* VDI-1-35 and *(b)* VDI-1-37. Both measurements were performed at room temperature for different LO frequencies.

the procedure presented in section 3.4.1.4. Moreover, this test is performed inside the test cryostat at 20 and 77 K.

The preliminary results at 77 K are shown in figure 5.4. The noise temperature of the system with the CALTECH-14 is in the range of 200 to 500 K. Both outputs present similar temperatures. Notice that the system considers the horn outside the cryostat and the performance of the components as the LNA and mixers are not optimized. Then, in order to obtain a correct noise temperature of the receiver it is necessary to discount the noise introduced by the components before the LNA and search for the optimal LNA bias and LO power. In particular it is required a good characterization of the losses introduced by the 75μm layer of mylar and it is estimated to be about 100 K with a loss about of 2 dB. This will be performed in future measurements. Other changes consider replacing the current mylar for a thinner mylar of 12 μm.

Figure 5.5 shows the preliminary results of the noise temperature of the system at 20 K. The noise temperature is in the range of 180 to 450 Kelvin. This measurement has the same considerations of the measurement at 77 K. Then, more tests must be performed in order to obtain the correct noise temperature of the reciever. In fact, the noise temperature presented in figures 5.4 and 5.5 show the worst case for the receiver and is totally possible to improve the performance presented.

5.2.2 Receiver with digital back-end

5.2.2.1 Calibration of the digital back-end

In order to use the digital back-end it is necessary to calibrate it. For this calibration we used the scheme presented in section 3.4.2.2.1. The measurement was performed at room temperature since the calibration of the digital IF-hybrid compensate any imbalances in the RF stage. Therefore, the sideband rejection must be similar, both at room and cryogenic

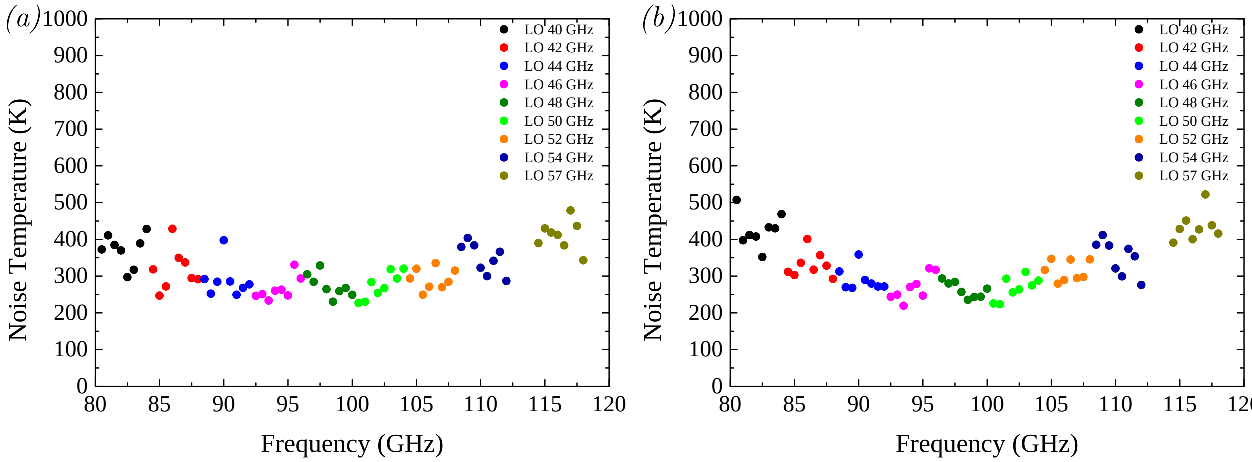

Figure 5.4: Noise temperature of system. *(a)* Mixer VDI-1-35 and *(b)* mixer VDI-1-37. Both measurements were performed at 77 K for different LO frequencies.

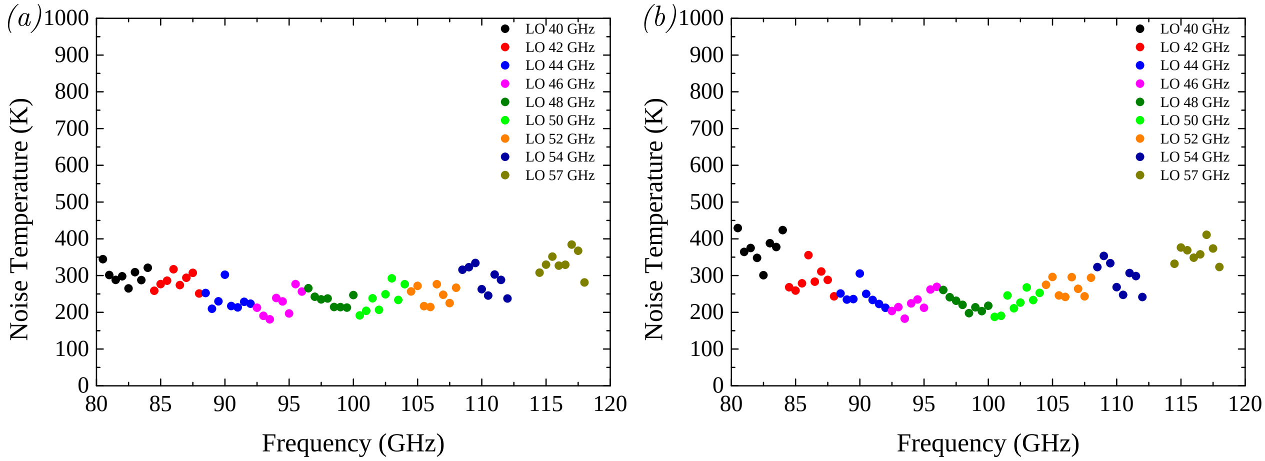

Figure 5.5: Noise temperature of system. *(a)* Mixer VDI-1-35 and *(b)* mixer VDI-1-37. Both measurements were performed at 20 K for different LO frequencies.

temperatures, only the calibration being different due to the changes by thermal contraction and performance in the components produced by changes in the temperature.

Figure 5.6 shows a calibration of the new receiver. The measurement was performed at an LO of 90 GHz with a IF bandwidth of 500 MHz. Differences in the imbalances can be observed with respect to other calibrations in previous sections, mainly since this is a new receiver (we have changed the mixers and the LNA).

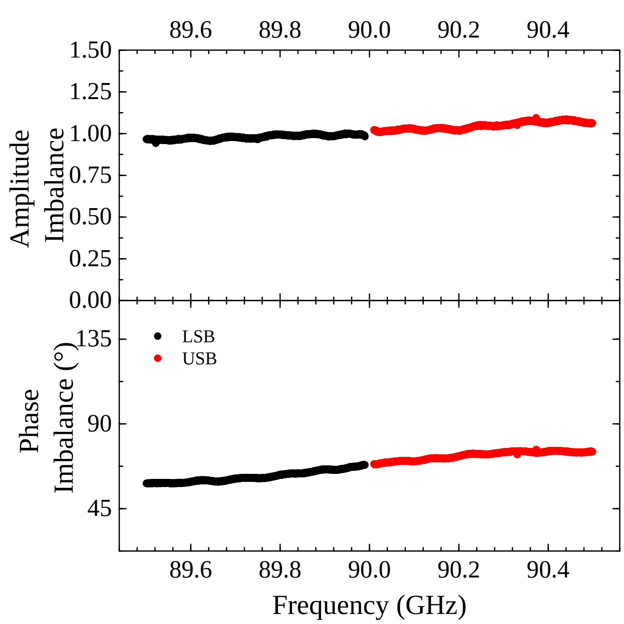

Figure 5.6: Amplitude and phase imbalances for a LO of 90 GHz.

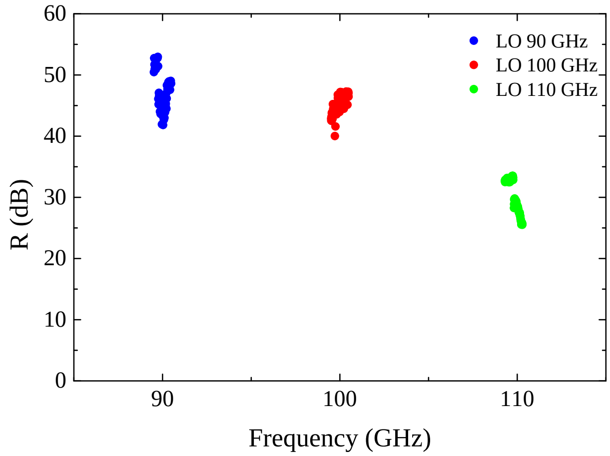

Figure 5.7: Sideband rejection ratio for different LO frequencies using the digital hybrid and spectrometer.

5.2.2.2 Sideband Rejection Ratio

We measured the sideband rejection of the receiver using the digital spectrometer following the procedure described in section 3.4.2. Figure 5.7 shows the preliminary result of the sideband rejection ratio. The SRR drops from 48 dB to 30 dB, when changing the LO from 90 to 110 GHz. The SRR is similar between at LO frequencies of 90 and 100 GHz over 40 dB. The lower ratio presented in 110 GHz is due to the decrease of the dynamic range in the IF output. This can be solved increasing the IF amplification. Notice also that we have defined the sideband ratio as the ratio between the tone in the correct sideband to either the tone in the incorrect sideband or the highest spurious, whichever is larger.

5.3 Conclusions

In this chapter we have presented the preliminary results of the improved analogue 2SB receiver for the SMWT. These results are promising. The new LNA and mixers show a great performance and excellent noise temperatures. The noise temperature of the mixers (without any amplification) at room temperature are lower than 2500 K for all frequencies range meaning 2000 K lower than the older mixers for frequencies below 100 GHz. This translate to a system noise temperature, at 77 K, of around 300 K. It is, therefore to achieve a competitive astronomical receiver for SMWT. It is important to keep in mind that the results presented in this Chapter are preliminary and more tests must be performed in order to obtain the best operational point for astronomical observations.

Chapter 6

Summary of the Conclusions and Future Work

In the present work we have implemented a millimeter-wave 2SB receiver in two configurations, an all-analogue version and a version where the IF hybrid is implemented digitally. The philosophy of design behind the analogue part of the receiver was a modular one, combining commercial with custom-made components. We designed and fabricated key components as the RF-hybrid, the LO splitter and an RF load. Other components such as mixers, IF-Hybrid, amplifiers and filters were purchased commercially or acquired through collaborations. All of these components were integrated in a functional receiver that was tested at the Millimeter Wave Laboratory (MWL) in Cerro Calán. The sideband ratio of the all-analogue 100 GHz receiver version was above 7 dB in the whole frequency range, demonstrating that the custom-made components performed well into specifications. This result is, in fact, consistent with other state-of-the-art astronomical receivers. The receiver presented very high noise temperatures due to the poor performance of the commercial mixers and low gain of the amplifier. As preliminary demonstrated by recent work, presented also in this thesis, by using a state-of-the-art RF amplifier a much better performance was demonstrated. This new receiver will be installed inside the SMWT with the digital IF hybrid and will be used for scientific purposes.

The original front end, except for the IF analogue hybrid, was used to demonstrate a digital 2SB receiver. The first tests presented problems with the data acquisition, specifically with the synchronization when reading of the data. The presence of several frequency-multiplication stages incremented the phase noise. This issue was solved by adding a synchronization block in the program flow. In this way was possible to obtain an image rejection of 50 dB at the center of the RF band with some degradation at the band edges, but always above 35 dB, in stark contrast with the values obtained when using an analogue IF hybrid where in the best case it was possible to obtain only 30 dB. Moreover, tests using a second down-conversion in the IF were implemented increasing the potentiality of the receiver with the digital back-end incorporated.

The developments made with the millimeter-wave receiver presented here allowed us to test this concept in a functional 2SB receiver developed by SRON for ALMA. These tests proved the high potential of the calibrated IF hybrid in order to reach high sideband rejection ratios, improving considerably the performance of the receiver. In this case ratios above 40 dB for the entire band were obtained, an improvement contribution to the development of the improved ALMA Band-9 2SB receiver.

It is important to note that in both cases we have used two mixers whose conversion gains were not matched. We envision that using the technique presented here, matching the gain of mixers to be used as 2SB converters will not be needed. This demonstrates the enormous potential that digital platforms have for astronomical instrumentation.

In order to continue with the project, the receiver presented in Chapter 5 will be installed in the SMWT. However, it is necessary to implement mechanical adaptations, and develop a new LO (since the new mixers are sub-harmonics). By the time of writing, the design of this new LO has been finished and the construction is ongoing. The installation is planned for next March, 2014. The SMWT will be used in the completion of the survey of the molecular CO.

A future improvement of the SMWT is the evaluation of the telescope optics in order to change the receiver for a heterodyne camera. Furthermore, an evaluation of the refrigeration system could be done, seeing the possibility of change the liquid Nitrogen system by a closed-loop system of Helium.

Appendix A

Appendix

During the measurements performed were identified some spurious signals coming form RFI. The spurious signals determined are presented in tables A.1, A.2 and A.3,

Table A.1: Spurious signals identified during measurements I

Source	Frequency band (MHz)
WiFi (IEEE-802.11)	2401 - 2495
Bluetooth	2400 - 2480
W-CDMA (Claro/Movistar)	UL: 824 - 849 DL: 869 -894
W-CDMA (Claro/ENTEL)	UL: 1850 - 1910 DL: 1930 -1990

Table A.2: Spurious signals identified during measurements II

UHF Source (DIGITAL TV)	Band (MHz)	Frequency band (MHz)	
		Video	Audio
Ch 24 (Canal 13)	530-536	531.25	535.75
Ch 26	542-548	543.25	547.75
Ch 27 (MEGA)	548-554	549.25	553.75
Ch 28 (LA RED)	554-560	555.25	559.75
Ch 30 (CHV)	566-572	567.25	571.75
Ch 33 (TVN)	584-590	587.25	589.75
Ch 56 (TELECANAL)	722-728	723.25	727.25

Table A.3: Spurious signals identified during measurements III

VHF Source (OPEN TV Signal)	Band (MHz)	Frequency band (MHz)	
		Video	Audio
Ch 2 (TELECANAL)	54-60	55.25	59.75
Ch 4 (LA RED)	66-72	67.25	71.75
Ch 5 (UCV)	76-82	77.25	81.75
Ch 7 (TVN)	174-180	175.25	179.75
Ch 9 (MEGA)	186-192	187.25	191.75
Ch 11 (CHV)	198-204	199.25	203.75
Ch 13 (CANAL 13)	210-216	211.25	215.75

Appendix B

Appendix

B.1 Others Designs

During this work, other designs were performed in order to support additional work at the MWL. Here we present a transition from waveguide to microstrip and a directional coupler of 20 dB in the 84−116-GHz band.

B.1.1 Adaption to Waveguide to Micro strip antenna

An adaptation from waveguide to a microstrip antenna was also design. This study was in the framework of a design of an amplifier for the LO. Two antennas were designed. One approach consisted in a typical conical antenna [63] and the second was a rectangular antenna [64]. The design goal was a −20 dB in the reflection in the band of 84 to 115 GHz. The substrate chosen was quartz 5-mil thick. The simulation and optimization of this antenna were performed in HFSS [37] and fabricated commercially by ion milling [65].

Figure B.1 presents a 3D sketch of the microstrip to waveguide transition. The S parameters for conical transition and rectangular transition are presented in figure B.2a and figure B.2b respectively. The reflections are lower than −20 dB in the band of interest accomplishing, then, the design goal in both cases.

B.1.2 Directional Coupler 20 dB

A directional coupler can be used for measuring a reference or sensing the power in a point of the system. Using a directional coupler of 20 dB of coupling is easy to estimate the input power due to 20 dB are 1% of the input power. There are several designs of commercial directional coupler [66, 67] but the typical design considers long dimensions, which in our case was a critical issue in the LO plate. The idea of a 20 dB coupler comes from the fact

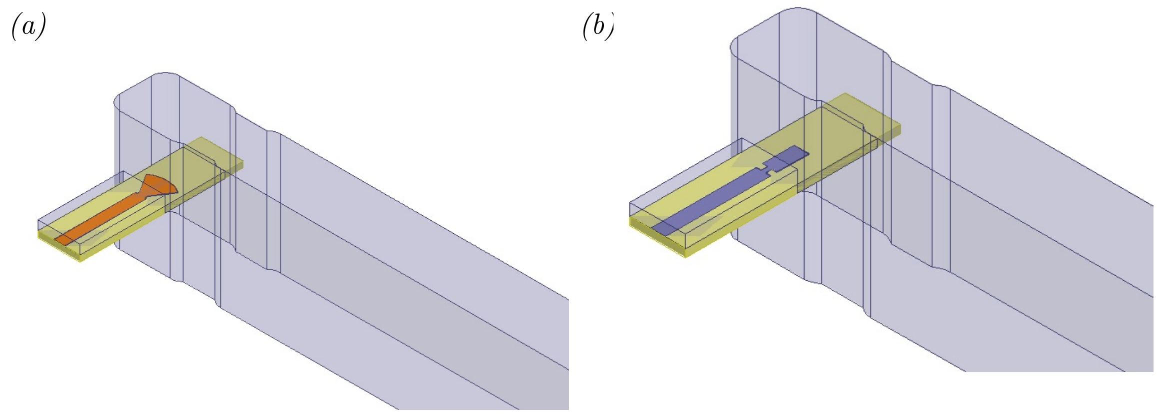

Figure B.1: *(a)* Model of a transition form waveguide to microstrip with a conical antenna. *(b)* Same model but using a rectangular antenna as transition.

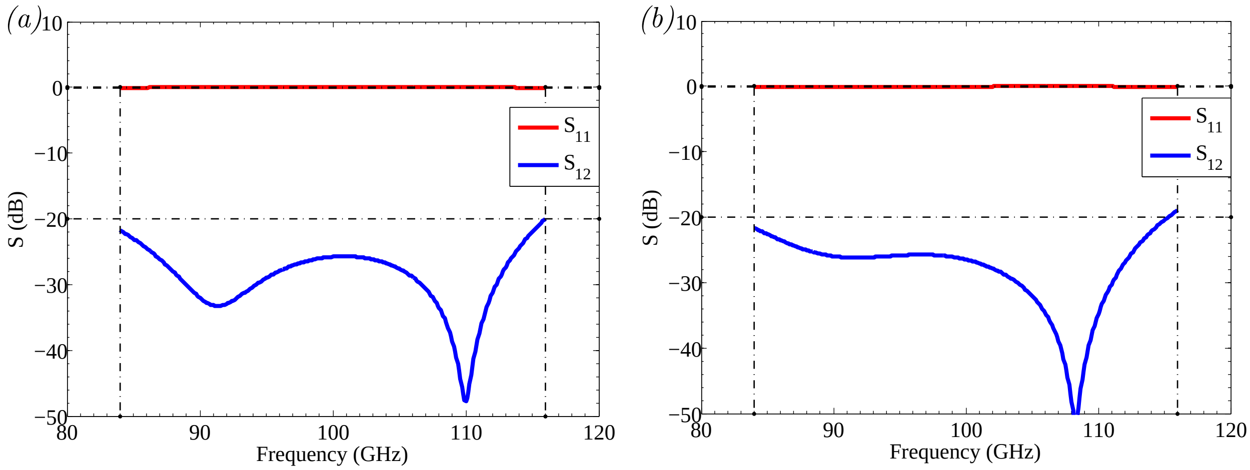

Figure B.2: *(a)* Conical. *(b)* Rectangular.

that the LO power is very limited then by sensing only 1% (20 dB) of the LO power, we reduce the leak of power due to the sensing.

In order to sense the LO power to the mixers a compact directional coupler was designed [35, 68]. These coupler will have a 20 dB of coupling and will be a four port device where one of these ports will have a load.

The design consisted in a block with inputs in WR-10 waveguide which go to the center of the block where the 4 waveguides converge in a plate which have two holes in a cross form. While the waveguides are close to the center of the block, the waveguides reduce the height through transitions. Figure B.3 presents a sketch of the directional coupler and some of the dimensions.

The results of the simulation are presented in figures B.4a and B.4b. The coupling is around 15 dB which is higher than the goal, and decrease considerably above 110 GHz. On the other hand, the reflections are higher than −20 dB, especially above 105 GHz. The isolation between ports is higher than −17 dB for all the frequency band. In general the coupler has a good behaviour below 110 GHz, but it does not meet the goal of 20 dB of coupling.

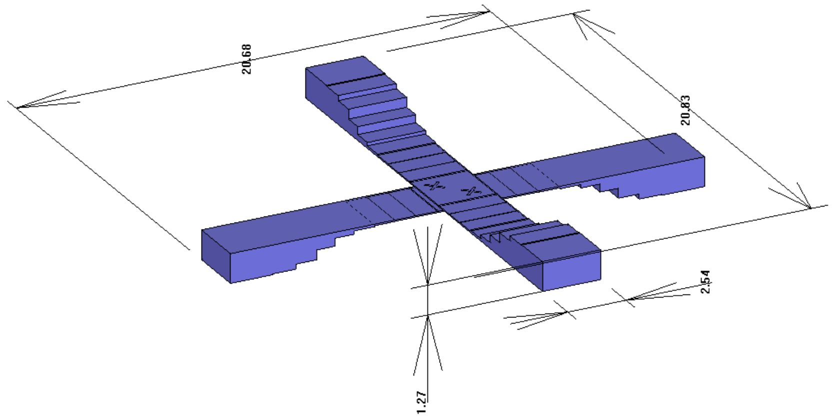

Figure B.3: Electromagnetic model of Directional Coupler 20 dB.

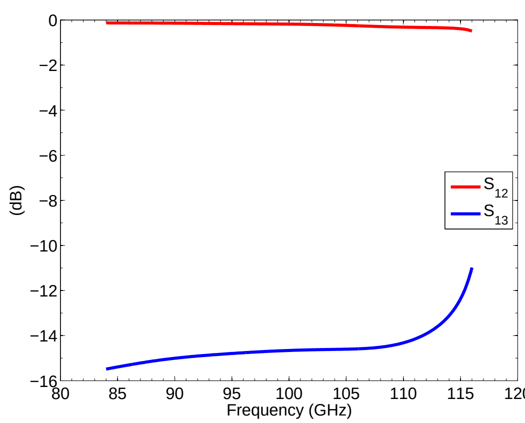

(a) Coupler Transmission.

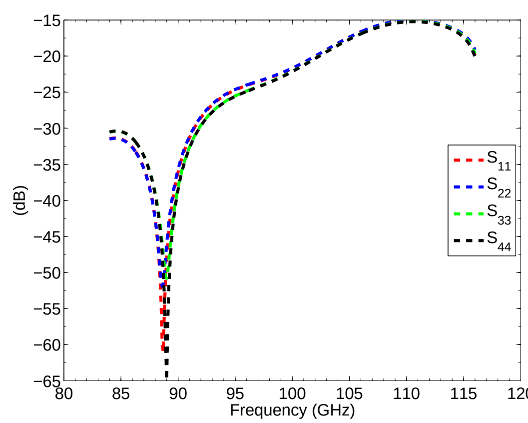

(b) Coupler Reflections.

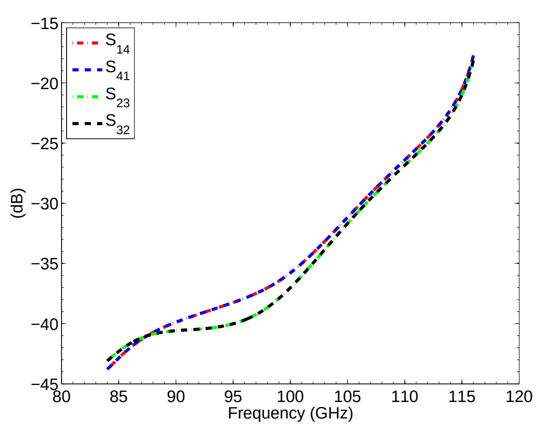

(c) Coupler Isolation.

Figure B.4: 20dB Coupler S Parameters simulation.

List of Acronyms

VLT	Very Large Telescope	1
CTIO	Cerro Tololo Inter-American Observatory	1
E-ELT	European Extremely Large Telescope	1
GMT	Giant Magellan Telescope	1
CBI	Cosmic Background Imager	1
APEX	Atacama Pathfinder EXperiment	1
ALMA	Atacama Large Millimeter Array	1
SMWT	Southern Millimeter-Wave Telescope	1
DSB	Double Sideband	1
2SB	Sideband Separating	1
SRON	Space Research Organisation Netherlands	2
CO	Carbon Monoxide	2
H_2	Molecular Hydrogen	2
LNA	Low Noise Amplifier	2
MWL	Millimeter Wave Laboratory	2
RF	Radio Frequency	2
LO	Local Oscillator	2
IF	Intermediate Frequency	3
HEMT	High Electron Mobility Transistor	5
SIS	Superconductor-Isolator-Superconductor	6
LSB	Lower Sideband	6
USB	Upper Sideband	6
SSB	Single Sideband	6
PLL	Phase Lock Loop	10
p-HEMT	Pseudomorphic High Electron Mobility Transistor	21
InP-HEMT	Indium Phosphide High Electron Mobility Transistor	21
MMIC	Microwave/Millimeter-wave Integrated Circuit	22
CASPER	Center for Astronomy Signal Processing and Electronic Research	22
ROACH	Reconfigurable Open Architecture Computing Hardware	22
FPGA	Field Programmable Gate Array	22
PowerPC	Performance Optimization With Enhanced RISC Performance Computing	23
ADC	Analog-to-Digital Converter	23
VNA	Vector Network Analyser	24
CW	continuous-wave	27
SRR	Sideband Rejection Ratio	27
CNC	Computer Numerical Control	31

HFSS	High Frequency Structure Simulation	30
SCPI	Standard Commands for Programmable Instruments	37
BW	bandwidth	41
RFI	Radio Frequency Interference	46

Bibliography

[1] ESO, “http://www.eso.org/public/,” 2011.

[2] GEMINI, “http://www.gemini.edu/,” 2011.

[3] CTIO, “http://www.ctio.noao.edu/,” 2011.

[4] G. M. Telescope, “http://www.gmto.org/overview/,” 2014.

[5] CBI, “http://www.astro.caltech.edu/ tjp/cbi/,” 2011.

[6] APEX, “http://www.apex-telescope.org/,” 2011.

[7] ALMA-NRAO, “https://science.nrao.edu/facilities/alma,” 2011.

[8] ALMA, “http://www.almaobservatory.org,” 2010.

[9] T. D. Carr, A. G. Smith, H. Bollhagen, N. F. Six, Jr., and N. E. Chatterton, “Recent Decameter-Wave Observations of Jupiter, Saturn and Venus,” *apj*, vol. 134, pp. 105–+, July 1961.

[10] T. D. Carr, F. Reyes, L. Garcia, W. B. Greenman, J. Levy, C. A. Higgins, J. M. de Buizer, J. May, J. Aparici, and H. Alvarez, “Search for effects of Comet S-L 9 fragment impacts on low radio frequency emission from Jupiter,” *Earth Moon and Planets*, vol. 66, pp. 31–48, Jan. 1994.

[11] L. Bronfman, H. Alvarez, R. S. Cohen, and P. Thaddeus, “A deep CO survey of molecular clouds in the southern Milky Way,” *apjs*, vol. 71, pp. 481–548, nov 1989.

[12] M. Bitran, H. Alvarez, L. Bronfman, J. May, and P. Thaddeus, “A large scale CO survey of the Galactic center region,” *aaps*, vol. 125, pp. 99–138, Oct. 1997.

[13] R. Mauersberger and L. Bronfman, “Molecular Gas in the Inner Milky Way,” in *Reviews in Modern Astronomy* (R. E. Schielicke, ed.), vol. 11 of *Reviews in Modern Astronomy*, p. 209, 1998.

[14] W. Max-Moerbeck, “Implementación de un Oscilador Gunn en un Receptor de 115 GHz, para fines Radio Astronómicos,” memoria para optar al titulo de ingeniero civil electricista, Universidad de Chile, 2005. Memoria para optar al titulo de ingeniero civil

electricista.

[15] N. Reyes, “Integración Física de un Amplificador de Bajo Ruido a un Receptor en 100 GHz,” memoria para optar al titulo de ingeniero civil electricista, Universidad de Chile, Aug. 2006. Memoria para optar al titulo de ingeniero civil electricista.

[16] N. Ramos, “Automatización de un Radiómetro para medir la opacidad Atmósferica a 115 GHz,” memoria para optar al titulo de ingeniero civil electricista, Aug. 2009. Memoria para optar al titulo de ingeniero civil electricista.

[17] P. Vásquez, “Instalación y Puesta en Marcha del Radiotelescopio Mini,” memoria para optar al titulo de ingeniero civil electricista, Universidad de Chile, 2011. Memoria para optar al titulo de ingeniero civil electricista.

[18] A. R. Thompson, J. M. Moran, G. W., and J. Swenson, *Interferometry and Synthesis in Radio Astronomy.* Wiley-Interscience, May 2001.

[19] F. Mena, J. Kooi, A. Baryshev, C. Lodewijk, T. Zijlstra, R. Hesper, G. Gerlofsma, T. Klapwijk, and W. Wild, “Design and Performance of a 600 - 720 GHz Sideband-Separating Receiver Using AlOx and AlN SIS Junctions,” *Microwave Theory and Techniques, IEEE Transactions on*, vol. 59, pp. 166–177, Jan. 2011.

[20] P. Astudillo, “Medición del patrón de radiación del telescopio MINI,” memoria para optar al titulo de ingeniero civil electricista, Universidad de Chile, 2014. Memoria para optar al titulo de ingeniero civil electricista.

[21] “Specifications for Four-foot Cassegrain Antennas,” tech. rep., 8 1973.

[22] J. W. Kooi, *Advanced receivers for submillimeter and far infrared astronomy.* PhD thesis, Groningen: University Library Groningen, 2008.

[23] S. A. Maas, *Microwave Mixers.* Artech House; 3rd Printing edition, June 1986.

[24] Millitech, “http://www.millitech.com/,” 2011.

[25] M. Wengler, “Submillimeter-wave detection with superconducting tunnel diodes,” *Proceedings of the IEEE*, vol. 80, pp. 1810–1826, Nov. 1992.

[26] T. L. Wilson, K. Rohlfs, and S. Hüttemeister, *Tools of Radio Astronomy.* Astronomy and Astrophysics Library, Springer; 5th ed. edition, Feb. 2009.

[27] J. Zmuidzinas, A. Karpov, D. Miller, F. Rice, H. G. Leduc, J. Pearson, and J. A. Stern, “Coherent Detection and SIS Mixers,” in *Far-IR, Sub-mm and mm Detector Technology Workshop*, 2002.

[28] H. Friis, “Noise Figures of Radio Receivers,” *Proceedings of the IRE*, vol. 32, no. 7, pp. 419–422, 1944.

[29] J. J. Whelehan, “Low-noise amplifiers-then and now,” *Microwave Theory and Tech-*

niques, IEEE Transactions on, vol. 50, pp. 806–813, Mar 2002.

[30] P. Smith, "Status of InP HEMT technology for microwave receiver applications," *Microwave Theory and Techniques, IEEE Transactions on*, vol. 44, pp. 2328–2333, Dec 1996.

[31] J. Berenz, K. Nakano, and K. Weller, "Low Noise High Electron Mobility Transistors," in *Microwave and Millimeter-Wave Monolithic Circuits*, vol. 84, pp. 83–87, May 1984.

[32] K. Duh, P. Chao, P. Ho, A. Tessmer, S. Liu, M.-Y. Kao, P. Smith, and J. Ballingall, "W-band InGaAs HEMT low noise amplifiers," in *Microwave Symposium Digest, 1990., IEEE MTT-S International*, pp. 595–598 vol.1, May 1990.

[33] R. Finger, *DESIGN AND CONSTRUCTION OF A DIGITAL SIDEBAND SEPARATING SPECTROMETER FOR THE 1.2-METER SOUTHERN RADIO TELESCOPE*. PhD thesis, Universidad de Chile, 2013.

[34] http://casper.berkeley.edu/wiki/ROACH.

[35] D. M. Pozar, *Microwave Engineering*. Wiley; 3 edition, Feb. 2004.

[36] A. R. Kerr, S.-K. Pan, and J. E. Effland, "ALMA Memo #357 - Sideband Calibration of Millimeter-Wave Receivers," tech. rep., NRAO, Mar. 2001.

[37] HFSS, "http://www.ansys.com/products/simulation+technology/electronics/signal+integrity/ansy 2010.

[38] TopSolid, "http://www.topsolid.com/," 2011.

[39] W. G. G. R. R. H. K. S. A. R. Kerr, H Moseley E. Wollack, "ALMA MEMO #494 - MF-112 AND MF-116: Compact Waveguide Loads And FTS Measurements At Room Temperature And 5 K," tech. rep., NRAO, Goddard Space Flight Center, Naval Research Lab, 2004.

[40] A. M. B. F. P. Mena, "ALMA MEMO #513 - Design and Simulation of a Waveguide Load for ALMA-band 9," tech. rep., SRON, 2005.

[41] ECCOSORB, "http://www.eccosorb.com," 2011.

[42] G. Mattheai, E. Jones, and L. Young, *Microwave Filters, Impedance-Matching Networks, and Coupling Structures*. Artech House Publishers, Feb. 1980.

[43] L. Young, "Synchronous Branch Guide Directional Couplers for Low and High Power Applications," *Microwave Theory and Techniques, IRE Transactions on*, vol. 10, no. 6, pp. 459–475, 1962.

[44] L. Young, "Stepped-Impedance Transformers and Filter Prototypes," *Microwave Theory and Techniques, IRE Transactions on*, vol. 10, no. 5, pp. 339–359, 1962.

[45] R. Levy and L. Lind, "Synthesis of Symmetrical Branch-Guide Directional Couplers,"

Microwave Theory and Techniques, IEEE Transactions on, vol. 16, no. 2, pp. 80–89, 1968.

[46] J. Reed, “The Multiple Branch Waveguide Coupler,” *Microwave Theory and Techniques, IRE Transactions on*, vol. 6, no. 4, pp. 398–403, 1958.

[47] S. Srikanth and A. R. Kerr, “ALMA Memo #343 - Waveguide Quadrature Hybrids for ALMA Receivers,” tech. rep., National Radio Astronomy Observatory, Jan. 2001.

[48] N. Marcuvitz, *Waveguide Handbook (IEEE Electromagnetic Waves Series)*. EEE Electromagnetic Waves Series, The Institution of Engineering and Technology, Apr. 1986.

[49] J. W. L. B. M. C. C. L. R. D. B. N. E. W. G. L. Y. S. C. Y. T. V. V. C. R. V. B. Wolfgang Wild, John Payne, “Chapter Five: ALMA Front Ends - ALMA Construction Project Book,” tech. rep., SRON, NRAO, Caltech, RAL, IRAM, NRO, U. Cambridge, OSO, jan 2002.

[50] H. Andoh, T. Minamidani, N. Mizuno, A. Mizuno, Y. Fukui, S. Asayama, Y. Yonekura, and H. Ogawa, “Alma memo #468 - designs of wideband 3db branch-line couplers for alma bands 3 to 10,” tech. rep., Toyota National College of Technology, Nagoya University, Osaka Prefecture University, June 2003.

[51] S. M. X. Claude, C. T. Cunningham, A. R. Kerr, and S.-K. Pan, “ALMA Memo #316 - Design of a Sideband-Separating Balanced SIS Mixer Based on Waveguide Hybrids,” tech. rep., Herzberg Institute of Astrophysics National Research Council of Canada , National Radio Astronomy Observatory, Sept. 2000.

[52] E. Wollack, “On the Compensation of E-Plane Bifurcation in Rectangular Waveguide,” tech. rep., NRAO, Charlottesville, VA, Oct. 1997.

[53] A. R. Kerr, “ALMA Memo #381 - Elements for E-Plane Split-Block Waveguide Circuits,” tech. rep., NRAO, July 2001.

[54] MITEQ, “http://www.miteq.com/,” 2011.

[55] R. Finger, P. Mena, N. Reyes, R. Rodriguez, and L. Bronfman, “A Calibrated Digital Sideband Separating Spectrometer for Radio Astronomy Applications,” in *Publications of the Astronomical Society of the Pacific* [55], pp. pp. 263–269.

[56] F. P. Mena, A. Baryshev, J. Kooi, C. F. J. Lodewijk, G. Gerlofsma, R. Hesper, and W. Wild, “Side-band-separating heterodyne mixer for band 9 of ALMA.,” in *Infrared Millimeter Waves and 14th International Conference on Teraherz Electronics, 2006. IRMMW-THz 2006. Joint 31st International Conference on*, pp. 522–522, 2006.

[57] A. M. B. J. A. K. W. M. K. T. Z. G. G. M. B. K. K. H. S. J. B. F. P. M. A. K. R. R. T. M. K. W. W. R. Hesper, B. D. Jackson, “Design and development of a 600-720 GHz receiver cartridge for ALMA Band 9,” in *16th International Symposium on Space Terahertz Technology*, pp. 110–115, 2005.

[58] e. a. Andrey Khudchenko ; Ronald Hesper ; Andrey Baryshev ; Gerrit Gerlofma ; Jan Barkhof, "Sideband separating mixer for 600-720 GHz for ALMA band 9 upgrade," in *Proc. SPIE 8452, Millimeter, Submillimeter, and Far-Infrared Detectors and Instrumentation for Astronomy VI*, 2012.

[59] A. Khudchenko, R. Hesper, A. Baryshev, F. P. Mena, J. Barkhof, T. Klapwijk, and M. Spaans, "Sideband separating mixer for 600 720 GHz based on SIS," in *Infrared, Millimeter, and Terahertz Waves (IRMMW-THz), 2012 37th International Conference on*, pp. 1–1, 2012.

[60] A. Baryshev, R. Hesper, K. Wielinga, G. Gerlofsma, and M. Carter, "Design and Verification of ALMA Band 9 Receiver Optics," in *Fifteenth International Symposium on Space Terahertz Technology* (G. Narayanan, ed.), p. 433, 2004.

[61] P. Dindo, S. Claude, D. Derdall, D. Henke, D. Erickson, G. Rodrigues, A. Lichtenberger, and S.-K. Pan, "Design and characterization of sideband-separating SIS mixer RF hybrids for the Band 3 receiver (84-116 GHz)," in *Infrared and Millimeter Waves and 13th International Conference on Terahertz Electronics, 2005. IRMMW-THz 2005. The Joint 30th International Conference on*, vol. 2, pp. 409–410 vol. 2, 2005.

[62] S. Claude, P. Dindo, D. Erickson, F. Jiang, K. Yeung, D. Derdall, D. Duncan, D. Garcia, D. Henke, B. Leckie, A. Lichtenberger, P. Niranjanan, S.-K. Pan, M. Pfleger, G. Rodrigues, K. Szeto, P. Welle, and K. Caputa, "The Band 3 receiver (84-116 GHz) for ALMA," in *Infrared and Millimeter Waves and 13th International Conference on Terahertz Electronics, 2005. IRMMW-THz 2005. The Joint 30th International Conference on*, vol. 2, pp. 407–408 vol. 2, 2005.

[63] J. Kooi, A. Kovacs, M. Sumner, G. Chattopadhyay, R. Ceria, D. Miller, B. Bumble, H. LeDuc, J. Stern, and T. Phillips, "A 275-425 GHz Tunerless Waveguide Receiver Based on AlN-Barrier SIS Technology," *Microwave Theory and Techniques, IEEE Transactions on*, vol. 55, pp. 2086–2096, Oct 2007.

[64] Y.-C. Leong and S. Weinreb, "Full band waveguide-to-microstrip probe transitions," in *Microwave Symposium Digest, 1999 IEEE MTT-S International*, vol. 4, pp. 1435–1438 vol.4, June 1999.

[65] I. B. Milling, "http://www.ionbeammilling.com/," 2014.

[66] Aerowave, "www.aerowave.net," 2014.

[67] Quinstar, "http://quinstar.com/," 2014.

[68] J. A. R. Ball and T. M. Sulda, "Small aperture crossed waveguide broad-wall directional couplers," *Microwaves, Antennas and Propagation, IEE Proceedings*, vol. 147, pp. 249–254, Aug 2000.